Università degli Studi di Trieste

XXXIV CICLO DEL DOTTORATO DI RICERCA IN NANOTECNOLOGIE

"TIME-RESOLVED STUDY OF THE EXCITON DYNAMICS AND CHARGE SEPARATION IN SEMICONDUCTORS"

SETTORE SCIENTIFICO DISCIPLINARE: FIS/03

DOTTORANDO
CRISTIAN SONCINI

COORDINATORE
PROF. ALBERTO MORGANTE

SUPERVISORE DI TESI
DR. MADDALENA PEDIO

Anno Accademico 2021/2022

Abstract

The current challenge in nanoscience consists of understanding and engineering the functionality of nanostructured materials at the nanoscale, optimizing the control of the properties of the materials in increasingly smaller time and energy scales. Organic semiconductors constitute a class of nanomaterials that integrate and expand the performance of inorganic materials. Aggregation and inter-molecular interactions have a significant impact on tuning the photo-physical and dynamical carrier properties of the film, affecting the light absorption, the energy level alignment, the exciton diffusion and the charge transport in the material. In this regard, time-resolved spectroscopies provide access to information about charge transfer, charge separation and de-excitation phenomena, demonstrating the intimate connection between structure and electronic properties. Exciton dynamics, charge transfer and charge separation are fundamental processes in organic-based devices. For this reason, a deeper understanding of these processes is necessary.

The influence of the molecular ordering in cobalt phthalocyanine (CoPc) thin films is investigated by a multi-technique approach (time-resolved photoemission and optical spectroscopies), demonstrating the connection between the charge transfer (CT) process and molecular structure. Competitive de-excitation through internal conversion (IC) and intersystem crossing (ISC) processes is observed. However, relaxation from triplet excited states (populated by ISC) is the preferential relaxation pathway, resulting in long-living CoPc excited states (a highly desirable characteristic in many device applications). Enhanced CT exciton lifetime is observed in CoPc film with herringbone structure (decay time of tens of ps) with respect to the brickstone structure (decay time of a few ps).

The surface photovoltage (SPV) process arises whenever photo-generated charge carriers are separated in space, modifying the electronic structure at the interface over time. In a device based on heterojunction, the efficiency of charge separation and the interface energy level alignment are crucial aspects in determining its performance. The SPV effect in the copper phthalocyanine (CuPc)/SiO_2/p-Si(100) heterojunction is investigated using time-resolved photoemission spectroscopy. The CuPc thin film shows a transient SPV effect with identical magnitude and relaxation dynamics of the SiO_2/Si(100) substrate, highlighting a direct connection between the SPV relaxation dynamics in the two materials. The new Light/Electron Induced Non-Equilibrium phenomena Calculator (LEINEC) code has been developed to get a more clear understanding of the SPV dynamics in semiconductors. It successfully modelled the transient SPV effect in the studied systems.

Among X-ray-based techniques, X-ray absorption offers the advantage to probe both the electronic and morphologic structure of the system. With the aim of better understanding the structural evolution in the dynamics of electronic properties, we developed a new experimental end-station for time-resolved X-ray absorption spectroscopy, in which excited state dynamics can be characterised with 80-100 ps resolution. A discussion of preliminary experimental results of the chamber commissioning is reported.

The results presented in this thesis demonstrate the valuable contribution of time-resolved spectroscopies in providing detailed information on carrier and interface dynamics in organic and inorganic semiconductors.

Contents

Introduction

The current challenge in nanoscience consists of understanding and engineering the functionality of nanostructured materials at the nanoscale, optimizing the control of the properties of the materials in time and energy scales increasingly smaller. Organic semiconductors constitute a class of nanomaterials that complement and expand the performance of inorganic materials. Their use is increasingly widespread for several technological applications such as microelectronic, spintronic, photovoltaic and photoelectronic devices[1-5].

The study of excited state dynamics by using time-resolved spectroscopies is strongly benefiting of new light sources (lasers with ultra-short pulse duration) and large-scale facilities (free electron lasers and synchrotrons)[6-13]. The use of energy-tunable and high-intensity light sources is providing access to new information not previously observable about charge transfer and de-excitation phenomena, demonstrating the intimate connection between structure and electronic properties. Many studies have been carried out on molecules in solution[14-20]. However, only recently the field of investigation has been extended to molecular solids and thin films, revealing substantial differences to the liquid phase. Molecular aggregation in the solid state as well as the formation of molecular crystals induce unique properties, which differ from those of the single molecule or their liquid phase, influencing the optical and electromagnetic properties[21-26]. In molecular solids, the excitation to high energy excited states leads to relaxation dynamics through meta-stable states, in which the excess energy is partly dissipated through phonons and intra-molecular vibrations. This situation leads to exciton and charge dynamics dependent on the molecular arrangement. Electron-phonon coupling and similar phenomena can strongly influence the charge and exciton transport in the molecular film, affecting the efficiency of the device itself[21,25,26]. Moreover, charge separation effects, i.e. the ability of a system (inorganic and organic semiconductor interfaces) to separate charges upon light absorption, are crucial characteristics of an efficient device[27]. The detailed understanding and control of the processes determining the dynamical properties of organic semiconductors are crucial factors for further developing and engineering organic-based technological applications. However, still significant work is necessary to understand and control exciton transport and dissociation mechanisms in molecular solids to fully benefit from the advantages offered by organic semiconductors and rationally design functional optoelectronic devices.

Aim of the thesis

The main objective of this thesis work was to get a deeper insight into the carrier and interface dynamics in organic thin films and organic-inorganic semiconductor heterojunctions. A study of the influence of molecular aggregation and ordering on the

excited state dynamics in organic thin films as well as the characterization of the surface photovoltage effect in organic heterojunctions is here reported. One major task of this thesis work was the development and commissioning of an experimental setup for time-resolved X-ray absorption spectroscopy (TR-XAS endstation). In recent years, increasing attention has been given to the investigation and deeper understanding of dynamic properties in organic films, as a real benefit to their commercial use in various technological applications. Pump-probe spectroscopies are a class of techniques widely used to study electronic dynamics in materials science, though the majority of laboratories solely rely on lasers. By using X-ray photons as a probe, the core levels are accessible providing additional elemental information which complements the excited states dynamics picture provided by optical transient techniques. As will be shown in the following chapters a multi-technique approach, combining laser and X-ray-based time-resolved techniques, provides a clearer and detailed understanding of the relaxation dynamics in materials, in many cases not achievable by solely using a single experimental approach.

Chapter 3 reports the study of the influence of molecular ordering on the cobalt phthalocyanine (CoPc) thin film excited state dynamics. The impact of different structures (herringbone and brickstone) on the energy level alignment and dynamical electronic properties of CoPc thin films was characterized using a multi-technique approach. Transient absorption spectroscopy (TAS) measurements show enhanced CT exciton lifetime in CoPc film with herringbone structure (decay time of tens of ps) with respect to the brickstone structure (decay time of a few ps). The de-excitation pathways of the excited states were addressed, demonstrating the competition between internal conversion and intersystem crossing (ISC) processes. However, complete de-excitation is observed in the ns time scale states through triplet excited states populated by ISC. The complementary use of TAS and time-resolved photoemission (TR-PES) measurements point out a new fast dynamic of hundreds of fs directly involving the Co $3d_z^2$ atomic orbital. This relaxation process is tentatively explained by assuming partial charge density redistribution between the macrocycle and the Co atom.

Chapter 4 reports the characterization of the surface photovoltage (SPV) effect in inorganic semiconductors and organic-inorganic heterojunctions. During my PhD, I developed the LEINEC (Light/Electron Induced Non-Equilibrium phenomena Calculator) code to model the surface voltage[28] (SV) and SPV effects in semiconductor systems[29-31]. The first step consisted in testing the validity of the code in predicting the static and transient SPV in a set of inverse photoemission and photoemission experimental data[32,33,34] (SiO_2/Si, GaP and GaAs systems). In the second step, TR-PES measurements were performed on n- and p-Si/SiO_2 systems to characterize the dependence of the SPV relaxation dynamics on the doping and photon flux. The LEINEC code has been able to correctly evaluate their SPV magnitude and relaxation dynamics. Finally, the copper phthalocyanine heterojunction (CuPc/SiO_2/p-Si) was studied by TR-PES. Transient SPV effect is observed in the molecular thin film with identical magnitude and relaxation dynamics of the SiO_2/p-Si substrate, suggesting a relationship between the SPV relaxation dynamics between organic and inorganic materials.

Finally, Chapter 5 describes the new TR-XAS endstation now in commissioning at the BACH beamline (Elettra synchrotron), in which is possible to perform time-resolved X-ray absorption (TR-XAS) experiments up to 80-100 ps resolution through the multi-bunch operation mode of the Elettra synchrotron. The new presented TR-XAS setup is developed according to the configuration used at the BACH beamline at Elettra. The experimental chamber allows a variable mutual geometry between the pump, probe and detector. The feasibility of TR-XAS experiments is strongly determined by an optimal overlap between pump and probe beams. Differently to TAS, in X-ray-based time-resolved experiments, the penetration depths between X-ray and laser may strongly differ, depending on the nature of the sample. For this reason, variable X-ray-laser geometry is mandatory to optimize the excitation volume, maximizing the signal-to-noise ratio (S/N). The effect of different geometrical configurations of the incident beams and detection angle in XAS experiments will be demonstrated by systematic studies on model samples. A new T-XRES (Time-resolved X-ray Experiment Simulator) code was developed as an auxiliary tool to the TR-XAS chamber to a priori optimize the experimental condition. The code can evaluate the laser-X-ray excitation volume, the detector efficiency (for a given absorption edge), the signal counts in static mode as well as the S/N in time-resolved operation mode as a function of the chosen experimental geometry.

References:

[1] P. Friederich, A. Fediai, S. Kaiser, M. Konrad, N. Jung, and W. Wenzel. Toward Design of Novel Materials for Organic Electronics. *Adv. Mater.* **2019**, 31, 1808256.

[2] C. Wang, X. Ren, C. Xu, B. Fu, R. Wang, X. Zhang, R. Li, H. Li, H. Dong, Y. Zhen, S. Lei, L. Jiang, and W. Hu. N-Type 2D Organic Single Crystals for High-Performance Organic Field-Effect Transistors and Near-Infrared Phototransistors**.** *Adv. Mater.* **2018**, 30, 1706260.

[3] T. Tsujimura. *OLED Display Fundamentals and Applications*. John Wiley & Sons, Hoboken, NJ, USA **2017**.

[4] T M. Clarke and James R. Durrant. Charge Photogeneration in Organic Solar Cells. *Chem. Rev.* **2010,** *110*, 6736–6767.

[5] [D. Li and G. Yu. Innovation of Materials, Devices, and Functionalized Interfaces in Organic Spintronics. *Adv. Funct. Mater.* **2021**, 31, 2100550.

[6] A. Pietzsch, A. Föhlisch, M. Beye, M. Deppe, F. Hennies, M. Nagasono, E. Suljoti, W. Wurth, C. Gahl, K. Döbrich, and A. Melnikov. Towards time resolved core level photoelectron spectroscopy with femtosecond x-ray free-electron lasers. *New Journal of Physics* **2008**, 10, 033004.

[7] H.T. Lemke et al. Femtosecond x-ray absorption spectroscopy at a hard x-ray free electron laser: Application to spin crossover dynamics. *Journal of Physical Chemistry A* **2013**, 117, 735-740.

[8] S. Hellmann, C. Sohrt, M. Beye, T. Rohwer, F. Sorgenfrei, M. Marczynski-Bühlow, M. Kalläne, H. Redlin, F. Hennies, M. Bauer, A. Föhlisch, L. Kipp, W. Wurth, and K. Rossnagel. Time-resolved x-ray photoelectron spectroscopy at FLASH. *New Journal of Physics* **2012**, 14, 013062.

[9] L. Stebel, M. Malvestuto, V. Capogrosso, P. Sigalotti, B. Ressel, F. Bondino, E. Magnano, G. Cautero, and F. Parmigiani. Time-resolved soft x-ray absorption setup using multibunch operation modes at synchrotrons. *Review of Scientific Instruments* **2011**, *82*, 123109-44913.

[10] A. M. March, A. Stickrath, G. Doumy, E. P. Kanter, B. Krässig, S. H. Southworth, K. Attenkofer, C. A. Kurtz, L. X. Chen, and L. Young. Development of high-repetition-rate laser pump/x-ray probe methodologies for synchrotron facilities. *Review of Scientific Instruments* **2011**, 82, 073110.

[11] A. Shavorskiy et al. Sub-nanosecond time-resolved ambient-pressure X-ray photoelectron spectroscopy setup for pulsed and constant wave X-ray light sources. *Review of Scientific Instruments* **2014**, 85.

[12] G. Vankó, P. Glatzel, V.-T. Pham, R. Abela, D. Grolimund, C. N. Borca, S. L. Johnson, C. J. Milne, and C. Bressler. Picosecond Time-Resolved X-Ray Emission Spectroscopy: Ultrafast Spin-State Determination in an Iron Complex. *Angewandte Chemie International Edition* **2010**, 49, 5910-5912.

[13] K. Zhang, M. F. Lin, E. S. Ryland, M. A. Verkamp, K. Benke, F. M. De Groot, G. S. Girolami, and J. Vura-Weis. Shrinking the Synchrotron: Tabletop Extreme Ultraviolet Absorption of Transition-Metal Complexes. *Journal of Physical Chemistry Letters* **2016**, 7, 3383-3387.

[14] S. V. Rao, and D. N. Rao. Excited state dynamics in phthalocyanines studied using degenerate four wave mixing with incoherent light. *J. Porphyrins Phthalocyanines* **2002**, 6, 233-237.

[15] J. McVie, R. S. Sinclair, and T. G. Truscott. Triplet states of copper and metal-free phthalocyanines**.** Faraday Trans.**1978**, 2, 74, 1870–1879.

[16] A. V. Nikolaitchik, O. Korth and M. A. J. Rodgers. Direct determination of nonradiative relaxation rates in nonfluorescent metallophthalocyanines**.** *J. Phys. Chem. A*, **1999**, 103, 7587–7596.

[17] O. Bram, thesis: Ultrafast Visible and Ultraviolet Fluorescence Studies of Molecular and Biological Sytems in Solution. Ecole polytechnique federale de Lausanne, **2011**.

[18] M. J. Van Vleet, T. Weng, X. Li, and J.R. Schmidt. In Situ, Time-Resolved, and Mechanistic Studies of Metal–Organic Framework Nucleation and Growth**.** *Chemical Reviews* **2018,** 118, 7, 3681-3721.

[19] M. Chergui. Picosecond and femtosecond X-ray absorption spectroscopy of molecular systems. *Acta Crystallogr. A* **2010**, 66**,** 229–239.

[20] W. Gawelda, M. Johnson, F.M.F. de Groot, R. Abela, C. Bressler and M. Chergui. Electronic and molecular structure of photoexcited $[Ru^{II}(bpy)_3]^{2+}$ probed by picosecond X-ray absorption spectroscopy. *J. Am. Chem. Soc*. **2006**, 128, 15, 5001–5009.

[21] C. Qian, J. Sun, and Y. Gao. Transport of charge carriers and optoelectronic applications of highly ordered metal phthalocyanine heterojunction thin films**.** *Phys. Chem. Chem. Phys.* **2021**, 23, 9631.

[22] H. Lim, S. Yang, S.-H. Lee, J.-Y. Lee, Y. Lee, A. B. Situmorang, Y.-H. Kim, and J. W. Kim. Influence of the metal phthalocyanine molecular orientation on charge separation at the organic donor/acceptor interface. *J. Mater. Chem. C*, **2021**, 9, 2156.

[23] C. Videlot, A. El Kassmi, and D. Fichou, Photovoltaic properties of octithiophene-based Schottky and p/n junction Cells: Influence of molecular orientation *Sol. Energy Mater. Sol. Cells*, **2000**, 63, 69-82.

[24] V. Coropceanu, J. Cornil, D. A. da Silva Filho, Y. Olivier, R. Silbey, and J.-L. Bredas. Charge transport in organic semiconductors**.** *Chem. Rev*., **2007**, 107, 926-952.

[25] S. Duhm, G. Heimel, I. Salzmann, H. Glowatzki, R. L. Johnson, A. Vollmer, J. P. Rabe, and N. Koch. Orientation-dependent ionization energies and interface dipoles in ordered molecular assemblies. *Nat. Mater.* **2008**, **7**, 326.

[26] T. Wang, T. R. Kafle, B. Kattel, and W.-L. Chan. Observation of an Ultrafast Exciton Hopping Channel in Organic Semiconducting Crystals. *J. Phys. Chem. C* **2016**, 120, 14, 7491–7499.

[27] T. Dittrich, and S. Fengler. *Surface Photovoltage Analysis of Photoactive Material*. World Scientific, **2020**.

[28] M. Cantoni, R. Bertacco, A. Brambilla, F. Ciccacci Photon- and electron-induced surface voltage in electron spectroscopies on ZnSe(0 01). *Journal of Electron Spectroscopy and Related Phenomena* **2009** 173, 84–87

[29] M. A. Reshchikov, M. Foussekis, and A. A. Baski. Surface photovoltage in undoped n -type GaN. *Journal of Applied Physics* **2010**, 107, 113535.

[30] M. Foussekis, J. D. McNamara, A. A. Baski, and M. A. Reshchikov. Temperature-dependent Kelvin probe measurements of band bending in p-type GaN. *Applied Physics Letters* **2012**, 101, 082104.

[31] M. H. Hecht. Time dependence of photovoltaic shifts in photoelectron spectroscopy of semiconductors. *Phys. Rev. B* **1991**, 43, 12102–12105.

[32] M. Alonso, R. Cimino, and K. Horn. Surface Photovoltage Effects in Photoemission from Metal-GaP(110) Interfaces: Importance for Band-Bending Evaluation. *PRL* **1990**, 64, 16.

[33] W. Widdra, D. Bröcker, T. Gießel, I. V. Hertel, W. Krüger, A. Liero, F. Noack, V. Petrov, D. Pop, P. M. Schmidt, R. Weber, I. Will, and B. Winter. Time-resolved core level photoemission: surface photovoltage dynamics of the SiO2/Si(100) interface. *Surface Science* **2003**, 543, 87–94.

1. Dynamics in solids

In the view of technological applications, the interplay between the generation of free carriers, charge transport, charge separation and recombination processes plays a key role in optoelectronic and photonic devices. This chapter will provide a short overview of the dynamical processes in organic and inorganic semiconductors covered in this thesis.

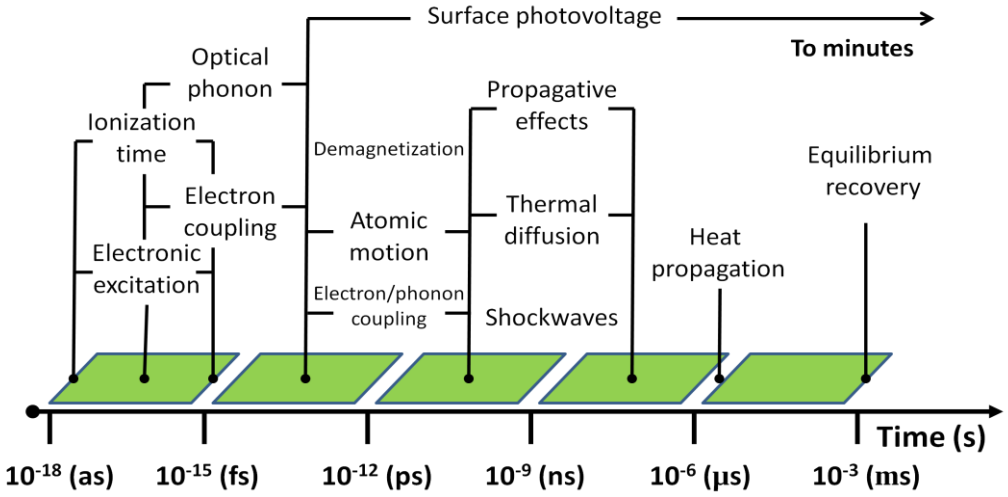

Figure 1.1 *Schematic illustration of the possible dynamical processes after excitation in solid materials.*

As shown in Figure 1.1, charge dynamics involve multiple timescales, and different relaxation pathways of the excited states depending on the chemical and physical properties of the system (type of semiconductor, structural properties, dopant concentration, defects etc…). Several factors have to be considered in designing semiconductor-based devices. Anyway, high charge mobility and low recombination of the carriers are essential requirements. In solids, an effective way to enhance the charge transport efficiency is the optimization of the crystalline structure, a complex task especially in organic semiconductors[1-6]. Due to the localized nature of the states over the molecular site, different molecular ordering can lead to more favourable intermolecular interactions between neighbour molecules, potentially increasing the charge separation and transport efficiency[1-3,5,7-9].

The majority of the presently available commercial devices are based on semiconductor homo/heterojunctions. The semiconductor interface properties can drastically differ from those of the bulk. Moreover, they are strongly dependent on the type of semiconductors in contact. The energy level alignment at the interface plays a crucial role in determining the behaviour and charge transport efficiency in devices. Close to the junction interface, the energy bands of the materials are bent[10,11]. In the case of incident light, this condition gives rise to a peculiar non-equilibrium phenomenon known as surface photovoltage (SPV), which modifies the energy band positions at the interface over time. As a consequence, the

charge transport and injection properties at the interface can be affected as well. To address all these issues, a detailed understanding of the interconnection between the dynamics of excited states and the material properties is a key factor in designing and optimising the device performance, implying the possibility to ad-hoc engineer the electronic properties and the carrier transport in solid films.

1.1 Non-equilibrium: excitation and de-excitations effects

Light excitation with photons of suitable energy promotes materials from their ground state to an electronically excited state, causing changes in their electronic structure. As a consequence, materials in the excited state configuration can be considered as different species with different chemical-physical properties. Since the excited configuration is a non-equilibrium condition, the system will tend to dissipate the excess energy relaxing to the ground state. This fact implies that the excited state is characterised by a lifetime and several different de-excitation pathways are possible. The relaxation mechanisms of the excited state involve radiative and non-radiative processes[12]. Depending on several factors related to the nature of the system (organic or inorganic), one de-excitation pathway can be more favourable than another. In inorganic semiconductors, the excitation process generates free carriers in the material. This is due to the comparable exciton binding energy to the thermal broadening ($\Delta \cong 25$ meV $\cong K_B T$ at room temperature)[13]. On the contrary, in organic materials, the exciton binding energy ranges from hundreds of meV to 1.5 eV[14], and the excitation process generates excitons (bound state of an electron-hole pair by the electrostatic Coulomb force), leading to a completely different evolution in the time of the excited states to the case of the inorganic semiconductors. Furthermore, inorganic and molecular solids are two opposite extreme cases of materials that exhibit substantially different transport mechanisms. In inorganics, the wavefunctions of the states are delocalized over the entire volume giving rise to bands (valence and conduction band), and the transport mechanism is called band transport. On the contrary, in organic semiconductors, the transport is inter-molecular (transition between localized molecular sites), or hopping transport. As a consequence, the charge mobility and diffusion length of the carriers show strong differences in the two cases[12-15].

Systems with long-living excited states and low recombination yield of excitons/free carriers are highly desirable to achieve high-efficiency devices. Accordingly, to move toward organic-based technology, several additional factors have to be considered in optimising the molecular film properties for device applications. One critical issue to overcome these problems nowadays is the need for thorough control of the molecular structure during film processing, even though fabrication of low-cost organic semiconductor crystals and films is still challenging. Depending on the growth method different molecular structures are obtained, resulting in different excited state dynamics[16 and refs therein]. Aggregation and inter-molecular interactions have a significant impact on tuning the photo-physical properties of the film[1,2,6,17], affecting the light absorption, energy

level alignment, exciton diffusion and charge transport[3-5]. Therefore, a detailed understanding of the relationship between structural and dynamical properties is mandatory to optimise the intermolecular interactions and promote efficient charge transport in organic semiconductors. Materials showing a high intersystem crossing (ISC) quantum yield are extremely attractive, since they generate long-living triplet states (that would not possible to be obtained by direct excitation from the ground state - spin selection rule) from short-living singlet states, potentially increasing the performance of several optoelectronic and photonic devices[18]. Previous studies in the literature have shown how charge transfer (CT) states can play an essential role as intermediates in enabling a rapid evolution between the singlet and triplet configurations[7,19].

Pump-probe (PP) spectroscopy is a class of techniques that offers the possibility to address all those issues, providing a detailed characterisation of the excited state properties. Depending on the chosen PP technique, it is possible to clarify the electronic and structural properties of transient states, as well as their relationship in a wide range of temporal domains[20,21].

1.1.1 Pump-probe spectroscopy

As suggested by the name, in a PP experiment two light beams are used, a pump pulse and a probe pulse interacting with the sample over a specific time domain. The pump pulse optically excites the material, creating excited species with transient character. The probe pulse monitors the evolution in time of the excited states at fixed time delays. Figure 1.2 shows a sketch of the dynamical processes that occur in PP experiments after the excitation of the sample. Depending on the type of dynamical processes of interest, different transient techniques can be used. Transient absorption spectroscopy (TAS) is an extension of optical absorption spectroscopy, which provides information on the optical properties of the excited states. The technique is based on measuring changes in the absorbance or transmittance in the sample after the excitation (from the ground state) as a function of the time after excitation. This technique is highly effective in providing information on the electronic dynamical properties of the excited states. However, it lacks structural resolution and is not element sensitive. Time-resolved X-ray absorption spectroscopy (TR-XAS) is more versatile due to the possibility to probe both the electronic and local structure (within a few nm) with element sensitivity. Excitation of core orbitals allows probing the unoccupied density of states. For photoelectrons excited above the Fermi level, in solids, multiple scattering events occur (with neighbor atoms), giving rise to modulations in the spectrum which provides information on the surrounding environment of the absorber. Therefore, TR-XAS can provide information on structural variations during the de-excitations [22].

The complementary use of information gained through different time-resolved techniques is nowadays becoming a powerful tool to provide a complete characterization of the excited states. Examples are phthalocyanine (Pc) and porphyrin (P) systems, where in recent years their ultrafast dynamical properties have been extensively studied[6,7,23-27].

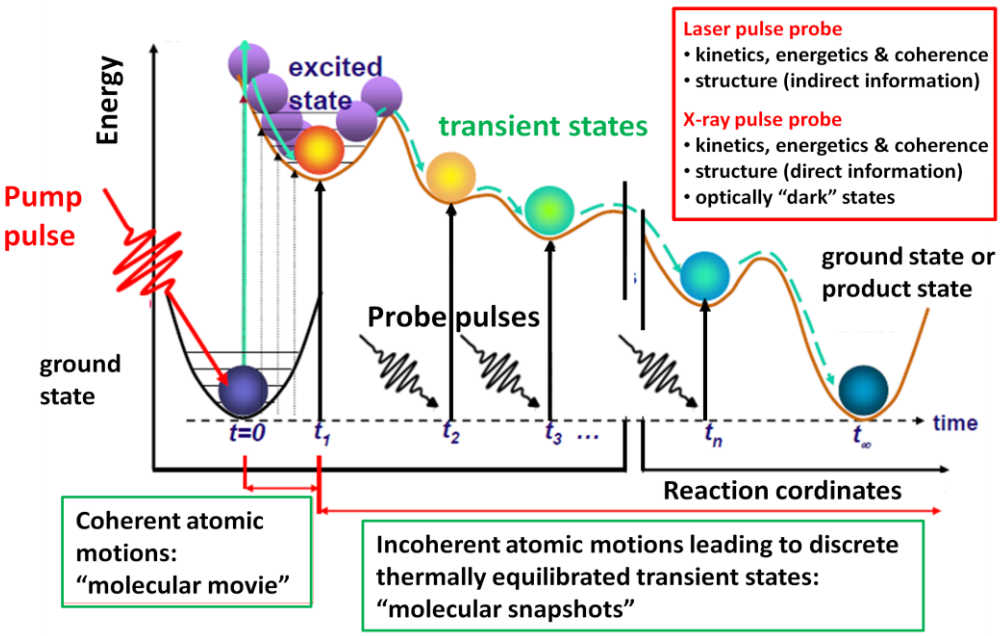

Figure 1.2 *Representation of the evolution in time of the excited states after excitation of the system as measured in PP experiments [courtesy of Prof. F. Parmigiani].*

TAS studies pointed out how the coordination and type of transition metal atom into the Pc macrocycle lead to ultrafast relaxation of the singlet states[7,23]. The presence of a transition metal in the macrocycle origins additional excited states, πd* or CT states which, coupling to intra-molecular exciton states, provides new de-excitation pathways. The origin of CT states and their role as intermediates in promoting a rapid evolution between singlet and triplet configuration, in solution and solid state, have been clarified as well[18,28]. For example, TR-XAS has been used to simultaneously track the electronic structure and atomic coordinates of Ni-porphyrins along their de-excitation pathways[21]. The comparison between the relaxation dynamics in solution (using different solvents) and in the solid states (film or embedded in a matrix) helped to rationalize the relationship between structure and electron dynamics in metal complexes[6,7,20,23,25-27,29].

1.2 The surface photovoltage effect

Charge separation effects, i.e. the ability of a system (inorganic and organic semiconductor interfaces) to separate charges upon light absorption, are crucial characteristics of an efficient device. A deeper understanding of charge separation and transport processes is important for applications in optoelectronics, such as organic light-emitting diodes and organic solar cells[1,3,10,11,30]. SPV effect arises whenever photo-generated charge carriers are separated in space. The SPV signal depends on fundamental processes arising after light absorption such as photo-generation of mobile charge carriers,

charge transport, recombination and relaxation processes. Related phenomena can be generally investigated by SPV techniques in photoactive materials[10,11,29].

Semiconductors with remarkable bulk electronic properties are a necessary starting point. However, the majority of the presently available commercial devices are based on hetero/homojunctions, and in many cases, the function originates at the interface. Therefore, a detailed understanding of the interfacial electronic structure is an essential requirement to properly engineer semiconductor-based devices. When two semiconductors (or a metal and a semiconductor) are in contact the energy level alignment at the interface is modified and the bands of both materials are bent[10,11,13] (Figure 1.3a). The crucial factors of the interfacial electronic structure can be simplified in two main aspects: The energy level alignment at the interface determines the carrier injection, and the band bending is essential for the carrier separation. However, on the semiconductor surface, surface states may exist due to the termination of lattice periodicity. Typically the density of surface states is larger ($\sim 10^{15}$ cm^{-2}) than the one due to bulk dopant states ($\sim 10^{8}$–10^{12} cm^{-2}), and the surface E_F can be pinned at the mid-gap[10,13]. Therefore, in n-type and p-type semiconductors, similarly to the contact case, band bending at the semiconductor surface may exist (Figure 1.3b)[10,13].

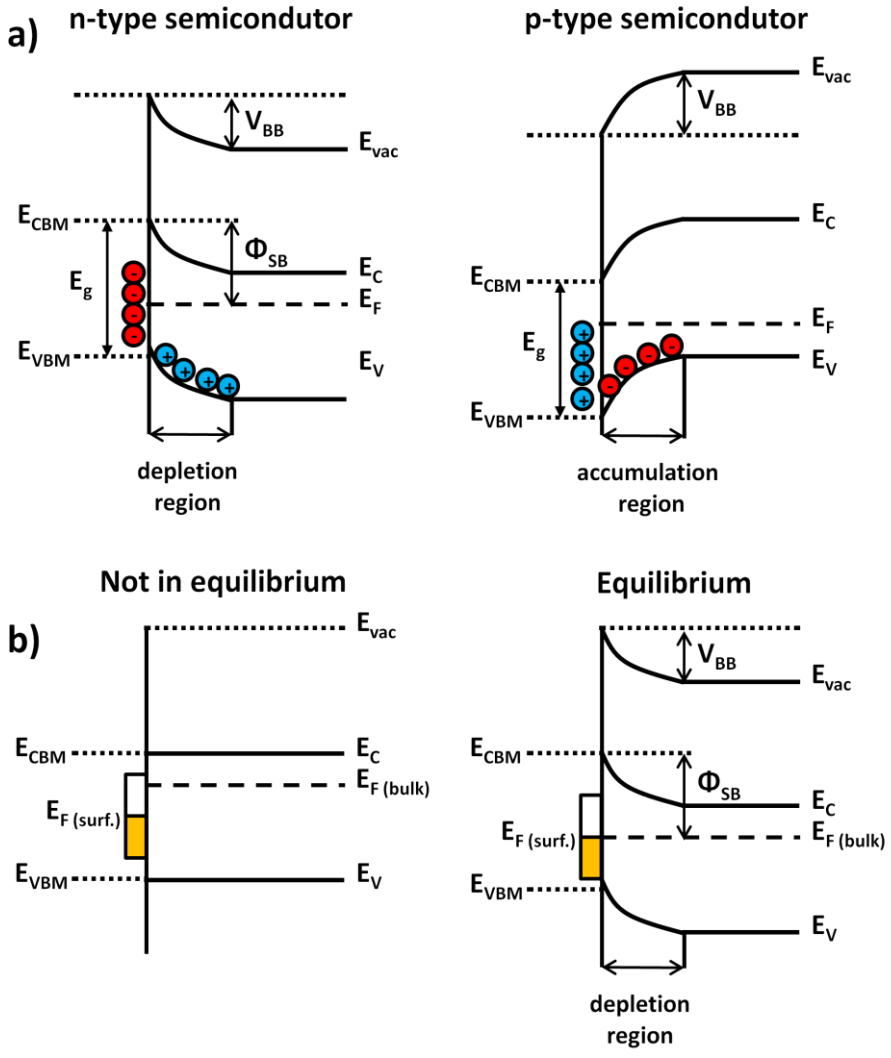

Figure 1.3 *Energy band diagrams of* **a)** *n- and p-type semiconductor contacts (equilibrium condition) and* **b)** *near the surface of a clean semiconductor (n-doped) before and after equilibrium of the bulk and surface E_F. E_{vac} is the vacuum energy, E_V and E_C are the energy of valence and conduction band minimum, respectively.*

When photons are absorbed or an electron flux (with suitable energy to promote an excitation in the material) impinges on the surface/interface of a semiconductor system, electron-hole pairs (excitons) are generated. The presence of an electric field (due to the unscreened charge close to the surface/interface) leads to the separation of the electron-hole pair in free carriers, which move in opposite directions[10,11,30]. For example, in the case of n-type semiconductors with upward band bending, the free electrons move toward the bulk and the free holes to the surface neutralizing, respectively, the excess of positive and negative charges. As a consequence, the degree of band bending is partially reduced (Figure 1.4). In other words, a change of the surface potential is induced by the photon or electron impinging flux. This effect is called surface photovoltage (SPV) in the case of photons or surface voltage (SV) in the case of electrons. Increasing the photon/electron flux the SPV/SV saturation can be achieved, completely flattening the energy bands. In this case, the SPV/SV value equals the band bending magnitude. Since the band flattening is induced by an external perturbation, the system will tend to restore the original condition and the SPV/SV effect decays in time. Temperature, dopant concentration, defects concentration, surface velocity recombination and the incident photons/electron flux, among others, are the important parameters in determining the magnitude and relaxation time of the SPV/SV[31-33]. The SPV/SV dynamics can occur in an extremely wide temporal range, from ps to seconds and more, depending on the condition of the system[31-35]. As a consequence, the efficiencies of carrier separation and injection at the interface are dependent on the evolution in time and magnitude of the SPV/SV.

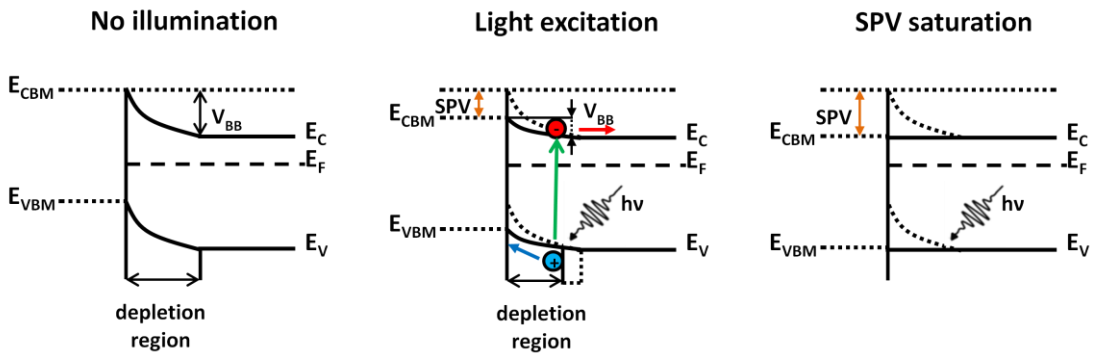

Figure 1.4 *Schematic diagrams of the surface photovoltage effect. Upward band bending in n-type semiconductor (No illumination); photons excitation produces free charge carriers resulting in a partial band flattening (Light excitation). By using intense light flux complete bands flattening is achieved (saturation SPV).*

In a conventional *p-n* junction photovoltaic cell made, for example, by silicon, the semiconductor assumes two roles at the same time: it harvests the incident sunlight and conducts the charge carriers produced under light excitation. To achieve good efficiency the photons have to be absorbed close to the *p-n* interface. Electron-hole pairs produced away from the junction must diffuse to the *p-n* contact where the local electrostatic field separates the charges. As a consequence, to avoid charge carrier recombination during diffusion the concentration of defects in the solid must be small[13,30]. This imposes severe requirements on the purity of the semiconductor material, rendering solid state devices of the conventional type more expensive. In contrast, molecular photovoltaic systems separate the functions of light absorption and carrier transport. Light-harvesting is carried out by a sensitizer which initiates electron transfer events leading to charge separation[30].

A detailed understanding of SPV/SV relaxation dynamics is fundamental not only in the view of technological applications but also experimentally. Several studies demonstrated the sensitivity of photoemission spectroscopy and inverse photoemission spectroscopy to this process[36-40]. Both occupied and unoccupied states, depending on the photon/electron flux shifts in energy from the equilibrium position, possibly leading to an incorrect evaluation of the electronic structure of the semiconductor. Considering its possible huge impact on steady-state measurements, even more carefulness has to be paid to this effect during pump and probe experiments. In the case of long-living SPV/SV relaxation dynamics, the assumption that the equilibrium condition of the system is restored within consequent pump pulses may lead to a misleading interpretation of the experimental results.

1.2.1 Transient SPV in pump-probe experiments

The SPV effect in inorganic semiconductors has been well established 30 years ago by photoemission studies[36,37]. However, despite the fundamental theory of the SPV, that has been well known for decades[41,42], only in recent years it has been possible to provide a detailed characterization of its relaxation dynamics and how different factors tune its evolution over time. Ultrafast time-resolved spectroscopy is nowadays a powerful tool in this field. Detailed characterization of the SPV relaxation dynamics in crystalline Si and its dependences on the incident photon flux, dopant concentration and surface termination have been addressed[33,43]. Its dependence on the temperature and adsorbate species in n- and p-doped GaN samples are reported, as well as the impact on the SPV relaxation dynamic in a GaP heterojunction[31,32,44]. One of the critical issues of the SPV dynamics is the extreme variability of its relaxation dynamics, which can differ by several orders of magnitude for a given semiconductor system and experimental condition (temperature, photon flux)[31-35]. Since the efficiency of the carrier injection and separation at the interface may change over time, due to the SPV effect, a careful evaluation of the magnitude and relaxation dynamics of the SPV is essential. Moreover, a correct evaluation of this effect is also fundamental in avoiding misleading interpretations of the experimental time-resolved data. For example, assuming that an SPV dynamic is present in addition to the dynamical process of interest, several different scenarios are possible in time-resolved experiments (Figure 1.5). In the

first case, the SPV relaxation dynamic is assumed faster than the time delay between consecutive probe pulses (or instrumental time resolution). The relaxation processes occur in two distinct temporal domains and can be easily disentangled between each other, representing a "safe" situation where the presence of the SPV effect is negligible.

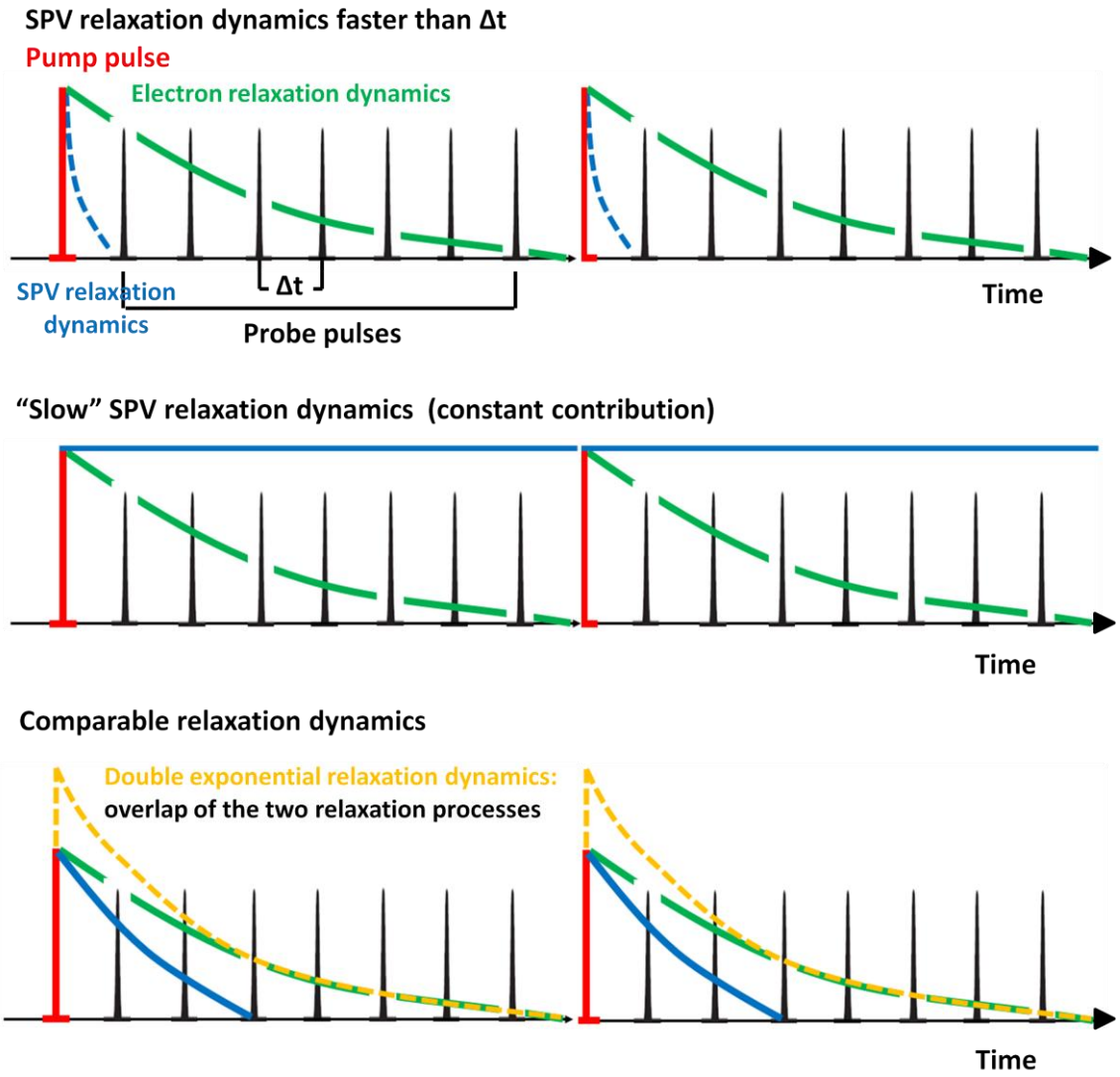

Figure 1.5 *Illustration of three possible scenarios performing time-resolved experiments where SPV dynamics are present in addition to the dynamical process of interest.*

An intermediate situation occurs when the SPV relaxation dynamic occurs in a different time domain to the main relaxation dynamic. A constant contribution to the relaxation signal will be observed in the experimental data. Knowing the steady-state SPV magnitude, the SPV dynamic can be easily disentangled from the main relaxation dynamics. The more complex scenario is when the two relaxation dynamics are comparable. Without detailed knowledge of the SPV effects in the system, it would be highly difficult to disentangle and correctly address the two dynamical processes. From the experimental point of view, those three different cases may coexist. For a given experimental condition (temperature, photon

flux used) the sample may not exhibit an SPV effect (or be negligible), initially leading to the detection of one relaxation dynamics. However, varying the experimental condition, i.e. lowering the temperature or increasing the incident photon, the SPV effect may occur. As will be shown in Chapter 4, depending on the experimental condition its magnitude and evolution over time can be substantially different. As a consequence, not consider nor properly evaluating the SPV effect may easily lead to a misleading interpretation of the experimental data.

References:

[1] C. Qian, J. Sun, and Y. Gao. Transport of charge carriers and optoelectronic applications of highly ordered metal phthalocyanine heterojunction thin films**.** *Phys. Chem. Chem. Phys.* **2021**, 23, 9631.

[2] H. Lim, S. Yang, S.-H. Lee, J.-Y. Lee, Y. Lee, A. B. Situmorang, Y.-H. Kim, and J. W. Kim. Influence of the metal phthalocyanine molecular orientation on charge separation at the organic donor/acceptor interface. *J. Mater. Chem. C*, **2021**, 9, 2156.

[3] C. Videlot, A. El Kassmi, and D. Fichou, Photovoltaic properties of octithiophene-based Schottky and p/n junction Cells: Influence of molecular orientation *Sol. Energy Mater. Sol. Cells*, **2000**, 63, 69-82.

[4] V. Coropceanu, J. Cornil, D. A. da Silva Filho, Y. Olivier, R. Silbey, and J.-L. Bredas. Charge transport in organic semiconductors**.** *Chem. Rev.*, **2007**, 107, 926-952.

[5] S. Duhm, G. Heimel, I. Salzmann, H. Glowatzki, R. L. Johnson, A. Vollmer, J. P. Rabe, and N. Koch. Orientation-dependent ionization energies and interface dipoles in ordered molecular assemblies. *Nat. Mater.* **2008**, 7, 326.

[6] T. Wang, T. R. Kafle, B. Kattel, and W.-L. Chan. Observation of an Ultrafast Exciton Hopping Channel in Organic Semiconducting Crystals. *J. Phys. Chem. C* **2016**, 120, 14, 7491–7499.

[7] A. Gadalla, J. B. Beaufrand, M, Bowen, S. Boukari, E. Beaurepaire, O. Crégut, M. Gallart, B. Honerlage and P. Gilliot. Ultrafast Optical Dynamics of Metal-Free and Cobalt Phthalocyanine Thin Films II: Study of Excited-State Dynamics. *J. Phys. Chem. C*, **2010**, 114, 17854–17863.

[8] W. Wu, N.M. Harrison and A. J. Fisher. Electronic structure and exchange interactions in cobalt phthalocyanine chains. *PRB*, **2013**, 88, 024426.

[9] H. Yoshida, Y. Tokura and T. Koda. Charge-transfer excitation bands in electro-absorption spectra of metal (Co, Ni, Cu, Zn)-phthalocyanine films. *Chemical Physics*, **1986**, 109, 375-382.

[10] Z. Zhang, and J. T. Yates, Jr. Band Bending in Semiconductors: Chemical and Physical Consequences at Surfaces and Interfaces. *Chem. Rev.* **2012**, 112, 5520−5551.

[11] H. Ishii, N. Hayashi, E. Ito, Y. Washizu, K. Sugi, Y. Kimura, M. Niwano, Y. Ouchi, and K. Seki. Kelvin probe study of band bending at organic semiconductor/metal interfaces: examination of Fermi level alignment. *Phys. Stat. Sol. (a)* **2004**, 201, 6, 1075–1094.

[12] M. Kasha. Energy Transfer Mechanisms and the Molecular Exciton Model for Molecular Aggregates Energy. Radiation Research **1963**, 20, 55-71.

[13] S. M. Sze, and Kwok K. Ng. Physics of Semiconductor Devices. John Wiley & Sons, Inc., **2007.**

[14] M. Knupfer. Exciton binding energies in organic semiconductors. *Appl. Phys. A* **2003**, 77, 623–626.

[15] M. Pope, and C. E. Swenberg. Electronic Processes in Organic Crystals and Polymers**.** Oxford University Press, **1999.**

[16] D. Potamianos, M. Nuber, A. Schletter, M. Schnitzenbaumer, M. Haimerl, P. Scigalla, M. Wörle, L. I. Wagner, R. Kienberger, and H. Iglev. Full Dynamics Description of Mg Phthalocyanine Crystalline and Amorphous Semiconductor Systems. *J. Phys. Chem. C* **2021**, 125, 18279−18286.

[17] M. Lia, W.-H. Lia, Y.-J. Hua, J. Lengb, W.-M. Tianb, C.-Y. Zhaob, J.-X. Liub, R.-R. Cuib, S.-Y. Jinb, C.-H. Chenga, and S.-L. Conga. Influence of the Molecular Stacking Pattern on the Excited State Dynamics of Copper Phthalocyanine Films. Chin. *J. Chem. Phys.* **2021**.

[18] M. C. Hanna, and A. J. Nozik. Solar Conversion Efficiency of Photovoltaic and Photoelectrolysis Cells with Carrier Multiplication Absorbers. *J. Appl. Phys.* **2006**, 100, 7, 074510.

[19] M.-H. Ha-Thi, N. Shafizadeh, L. Poisson, and B. Soep. An Efficient Indirect Mechanism for the Ultrafast Intersystem Crossing in Copper Porphyrins. *J. Phys. Chem. A* **2013**, 117, 8111−8118.

[20] M. Chergui, and E. Collet. Photoinduced Structural Dynamics of Molecular Systems Mapped by Time-Resolved X-ray Methods. *Chem. Rev.* **2017**, 117, 11025−11065.

[21] L. X. Chenwighard, J. H. Jäger, G. Jennings, D. J. Gosztola, A. Munkholmand, and J. P. Hessler. Capturing a Photoexcited Molecular Structure Through Time-Domain X-ray Absorption Fine Structure. *Science* **2001**, 292, 5515, 262-264.

[22] R. Natoli, and M. Benfatto. A Unifying Scheme of Interpretation of X-ray Absorption Spectra Based on the Multiple Scattering Theory. *Journal de Physique* **1986**, 12, 47, 11-23.

[23] B. W. Caplins, T. K. Mullenbach, R. J. Holmes, and D. A. Blank. Femtosecond to nanosecond excited state dynamics of vapor deposited copper phthalocyanine thin films**.** *Phys. Chem. Chem. Phys.* **2016**, 18, 11454.

[24] S. V. Rao, and D. N. Rao. Excited state dynamics in phthalocyanines studied using degenerate four wave mixing with incoherent light. *J. Porphyrins Phthalocyanines* **2002**, **6**, 233-237.

[25] J. McVie, R. S. Sinclair, and T. G. Truscott. Triplet states of copper and metal-free phthalocyanines**.** Faraday Trans.**1978**, 2, 74, 1870–1879.

[26] A. V. Nikolaitchik, O. Korth and M. A. J. Rodgers. Direct determination of nonradiative relaxation rates in nonfluorescent metallophthalocyanines**.** *J. Phys. Chem. A*, **1999**, 103, 7587–7596.

[27] O. Bram, thesis: Ultrafast Visible and Ultraviolet Fluorescence Studies of Molecular and Biological Sytems in Solution. Ecole polytechnique federale de Lausanne, **2011**.

[28] A. Popescu, R. A. Younts, B. Hoffman, T. McAfee, D. B. Dougherty, H. W. Ade, K. Gundogdu, and I. V. Bondarev. Monitoring Charge Separation Processes in Quasi-One-Dimensional Organic Crystalline Structures. *Nano Lett.* **2017**, 17, 6056−6061.

[29] A. A. Cordones, C. Das Pemmaraju, J. H. Lee, I. Zegkinoglou, M.-E. Ragoussi, F. J. Himpsel, G. de la Torre, and R. W. Schoenlein**.** Excited-State Charge Distribution of a Donor-π-Acceptor Zn Porphyrin Probed by N K-Edge Transient Absorption Spectroscopy. *J. Phys. Chem. Lett.* **2021**, 12, 1182−1188.

[30] T. Dittrich, and S. Fengler. *Surface Photovoltage Analysis of Photoactive Material*. World Scientific, **2020**.

[31] M. A. Reshchikov, M. Foussekis, and A. A. Baski. Surface photovoltage in undoped n -type GaN. *Journal of Applied Physics* **2010**, 107, 113535.

[32] M. Foussekis, J. D. McNamara, A. A. Baski, and M. A. Reshchikov. Temperature-dependent Kelvin probe measurements of band bending in p-type GaN. *Applied Physics Letters* **2012**, 101, 082104.

[33] D. Pierucci, M. G. Silly, H.Tissot, P. Hollander, F. Sirotti, and F. Rochet. Surface photovoltage dynamics at passivated silicon surfaces: influence of substrate doping and surface termination. *Faraday Discussions***, 2022.**

[34] Y. Yao, X. Sun, B. Ding, D.-L. Li, X. Hou, and C.-Q. Wu. A combined theoretical and experimental investigation on the transient photovoltage in organic photovoltaic cells. *Appl. Phys. Lett.* **2010**, 96, 203306.

[35] H. Lim, H. Kwon, S. K. Kim, and J. W. Kim. Delayed Triplet-State Formation through Hybrid Charge Transfer Exciton at Copper Phthalocyanine/GaAs Heterojunction. *J. Phys. Chem. Lett.* **2017**, 8, 4763−4768.

[36] R. Cimino, A. Giarante,, M. Alonso, and K. Horn. Photoemission study on non-equilibrium effects in metals on GaAs(110). Applied Surface Science **1992**, 56-58, 151-159.

[37] M. Alonso, R. Cimino, and K. Horn. Surface Photovoltage Effects in Photoemission from Metal-GaP(110) Interfaces: Importance for Band-Bending Evaluation. *PRL* **1990**, 64, 16.

[38] M. Cantoni, R. Bertacco, A. Brambilla, F. Ciccacci . Photon- and electron-induced surface voltage in electron spectroscopies on ZnSe(001). *Journal of Electron Spectroscopy and Related Phenomena* **2009**, 173, 84–87.

[39] M. Cantoni, R. Bertacco, A. Brambilla, M. Finazzi, L. Duò, F. Ciccacci, A. Verdini, L. Floreano, A. Morgante, M. Passoni, C. S. Casari, and A. Li Bassi. Fe nanoparticles on ZnSe: Reversible temperature dependence of the surface barrier potential. *PRB* **2012**, 85, 155456.

[40] B. Adamowicz, M. L. Grilli, M. Pedio, C. Ottaviani, A. Campo, M. Capozi, C. Quaresima, and P. Perfetti. Inverse Photoemission and Kelvin Probe Studies of the Au/GaP(110) Interface. *Vacuum* **1995** 46, 509-512.

[41] M. H. Hecht. Role of photocurrent in low-temperature photoemission studies of Schottky-barrier formation *Phys. Rev. B* **1990**, 41, 11, 7918–7922.

[42] M. H. Hecht. Time dependence of photovoltaic shifts in photoelectron spectroscopy of semiconductors. *Phys. Rev. B* **1991**, 43, 12102–12105.

[43] W. Widdra, D. Bröcker, T. Gießel, I. V. Hertel, W. Krüger, A. Liero, F. Noack, V. Petrov, D. Pop, P. M. Schmidt, R. Weber, I. Will, and B. Winter. Time-resolved core level photoemission: surface photovoltage dynamics of the SiO2/Si(100) interface. *Surface Science* **2003**, 543, 87–94.

[44] B. M. Marsh, B. R. Lamoureux, and S. R. Leone. Ultrafast time-resolved extreme ultraviolet (XUV) photoelectron spectroscopy of hole transfer in a Zn/n-GaP Schottky junction. *Struct. Dyn.* **2018**, 5, 054502.

2. Methods and experimental details

This chapter reports a brief overview of the experimental techniques and samples studied in this thesis work. The first part describes the general concepts of spectroscopic techniques such as X-ray and ultraviolet photoemission, inverse photoemission and X-ray absorption. A second section introduces the fundamental concepts of pump-probe techniques and which kind of information can be obtained on the excited state dynamics using time-resolved spectroscopies. A general overview of time-resolved photoemission, time-resolved X-ray absorption and transient absorption spectroscopies is discussed. Finally, the last part describes the preparation methods and the studied samples.

2.1 Photoemission spectroscopy

Nowadays, photoemission spectroscopy is one of the most widely used techniques in many laboratories and surface science. It is a photon in/ electron out technique based on the photoelectric effect. When monochromatic radiation, with energy hν>solid sample work function, is absorbed by the solid, photo-electrons are emitted. Collecting the emitted electrons by an analyser it is possible to reconstruct the electronic structure of the material. The resultant spectrum is the distribution of the emitted electrons as a function of their kinetic energy, E_K, according to:

$$E_K = h\nu - E_B - \Phi \qquad (2.1)$$

where E_B is the binding energy of the state from which the photoelectron is emitted and Φ is the work function of the analyser. Depending on the photon energy used, photoemission spectroscopy is divided into two categories: Ultraviolet photoemission spectroscopy (UPS), when ultra-violet sources are used (10 - 100 eV), or X-ray photoemission spectroscopy (XPS), if performed with X-ray sources (> 100 eV). The former allows to determine the electronic structure of the outmost electronic states of a material, and the latter provides information on the inner shell, the core levels. UPS and XPS are performed by exploiting conventional laboratory sources such as helium discharge lamps (He I hν = 21.2 eV) and X-ray tubes (e.g. Al Kα, hν = 1487 eV). However, both techniques highly benefit of the higher photon flux and energy tunability of synchrotron light sources. The photoemission process is illustrated in Figure 2.1. It is worth noting that in photoemission the final state has N-1 electrons, due to the generation of a hole in the process. XPS measurements are commonly used to obtain information on the sample composition. Each chemical element has a characteristic set of core levels with distinct binding energies. Depending on the chemical state and environment surrounding the emitting atom, slightly shifts in the core level binding energies can be observed for a given element. By an accurate XPS characterization, a complete description of the chemical state of the sample can be obtained.

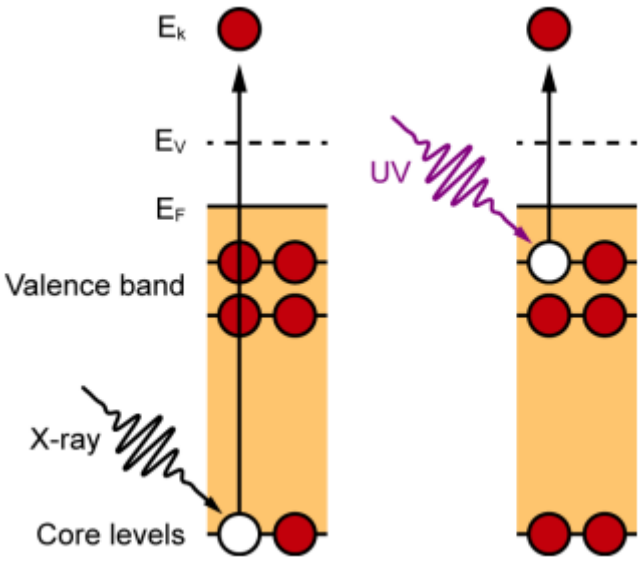

Figure 2.1 *Energy diagram of the photoemission process. In XPS (left) a monochromatic X-ray beam is used to ionize the core electrons, which are then detected as a function of their kinetic energy (E_K). UPS (right) is typically used to measure the valence band of the sample, as photons with energy in the UV range are not sufficient to eject the core electrons.*

UPS spectra, instead, are less element sensitive, because provide information on the outmost occupied electronic states of a material, which are the results of the mixing of atomic orbitals in the material. However, it is a fundamental tool for characterizing the electronic properties (and indirectly the optical properties) of the sample. In particular, the angular distribution of the UPS signal allows mapping the dispersion of the valence band states.

A fundamental property of photoemission spectroscopy is the surface sensitivity. Since photo-emitted electrons are probed, the possibility of their detection, in solids, is related to the inelastic mean free path, which is in the order of a few tens of Å for electrons with E_K = 20 - 1000 eV. In other words, these techniques provide information only on the first few layers of the samples (for photon energy in the soft X-ray range). For this reason, XPS and UPS are widely used to characterise thin films and molecular adsorbates. A more detailed description of these techniques can be found elsewhere[1,2].

The UPS measurements reported in this thesis were performed at the "Laboratory of quantum optics" of CITIUS in Nova Gorica. The UPS spectra were obtained using a commercial Ti:Sa laser source (Coherent, Legend Elite Duo), from which high-order harmonics were generated and monochormatized[3]. HH35 ($h\upsilon \approx 38.5$ eV) was selected: the overall resolution of the probe beam was 130 meV. The spectra were recorded in normal emission geometry, by using an R3000 hemispherical electron energy spectrometer from VG-Scienta. XPS measurements were performed at the ALOISA beamline, Elettra synchrotron (ANCHOR-SUNDYN endstation)[4]. The spectra were recorded in normal emission geometry, by using a 150 mm hemispheric electron analyser SPECS Phoibos 150.

The UPS and XPS spectra were calibrated by measuring the E_F and the Au 4f core level, respectively, of a polycristalline Au reference in direct contact with the samples.

2.2 Inverse photoemission spectroscopy

Inverse photoemission spectroscopy (IPES), contrary to photoemission, is an electron in-photon out technique, which provides information on the unoccupied density of states of a material. For this reason, it is commonly used as a complementary technique to photoemission. Figure 2.2 shows the schematic representation of the IPES experimental setup.

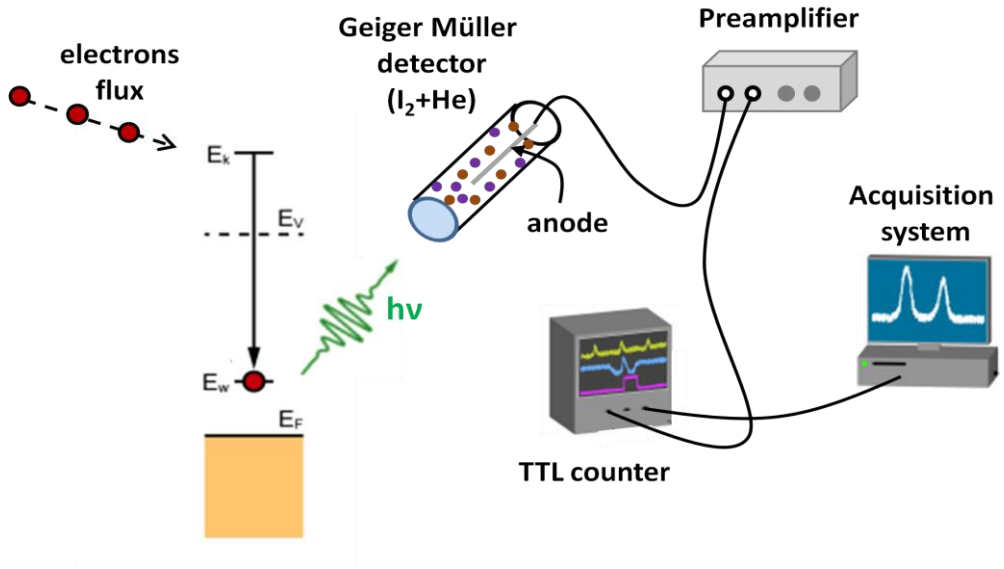

Figure2.2 *Schematic representation of the IPES setup. The emitted photons are detected by a Geiger-Müller detector. By ionization of the I_2 gas a pulse is produced at the anode. The pulse is then transformed in a TTL pulse by a preamplifier and sent to a TTL counter, which is connected to the acquisition system.*

An electron gun provides a collimated beam of low-energy electrons (5 eV to 20eV). The electrons impinging onto the sample are coupled to a high energy unoccupied state (E_K) and relax to a lower unoccupied state (E_W) emitting photons with energy equal to the energy difference of the empty states. The emitted photons are then detected by a Geiger-Müller detector which acts as a band-pass detector selecting photons with fixed energy. The photons interacting with the gas within the detector tube (I_2 mixed with He) generate a pulse at the detector anode. The detector pulses are sent to a preamplifier and then converted into a voltage pulse (transistor-transistor logic signal – TTL). TTL circuits are also used to reject the noise level of pulses. The number of TTL signals is counted by the counter and sent to the computer. Knowing the energy of the electrons sent to the sample

(E_K) and of the emitted photons (hν), the energy position of the unoccupied states is given by the conservation of energy as:

$$E_K = E_W + h\nu \qquad (2.2)$$

The band-pass filter of the Geiger-Müller tube is given by the combined use of a gas mixture of I_2 and He together with an SrF_2 window (or CaF_2), selecting photons of about 9.5 eV energy. The presence of He as quenching gas is necessary to improve the dead time as well as improve the count rate. The I_2 acts as a low energy limiter: only photons with energy higher than ~9.3 eV can trigger the ionization event producing an electric current in the cathode. The SrF_2 is the high energy limiter, letting pass only electrons with energy lower than ~9.7 eV. The maximum transmission combining the two elements is at 9.5 eV. Due to the low kinetic energy of the incident electrons, the penetration depth is only a few atomic layers, resulting in a surface-sensitive technique. In IPES the final state corresponds to an N+1 electronic state. In first approximation the spectrum provide the electronic density of the empty states of the system.

The IPES measurements of CoPc films, shown in Chapter 3, were performed at the SIPE laboratory, CNR-IOM in Trieste. The collimated electron beam was provided by a homemade Erdman-Zipf electron gun. The beam divergence was ~2°. Photons emitted by the sample were collected by a homemade Geiger-Müller type detector with a He-I_2 gas mixture and an SrF_2 entrance window filtering photons of energy hν= 9.5 eV. The experimental resolution was below 0.30 eV, as measured by the Fermi level (E_F) onset of a clean Ta foil. The IPES spectra were normalized at each point to the incident electron beam current.

2.3 X-ray absorption spectroscopy

Near-edge X-ray absorption fine structure, commonly known as NEXAFS, or just XAS, is a technique in which by scanning with photon energies around the absorption edge of a specific element, a spectrum proportional to the absorption coefficient of the sample is obtained. Therefore, intense and tunable X-ray sources are required, and XAS experiments are usually performed at synchrotron facilities. According to the Fermi Golden formula, dipole selection rules and the local character of the initial core state dominate the transitions detected by XAS. The absorption coefficient for specific photon energy is related to the absorption cross-section, σ_x, which is the number of electrons excited per unit time divided by the number of incident photons per unit time per unit area. Considering a transition from an initial state $|i\rangle$ to a final state $|f\rangle$ promoted by a plane electromagnetic wave, under the dipole approximation it is obtained:

$$\sigma_x \propto |\langle f|\boldsymbol{\eta} \cdot \mathbf{p}|i\rangle|^2 \rho_f(E) \qquad (2.3)$$

where η is the polarization unit vector, p is the sum of the linear momentum operators of the electrons and ρ_f (E) is the energy joint density of final states. In XAS, the initial state $|i\rangle$ is generally a localized atomic core level, while $|f\rangle$ can represent either a bound or a continuum state. A picture of the absorption process from a diatomic molecule is shown in Figure 2.3. In the region below the vacuum level, the absorption spectrum is dominated by transitions to the unoccupied molecular orbitals (typically the π* transitions in a molecule), while transitions to the continuum (typically the σ* transitions) start contributing as the photon energy approaches the ionization potential.

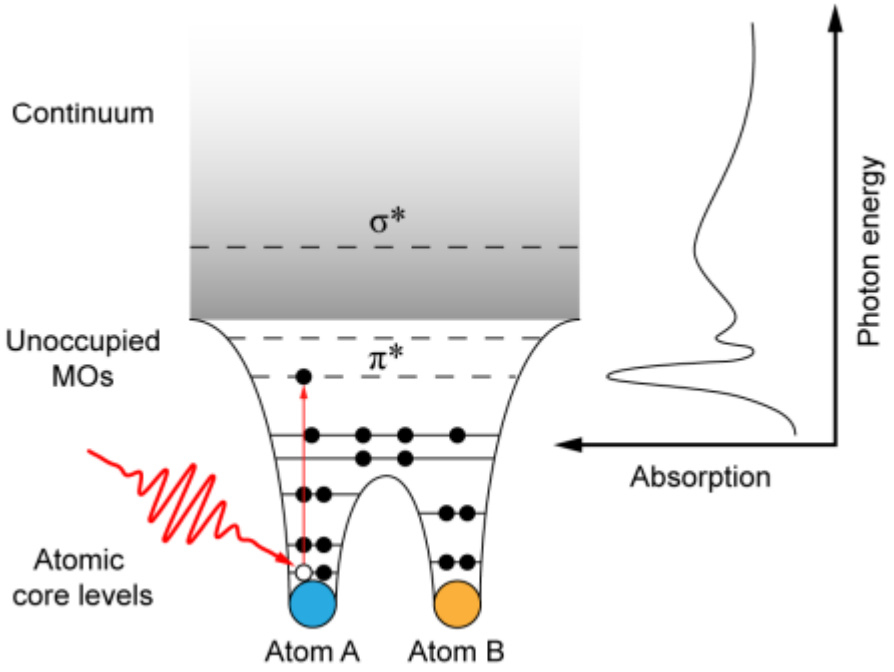

Figure 2.3 *Sketch of X-ray absorption spectroscopy on a diatomic molecule. Scanning the photon energy of the incoming beam through an absorption edge of the atom A, due to transitions from the localized core level to unoccupied molecular orbitals, a structured absorption signal is detected.*

By analysing the XAS spectra both chemical and structural information on the system can be extracted. In addition to the element sensitivity, another advantage of this technique is the possibility to gain information on the geometric structure/orientation of the sample, as in the case of molecular film. Since the XAS signal is obtained from excitation of a core level with a defined symmetry, the most intense features are due to transitions to unoccupied states following the symmetry selection rules (i.e. $\Delta\ell = \pm 1$). Molecular orbitals are highly oriented as π and σ orbitals (and the corresponding anti-bonding orbitals π* and σ*), directed orthogonally and along with the atomic bonds, respectively. As a consequence, by polarization-dependent measurements, the molecular orientation on surfaces can be readily determined[6]. Recalling eq. 2.3, the most intense features of a K-edge are due to core transitions from 1s → p-like final states, while in the L_3-edge the feature in the spectrum are due to 2p → d-like final states if the polarization vector, η, of

the incoming beam is oriented along the final state orbital direction (being the channel 2p →s-like state less intense of a factor 5). Therefore, in these cases, the intensity of XAS resonances is a function of the incidence angle of the incoming polarized X-ray beam. Like the photoemission case, in XAS measurements a core hole is generated. In the single-particle approximation, the final state is described by a core hole and an excited photo-electron. The core hole can be filled by an electron from an "external" shell followed by a radiative (photon) or Auger process. Therefore, in XAS measurements the signal can be measured by fluorescence photons, Auger electrons, or inelastically scattered photo-electrons (i.e. the current from the sample or the secondary electrons) with different sampling depths. Depending on the detection mode, XAS mode is called fluorescence yield (FY), total or partial electron yield (TEY or PEY) and Auger electron yield (AEY). One detection mode can be more suitable than another depending on the case. For example, in few layer low-Z molecules adsorbed on a surface, the most suitable approach is to measure the AEY (sampling depth about 1 nm). After the absorption of an X-ray photon, the system is left with a core hole, and the Auger decay is the most favourable recombination process for K-edge absorption in low-Z atoms. FY can be useful to overcome the high surface sensitivity of the photo-electron detection (sampling depth in the tens-hundreds of nm range in the soft X), having a signal related to the absorption length of the photons[7] in the material rather than the mean free path of electrons. For a complete review of principles, techniques and applications of XAS spectroscopy see Stöhr's book[8].

2.4 Pump-probe applied to spectroscopies

As suggested by the name in pump and probe (PP) techniques two beams are used, the pump beam and the probe beam, both interacting with the sample. In conventional PP experiments, a laser pulse (pump) excites a transient state while a probe (light in the UV-Vis or X-ray energy range), at a fixed delay time relative to the pump pulse, Δt, probes the evolution over the time of non-equilibrium states. In laser-based time-resolved measurements, the pump and probe pulses are generated by splitting the output beam of a single laser source, and the synchronization between the two beams is automatically achieved. The delay time is easily varied through motorized translation stages. A more complicated scheme is required for the synchronization of the beams in laser pump-X-ray probe experiments, as different sources are required to generate them. In this case, X-ray-based PP techniques strongly benefited from synchrotron facilities[9-13], exploiting their high brilliance and high repetition rate (multi-bunch operation modes[9]). Depending on the dynamic process to study, different time scales and PP techniques may be required or preferred. X-ray-based time-resolved experiments performed at the synchrotron, despite the great advantages in the beam properties, are limited by the time resolution of tens of ps, due to the intrinsic pulse duration of the probe. At laser-based time-resolved facilities, as free-electron lasers (whose use is out of this thesis work), a higher temporal resolution of 10-100 fs is achievable[14-16]. However, the photon energy range available is usually more limited than for synchrotrons. In many cases, a multi-technique approach may be the best

solution to completely clarify the excited states dynamics picture of the material, providing complementary information from both these classes of techniques.

2.4.1 Time-resolved X-ray and ultraviolet photoemission spectroscopies

In time-resolved photoemission spectroscopies, the probe can be either an X-ray or a laser beam. In the former case it is called time-resolved X-ray photoemission (TR-XPS), and in the latter time-resolved ultraviolet photoemission (TR-UPS). Similarly to steady-state photoemission, they provide information on the sample electronic structure. Depending on the technique chosen, the evolution in time of the core levels or valence band can be probed in different time domains. TR-UPS is a technique particularly convenient in characterizing the excited state dynamics in organic materials. Electron dynamical processes are generally extremely fast, occurring in the fs-ps time scales. Moreover, due to the localized nature of the frontier orbitals, the optical pump pulse selectively promotes transitions from specific molecular orbitals (MO). TR-UPS experiments directly probe the evolution in time of the states excited by the pump pulse, gaining direct information on the highest occupied MO (HOMO) and lowest unoccupied MO (LUMO). After pump excitation the LUMO is populated and photoelectrons from this state can be detected. Since the frontier orbitals originated from the mixing of atomic orbitals of different elements in the sample, UPS usually is not an element-sensitive technique. However, in some cases, exploiting the different dependence of the element cross-section on the probe photon energy, it is possible to discriminate the specific contribution of the elements to the dynamical processes. By changing the probe photon energy, the cross-section of one atomic orbital (which contributes to the MO of the material) may be drastically enhanced or quenched with respect to other elements. In this case, the different atomic contributions to the MO can be distinguished, allowing to highlight an eventual predominant atomic character in the excited state dynamics.

The TR-UPS measurements reported in this thesis were performed at the “Laboratory of quantum optics” of CITIUS in Nova Gorica. A commercial Ti:Sa laser source (Coherent, Legend Elite Duo), from which high order harmonics were generated and monochormatized3. HH35 ($h\upsilon \approx 38.5$ eV) was selected as the probe pulse: the overall resolution of the probe beam was 130 meV. The spectra were recorded in normal emission geometry, by using an R3000 hemispherical electron energy spectrometer from VG-Scienta. The excitation (pump) pulses were generated from an OPA (Coherent OPerA) set at 610 nm (2.0 eV). A detailed description of the experimental setup can be found in ref. 3.

TR-XPS spectroscopy has the intrinsic advantage of being element-sensitive. It is used to characterize phase-to-phase transitions, chemical and photo-reactions, as well as charge and surface photovoltage effects. However, as mentioned above TR-XPS experiments at synchrotron facilities suffer from a low time resolution of 50-100 ps, which implies limitations in the detectable dynamical processes. Furthermore, due to the finite flight time of low-energy electrons in the hemispheric analyser used as probe detector, usually, it is not possible to completely discriminate the electrons emitted from the consecutive pulses

normally delivered in the multi-bunch (MB) operation. To overcome this limitation, a single bunch is used synchronized with the laser pulse. Hence, special filling modes of the storage ring are required, the single bunch (SB) or the hybrid bunch mode (HB). In HB a single electron bunch is placed in the dark gap of the multi-bunch distribution. On the other hand, in SB only one bunch per revolution is injected. However, the low ring current in SB to HB represents an issue for most of the users at a synchrotron facility, who typically apply the high photon flux. The HB is therefore the preferred operation mode. In both cases, the count rate when detecting only the single bunch will be roughly 100 times lower if compared to standard multi-bunch measurements.

TR-XPS measurements reported in this thesis were performed at the ALOISA beamline, Elettra synchrotron (ANCHOR-SUNDYN end-station). The end-station is equipped with a Yb:YAG fibre laser (Amplitude Systèmes, Tangerine HP), with a fundamental wavelength of 1030 nm. Non-linear beta barium borate (BBO) crystals were used for generating 3rd harmonics up to the 4th (343 nm) as pump pulse. Synchrotron X-ray, hν=400 eV and hν=650 eV of photon energy, were used as probe pulses. A detailed description of the experimental setup can be found in ref. 4.

2.4.2 Time-resolved X-ray absorption spectroscopy

As X-ray based technique, time-resolved X-ray absorption spectroscopy (TR-XAS) requires a source of intense and energy-tunable X-ray pulses as in the case of synchrotron facilities. As discussed in section 2.3, XAS can provide information about the unoccupied states, and the chemical and structural properties of the system. Since TR-XAS is an "extension" of XAS, similar information is obtained for the sample in the excited state configuration as a function of the time. TR-XAS experiments probe core level transitions to unoccupied conduction band (or antibonding) states. The region above the edge, up to 30-60 eV, is called NEXAFS (near edge X-ray absorption fine structure). NEXAFS can be interpreted as the local joint density of states or in the framework of real space scattering theory, being both frameworks analytically equivalent[17]. In this case the NEXAFS signal is due to the interference of the outgoing photoelectron wave, generated from the absorbing atom, with the wave that is backscattered by the neighbouring atoms. For this reason, XAS provides structural information and by TR-XAS it is possible to study the evolution in time of photo-induced lattice (or molecular in the case of organics) distortion and expansion as well as heating effects[18]. The promotion of an electron from core levels to a "bound" unoccupied state implies the possibility to gain specific information on the unoccupied states involved in the relaxation processes. Furthermore, in the case of samples with highly oriented orbitals, by exploiting their dependence on the X-ray polarization it is possible to selectively enhance specific resonance peaks allowing better detection of the relaxation dynamics. As an X-ray-based technique, all these advantages can be additionally exploited in an element-sensitive way.

The multi-bunch mode operating at synchrotrons allows observing the complete dynamical evolution at once between consecutive pump pulses. By choosing different detection modes AEY or FY it is possible to selectively study the sample surface or gain

information on the bulk properties of the system. Moreover, the FY detection approach fully exploits the available X-ray photon flux at a high repetition rate providing continuous snapshots of the transient state. TR-XAS experiments shown in this thesis were performed on the new TR-XAS end-station currently in commissioning at the BACH beamline, Elettra synchrotron. The commissioning of this novel experimental chamber was one of the main goals of my PhD. TR-XAS measurements were performed in FY mode using a micro-channel plate, Hamamatsu F4655-13. A detailed description of the end-station setup and preliminar results are discussed in the Chapter 5.

2.4.3 Transient absorption spectroscopy

Transient absorption spectroscopy (TAS) is a laser-based pump-probe technique, in which after pump excitation the optical probe pulse measures the linear absorption spectrum of the excited state[19]. The TAS spectra are then obtained by the difference between the excited state and the ground state absorption spectra (measured before the pump excitation). Usually, the pump pulse photon energy corresponds to a strong optical absorption feature of the sample. The probe pulse is a continuum range of wavelength which scans the sample over the spectral region of interest (UV-Vis) over time. The measurement can be performed in reflection or transmission mode depending on the sample characteristic (for opaque samples reflection mode is necessary).

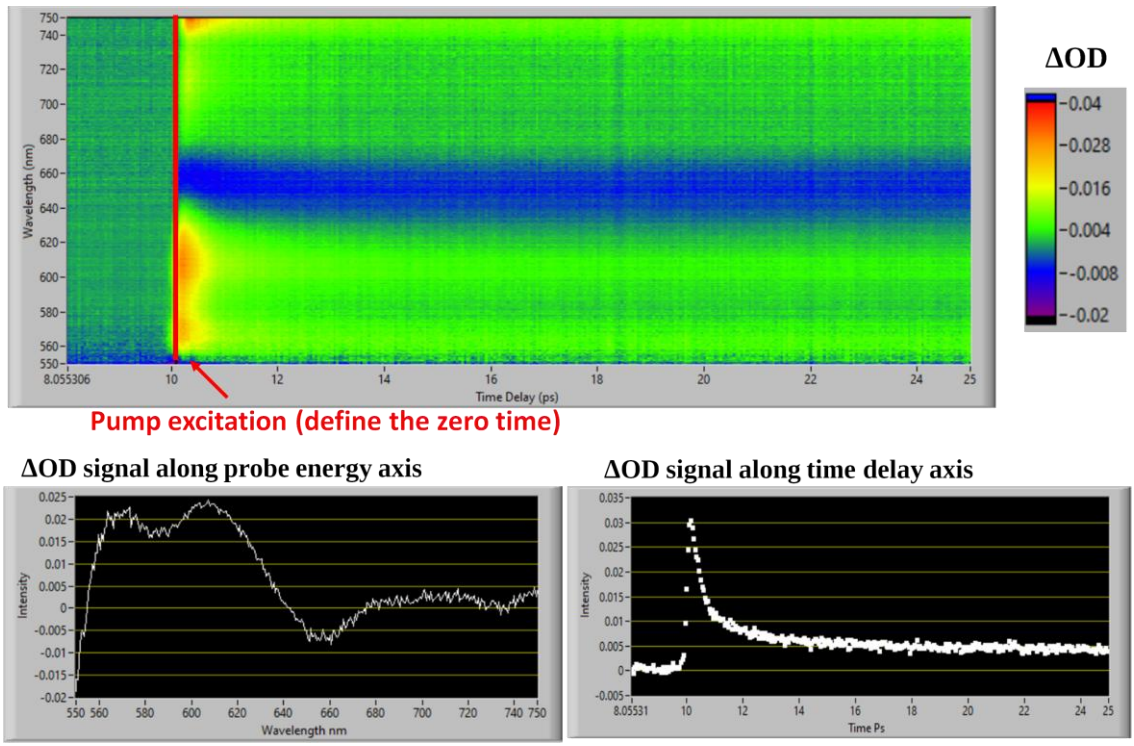

Figure 2.4 *Raw data obtained in a TAS experiments as 3D matrix where the ΔOD signal is plotted in false color scale as a function of the probe photon energy and time delay between pump and probe beam* ***(top)****. By extracting the*

ΔOD along the energy axis the differential spectra can be visualised for fixed time delay ***(bottom left)****. By extracting the ΔOD along the time delay axis it is shown the decay curve for fixed probe energy* ***(bottom right)***

Figure 2.4a shows an example of raw data obtained by TAS measurement. In TAS spectra, the differential optical density (ΔOD) signal is represented as a function of the time delay between the pump and probe beams and the spectral energy region mapped by the probe pulse. The differential spectrum of the sample is obtained according to the equation:

$$\Delta OD = -\log\left(\frac{I(t)}{I_0}\right) \qquad (2.4)$$

where I(t) and I_0 are the detected probe intensity signal with and without sample excitation by pump pulse, respectively. By extracting the ΔOD signal along the probe wavelength (or energy) range axis the differential spectra at a fixed time delay can be visualized. Negative and positive signals can be observed, called absorption bleaching and induced absorption signal, respectively. As general rule, absorption bleaching signals are due to the bleaching of the ground state after pump excitation: the depopulation of the ground states by the pump pulse reduces the transition probability and the excited state of the sample absorbs less in that spectral region. On the other hand, the population of unoccupied states by the pump pulse may lead to additional absorption processes not directly possible from the ground state configuration (at fixed pump photon energy). Therefore, additional transitions from the excited state to a high energy excited state may occur, leading to higher sample absorption of the probe pulse in a specific spectral range. This is called induced absorption. An illustration of the two processes is shown in Figure 2.5.

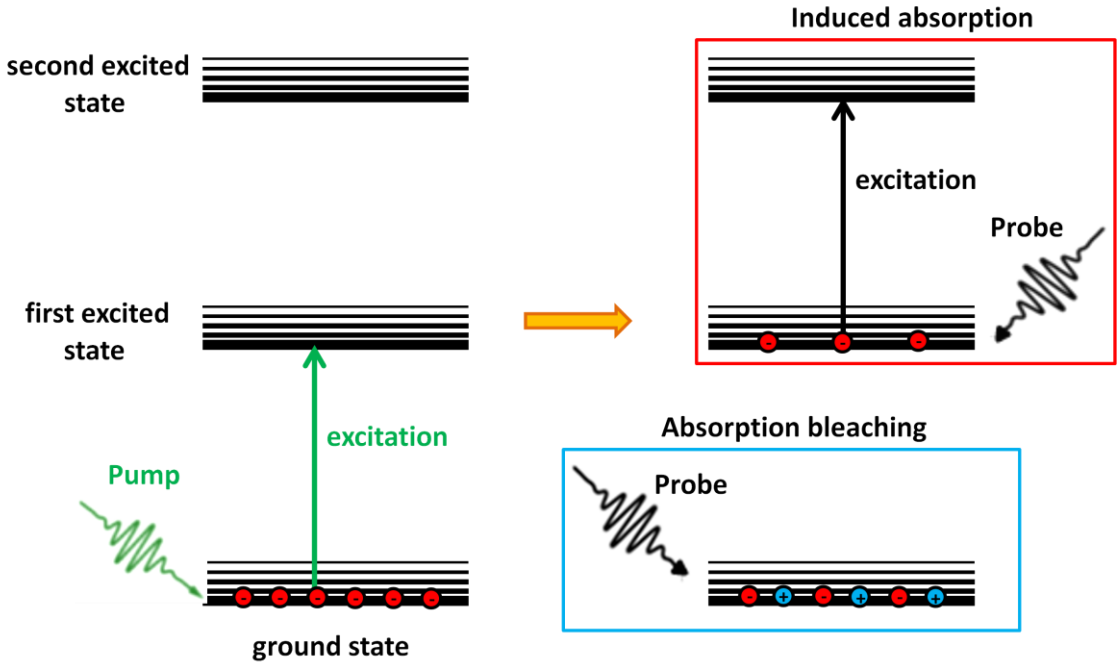

Figure 2.5 *Sketch of the absorption bleaching and induced absorption. After pump excitation the population of the ground state is reduced and electrons are*

promoted to the first unoccupied excited state. As a consequence, the transition probability of excitations from the ground state is lower (lower absorption), and according to eq. 2.4 a negative signal is observed (absorption bleaching). On the other hand, the occupancy of excited states (previously empty) leads to the possibility of new transitions from the first excited state to a higher excited state (higher absorption) and a positive ΔOD signal is detected (induced absorption)

By extracting the ΔOD signal along the time delay axis, it is obtained the decay curve of the ΔOD signal for fixed probe energy. The analysis of the decays curve provides quantitative information on the relaxation dynamics of the system, such as the number of processes that occurred and the relative decay time. The decay time, namely τ in the following, is defined as the time in which the differential signal decreases of a natural exponential factor *e* (Euler's number). The τ value is obtained fitting the ΔOD decay curves as a function of the time delay by mono or multi-exponential function according to:

$$\Delta OD = \sum_n A_n \, e^{-\frac{t}{\tau_n}} + C \qquad (2.5)$$

where A_n and τ_n are the contributions and decay time of the n-th exponential decay process and C is a constant value which describes a slower dynamics in a longer time domain to the experimental time window. The number of detected dynamical processes is given by the number of exponential functions used to fit the decay curve. However, it should be stressed that eq. 2.5, in some cases, could be an approximation of the effective relaxation dynamics. The fitting of decay curves by using eq. 2.5 implies assuming that the decay of all dynamical processes starts soon after the pump excitation, which is not always true.

TAS measurements in the Vis/IR range (from 1.12 eV to 2.34 eV) were performed at the "Ultrafast Laser Micro and Nano processing" laboratory of the Foundation for Research and Technology – Hellas research facility in Crete, Greece. The Femtosecond laser pulses were generated using a (Yb:KGW) femtosecond laser source with a pulse duration of 170 fs, 1 kHz repetition rate, and 1.21 eV of fundamental wavelength. An OPA was used to select photon energies of 1.21 eV, 2.41 eV and 3.1 eV for the pump pulses. For the probe pulses, a supercontinuum white light in the 1.12 eV to 2.34 eV range of wavelengths was generated using a YAG crystal. The time resolution was 250 fs. The experiments were performed either in reflection or transmission geometry mode.

2.5 Samples preparation

The experimental procedures used to obtain the samples studied in this thesis work are reported in the following.

2.5.1 Organic thin films: cobalt phthalocyanine and copper phthalocyanine

Metal phthalocyanines exhibit two important polymorphs called α– and β-phases. Both have similar herringbone structures but differ in their tilt angle of the b-axis to the molecular plane. The β-phase can be easily differentiated from the α-phase by structure, magneto-optical and morphological properties. The α-phase can have a brickstone or herringbone structure[20] (see Chapter 3).

The cobalt phthalocyanine (CoPc), β-form powder, was purchased from Sigma Aldrich, dye content 97%. CoPc deposition was performed by thermal sublimation from resistively heated quartz crucibles in ultrahigh vacuum UHV conditions ($<10^{-9}$ mbar). CoPc thin films were grown onto three different substrates, Au(111), graphene (Gr) and indium thin oxide (ITO). Before the deposition, the Au(111) surface was reconstructed by several Ar sputtering and annealing cycles in UHV. The Gr substrate was produced by the polymer transfer method of commercial Gr, purchased from Graphenea S.A., on a bulk Si wafer[21]. The ITO surface was rinsed using acetone and distilled water. The CoPc film growth was performed at a low deposition rate of 2 Å min^{-1}. The film thickness was measured via oscillating quartz microbalance after a degassing of the source at T lower than the sublimation temperature, obtaining CoPc films of 40 nm nominal thickness. A detailed characterisation of the structural and electronic properties of the films is reported in Chapter 3. XAS, XPS, UPS, IPES, TAS and TR-PES measurements were used to characterise the properties of the CoPc films. The relative laboratories and experimental setup used for each technique are reported in the previous section "Experimental Methods".

The copper phthalocyanine (CuPc), β-form powder, was purchased from Sigma Aldrich, dye content >99%. Similarly to the CoPc growth, the CuPc thin film was grown by thermal evaporation in ultrahigh vacuum (10^{-9} mbar) conditions on a SiO_2/p-Si(100) substrate at room temperature. The thickness of the films was monitored *in situ* using a quartz microbalance, obtaining a CuPc film of 2.2 nm nominal thickness. SiO_2/p-Si(100) substrate (details on the substrate properties are discussed in the next section 2.5.2 and Chapter 4) was annealed at 800 K before the deposition to remove the contaminant of the controlled oxide layer (obtained by standard Kirachi procedure) of about 2 nm. A detailed characterisation of the CuPc thin film and the SiO_2/p-Si(100) substrate electronic properties was performed by high-resolution XPS and TR-XPS at the ALOISA beamline, Elettra synchrotron (ANCHOR-SUNDYN end-station).

2.5.2 SiO_2/Si(100) systems

The commercial p-doped (B) and n-doped (As) SiO_2/Si(100) samples have dopant concentration of $8x10^{14}$ cm^{-3} (16.85 Ω×cm) and of $1.6×10^{19}$ cm^{-3} (0.004 Ω×cm), respectively. The dopant concentration was calculated from the sample resistivity[22]. Both samples were annealed at 800 K for 3 hours. The SiO_2/p-Si(100) sample after a detailed characterisation (see Chapter 4 section 4.4) by high-resolution XPS was used as the substrate for the growth of the CuPc thin film described in the previous section 2.5.1.

High-resolution XPS and TR-XPS of the SiO_2/Si(100) systems were performed at the ALOISA beamline, Elettra synchrotron (ANCHOR-SUNDYN endstation). A detailed discussion of the characterisation of the samples is reported in Chapter 4 sections 4.4.

References:

[1] C. S. Fadley, S. Manson, D. Dill. *Electron spectroscopy: Theory, techniques and applications*. Academic Press London, **1978**.

[2] A. G. Shard. Practical guides for x-ray photoelectron spectroscopy: Quantitative XPS. J. Vac. Sci. Technol. A 38 **2020**, 041201.

[3] C. Grazioli, C. Callegari, A. Ciavardini, M. Coreno, F. Frassetto,, D. Gauthier, D. Golob, R. Ivanov, A. Kivimäki, B. Mahieu, B. Bučar, M. Merhar, P. Miotti, L. Poletto, E. Polo, B. Ressel, C. Spezzani, and G. De Ninno. CITIUS: an infrared-extreme ultraviolet light source for fundamental and applied ultrafast science. *Review of Scientific Instruments* **2014**, 85, 023104.

[4] R. Costantini, M. Stredansky, D. Cvetko, G. Kladnik, A. Verdini, P. Sigalotti, F. Cilento, F. Salvador, A. De Luisa, D. Benedetti, L. Floreano, A. Morgante, A. Cossaro, and M. Dell'Angela. ANCHOR-SUNDYN: A novel endstation for time resolved spectroscopy at the ALOISA beamline. *Journal of Electron Spectroscopy and Related Phenomena* **2018**, 229, 7-12.

[5] J.C.Fuggle, and J.E. Inglesfield. *Unoccupied Electronic States*. Springer Verlag, Berlin **1992**.

[6] J. Stöhr, and D. A. Outka. Determination of molecular orientations on surfaces from the angular dependence of near-edge x-ray-absorption fine-structure spectra. *PRB* **1987**, *36*, 7891–7905.

[7] https://henke.lbl.gov/optical_constants

[8] J. Stöhr. *NEXAFS Spectroscopy*. Springer Series in Surface Sciences; Springer Berlin Heidelberg: Berlin, Heidelberg, **1992**.

[9] L. Stebel, M. Malvestuto, V. Capogrosso, P. Sigalotti, B. Ressel, F. Bondino, E. Magnano, G. Cautero, and F. Parmigiani. Time-resolved soft x-ray absorption setup using multibunch operation modes at synchrotrons. *Review of Scientific Instruments* **2011**, *82*, 123109-44913.

[10] A. M. March, A. Stickrath, G. Doumy, E. P. Kanter, B. Krässig, S. H. Southworth, K. Attenkofer, C. A. Kurtz, L. X. Chen, and L. Young. Development of high-repetition-rate laser pump/x-ray probe methodologies for synchrotron facilities. *Review of Scientific Instruments* **2011**, *82*, 073110.

[11] A. Shavorskiy et al. Sub-nanosecond time-resolved ambient-pressure X-ray photoelectron spectroscopy setup for pulsed and constant wave X-ray light sources. *Review of Scientific Instruments* **2014**, *85*.

[12] G. Vankó, P. Glatzel, V.-T. Pham, R. Abela, D. Grolimund, C. N. Borca, S. L. Johnson, C. J. Milne, and C. Bressler. Picosecond Time-Resolved X-Ray Emission Spectroscopy: Ultrafast Spin-State Determination in an Iron Complex. *Angewandte Chemie International Edition* **2010**, *49*, 5910-5912.

[13] K. Zhang, M. F. Lin, E. S. Ryland, M. A. Verkamp, K. Benke, F. M. De Groot, G. S. Girolami, and J. Vura-Weis. Shrinking the Synchrotron: Tabletop Extreme Ultraviolet Absorption of Transition-Metal Complexes. *Journal of Physical Chemistry Letters* **2016**, *7*, 3383-3387.

[14] A. Pietzsch, A. Föhlisch, M. Beye, M. Deppe, F. Hennies, M. Nagasono, E. Suljoti, W. Wurth, C. Gahl, K. Döbrich, and A. Melnikov. Towards time resolved core level photoelectron spectroscopy with femtosecond x-ray free-electron lasers. *New Journal of Physics* **2008**, *10*, 033004.

[15] H.T. Lemke et al. Femtosecond x-ray absorption spectroscopy at a hard x-ray free electron laser: Application to spin crossover dynamics. *Journal of Physical Chemistry A* **2013**, *117*, 735-740.

[16] S. Hellmann, C. Sohrt, M. Beye, T. Rohwer, F. Sorgenfrei, M. Marczynski-Bühlow, M. Kalläne, H. Redlin, F. Hennies, M. Bauer, A. Föhlisch, L. Kipp, W. Wurth, and K. Rossnagel. Time-resolved x-ray photoelectron spectroscopy at FLASH. *New Journal of Physics* **2012**, *14*, 013062.

[17] R. Natoli, and M. Benfatto. A Unifying Scheme of Interpretation of X-ray Absorption Spectra Based on the Multiple Scattering Theory. *Journal de Physique* **1986**, 12, 47, 11-23.

[18] W. Gawelda, V. T. Pham, M. Benfatto, Y. Zaushytsin, M. Kaiser, D. Grolimund, S. Johnson, R. Abela, C. Bressler, and M. Chergui. Structural determination of a short-lived excited iron (II) complex by picosecond x-ray absorption spectroscopy. *Phys. Rev. Lett.* **2007**, 98, 057401.

[19] R. Berera, R. van Grondelle, and J. T. M. Kennis. Ultrafast transient absorption spectroscopy: principles and application to photosynthetic systems. *Photosynth. Res.* **2009**, 101, 105-118.

[20] A. C. Cruickshank, C. J. Dotzler, S. Din, S. Heutz, M. F. Toney, and M. P. Ryan. The Crystalline Structure of Copper Phthalocyanine Films on ZnO(1-100). *J. Am. Chem. Soc.* **2012**, 134, 14302-14305.

[21] A. Matruglio, S. Nappini, D. Naumenko, E. Magnano, F. Bondino, M. Lazzarino, and S. Dal Zilio. Contamination-free suspended graphene structures by a Ti-based transfer method. *Carbon* **2016**, 103, 305-310.

[22] S. M. Sze, and Kwok K. Ng. Physics of Semiconductor Devices. John Wiley & Sons, Inc., **2007.**

3. The influence of molecular ordering in the CoPc dynamical properties

As previously discussed, one critical issue to overcome nowadays toward highly-efficient organic film-based devices is the need for thorough control of the molecular structure during film processing. Aggregation and inter-molecular interactions have a significant impact on tuning the photo-physical and dynamical carrier properties of the film[1-4], affecting the light absorption, energy level alignment, exciton diffusion and charge transport (CT) in the material[5-7]. This chapter demonstrates how different molecular arrangements affect the CT dynamics in ordered CoPc thin films. The characterization of the electronic structure and dynamical electronic properties of CoPc films with disordered, herringbone and brickstone structures is carried out by a multi-technique approach.

3.1 Structural and energy level alignment characterization of the CoPc films

The CoPc represents a particular case of great interest since the single occupied out-of-plane Co $3d_z^2$ orbital induces a strong coupling between adjacent molecular planes (Figure 3.1). As a consequence, it is proposed that it may give rise to a band of delocalized CT exciton states, allowing an efficient excitation energy transfer along the stacking axis in the CoPc film[8-10]. Previous studies show how CT states can play an essential role as intermediates in enabling a rapid evolution between the singlet (S) and triplet (T) configurations via coupling of the π-system with the 3d electron of the metal[11,12]. Materials with high intersystem crossing (ISC) quantum yield are extremely attractive since they generate long-living T states (that would not be possible to obtain by direct excitation from the ground state, spin selection rule) from short-living S states, potentially increasing the performance of several optoelectronic and photonic devices[13].

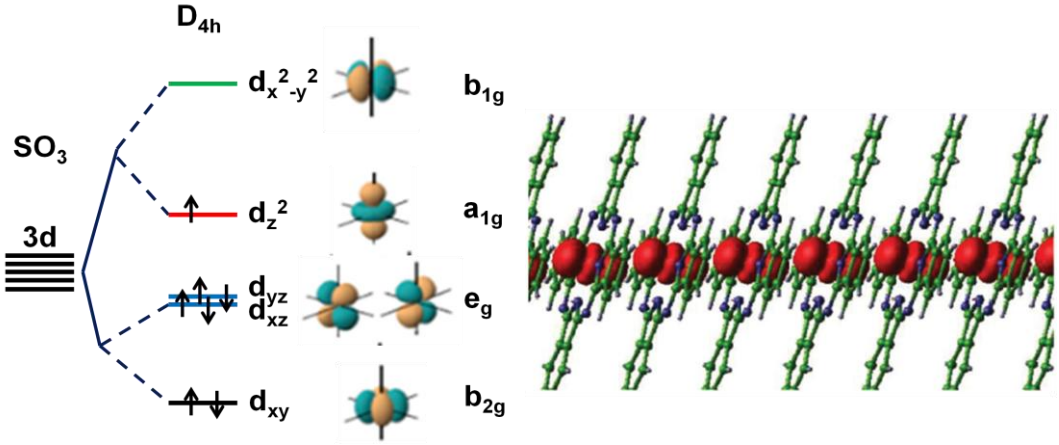

Figure 3.1 *(left) Schematic sketch of the Co 3d orbital splitting from the SO_3 spherical symmetry to the D_{4h} tetragonal distortion in the CoPc molecules, and (right) graphical representation of the α-CoPc phase stacking in solid films.*

An effective way to control the molecular orientation and obtain different film structures is to exploit the templating effect using different substrates. As demonstrated by ref. 14 it is possible to grow a specific molecular arrangement avoiding the admixture of the ordered phases. Scanning tunnel microscopy (STM) studies have shown that the first CoPc layer adopts a square or a hexagonal lattice when grown on graphene (Gr) or Au(111) respectively[15-17], leading to different molecular stacking for subsequent layers depositions. In this way, we have grown thin films with predominant herringbone or brickstone structures on Gr or Au(111) substrates, respectively. CoPc deposition on ITO leads to a disordered film[18]. A detailed description of the sample growth is provided in the section "Methods and experimental details" of Chapter 2.

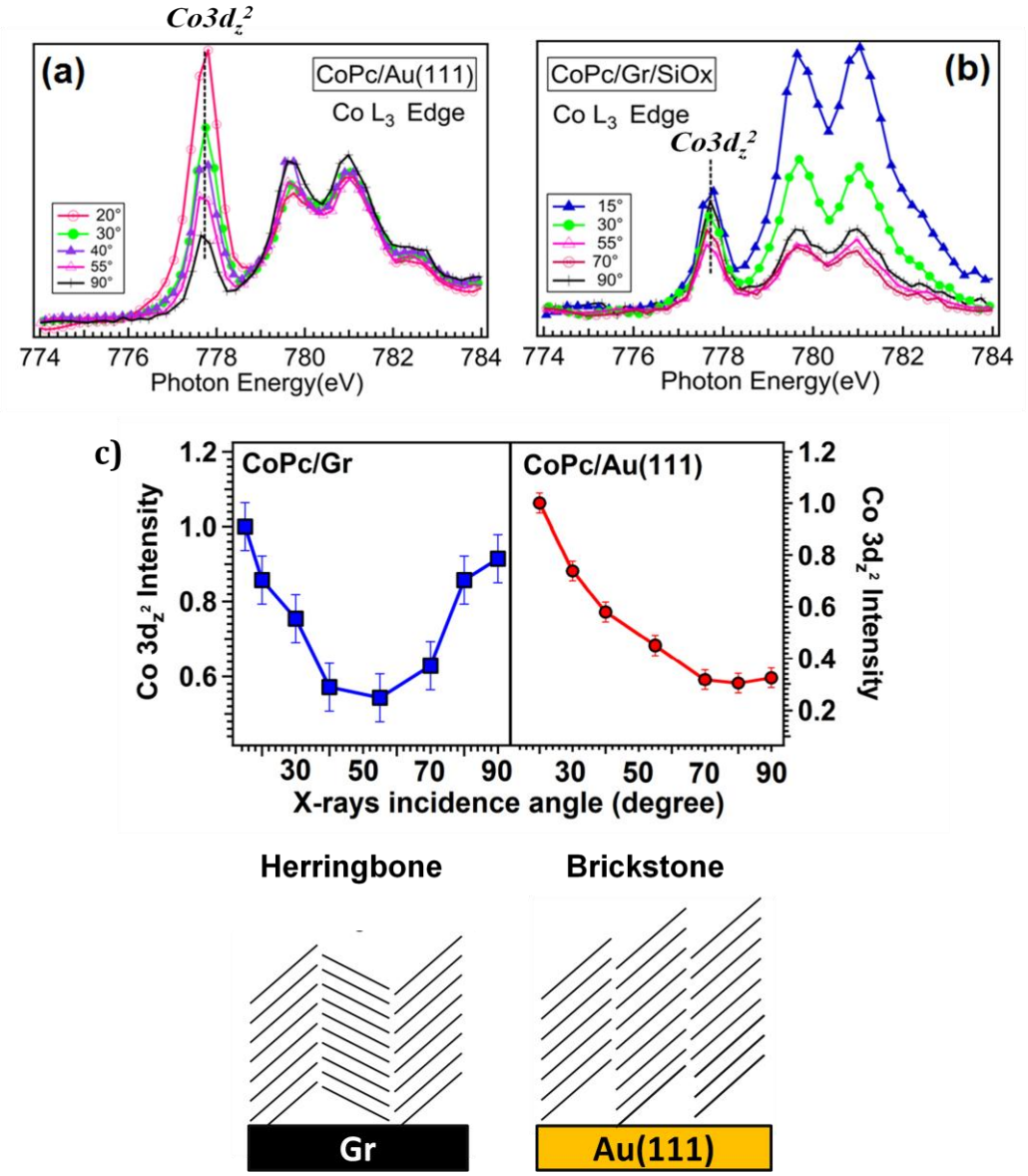

Figure 3.2 *Co L_3 edge of* **a)** *CoPc/Au(111) and* **b)** *CoPc/Gr as a function of the X-ray incidence angle (Reported from ref. 19)*; **c)** *(top) Dependence of the Co3d_z^2 peak intensity as a function of the X-ray incidence angle of the CoPc/Gr and CoPc/Au(111) samples; (bottom) schematic representation of the herringbone and brickstone structure*

Before studying the dynamical electronic properties of the films, it was necessary to have a detailed understanding of the film structures and the molecular orbitals involved in the excited state dynamics. The characterization of the molecular structure in the CoPc/Gr and CoPc/Au(111) samples has been carried out by exploiting grazing X-ray diffraction[19] and the polarization dependence of the out-of-plane Co $3d_z^2$ orbital of the CoPc. Its assignment as the first resonance peak of the Co L_3 XAS was known from literature[20]. Figure 3.2 shows the polarization dependence of the Co $3d_z^2$ peak intensity as a function of the X-ray incidence angle as measured by Co L_3 XAS. A well-defined molecular orientation is confirmed in both cases, though the two trends strongly differ. The monotonous decrease of the Co$3d_z^2$ intensity in the CoPc/Au(111) sample suggests a predominant brickstone structure, whereas the symmetric trend in the CoPc/Gr sample indicates a predominant herringbone structure[19].

The study of the electronic structure of the ordered films has been performed by combined PES-IPES measurements (Figure 3.3a). Four main peaks representing two occupied and two unoccupied states are labelled a, b, c, and d. In PES and IPES spectra several factors affect the energy level positions[21 and refs therein]. Peak broadening is due to the instrumental resolution, limited angular resolution and inelastic scattering processes. Peaks can be slightly shifted in energy because of the incomplete screening of holes/electrons induced in the system during the measurement and by polarization energy induced by molecular cations and anions originated during PES and IPES measurements. As a consequence, the energy level positions are better represented by the edges of the peaks after a proper deconvolution with the instrumental broadening[21] as shown in Figure 3.3b. In Figure 3.3a the so obtained values are reported as vertical dashed lines. From previous studies reported in the literature, the peaks a and b are assigned to the HOMO-1 and HOMO, respectively[22-24]. Concerning the unoccupied states, namely c and d, several theoretical works are reported in literature[9,23,25-27]. However, a general agreement on the correct sequence of the empty states is still missing. The calculated electronic structure of the CoPc is very sensitive to the simplified theoretical functional used to model the exchange-correlation interactions and the nature of the first empty state results of Co $3d_z^2$ (localized on the Co atom) or ligand character ($\pi\pi^*$ states delocalized over the macrocycle). Furthermore, most of them are performed in the isolated molecule approximation. Although a definitive assignment of the unoccupied states is beyond the scope of this study, we were able to draw some conclusions by combining IPES and XAS measurements from literature to our PES-IPES spectra. Xiao et al.[28] report IPES spectra of a CoPc/Au(111) thin film where the first unoccupied state, assigned to the LUMO, is located at 1.7 eV similarly to our peak d.

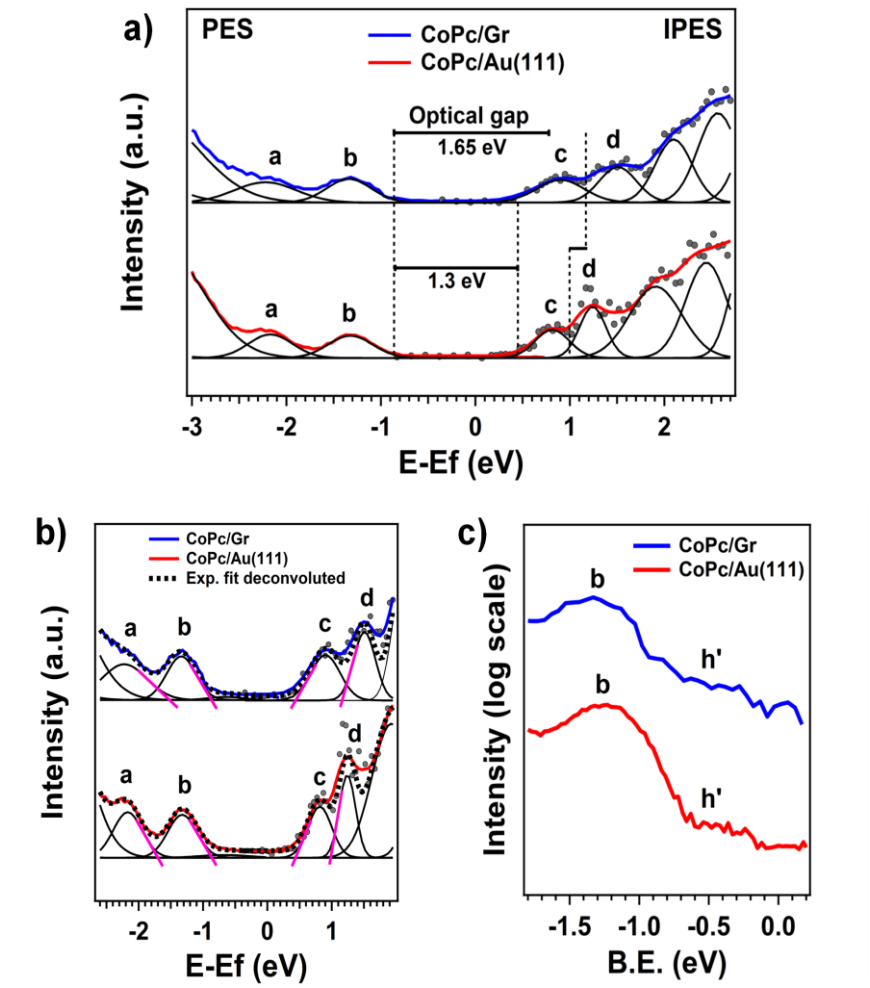

Figure 3.3 a) *Combined PES-IPES spectra of the CoPc/Gr and CoPc/Au(111) samples;* **b)** *Schematic of the procedure used for the determination of the peak edges from PES and IPES spectra. In the IPES spectral region the dots are the measured data and the continuous line (blue and red) the best fit obtained without deconvolution with the instrumental broadening. The fit components (continuous black curves) are those obtained after deconvolution and the dashed line the respective deconvoluted experimental fit;* **c)** *PES spectra of the CoPc/Gr and CoPc/Au(111) in the energy region close to* E_F *in logarithmic scale.*

However, the low-lying peak at 1.3 eV (peak c) is not observed. Such difference may be explained considering their lower experimental resolution of 0.4 eV than the present case (0.25 eV), leading to the superimposition of the two features in a broad single peak. On the other hand, Betti et al.[20] from linear polarization XAS measurements of the Co L_3 edge of a CoPc/Au(110) thin film, assign the first resonance peak to the Co $3d_z^2$ orbital and the second one to Co 3d orbitals with eg symmetry (orbitals mixed to the ligand $\pi\pi^*$ states). As shown in Figure 3.3a, the CoPc optical gap (calculated from the optical absorption spectra of ref. 8 by Tauc method[29,30]) is 1.65 eV, a value higher than the energy difference (edge to edge) between the HOMO and the first unoccupied state (1.3eV), the peak c. Representing

the CoPc optical gap, HOMO-LUMO transition, as a solid black line centred on the HOMO edge (estimated by fitting procedure, Figure 3.3b), the final state of the transition (LUMO) is located close to the edge of the unoccupied state labelled d. It can be seen that the optical gap does not precisely match the peak d. This is because the combined PES-IPES spectra measure the transport band gap, which differs from the optical band gap. The energy difference to exactly match the peak d corresponds to the exciton binding energy. Accordingly, similarly to ref. 20 we assign the first unoccupied state, c, to the single unoccupied molecular orbital (SUMO) originating from the single occupied Co $3d_{z^2}$ orbital. The presence of additional states with Co 3d character in the CoPc band gap is also supported by DFT calculations based on the β-CoPc crystal phase[27]. Aliabad et al.[27] point out the presence of two additional electronic states in the HOMO-LUMO gap at 1.13 eV and 1.39 eV with mostly Co3d character, estimating an indirect gap of 2.125 eV (without considering the middle gap states) compatible to our spectra.

An additional feature at about -0.5 eV, marked as h', can be observed as a shoulder of the peak b in Figure 3.3c. Broadening of the HOMO (peak b) induced by radiation damage in the CoPc thin films can be safely excluded. Figure 3.4 shows the CoPc/Au(111) VB spectra as a function of the irradiation time by using 38 eV photons energy. The broadening of the HOMO peak together with the smearing of the HOMO-1 induced by radiation damage start to be effective after half an hour of measurements.

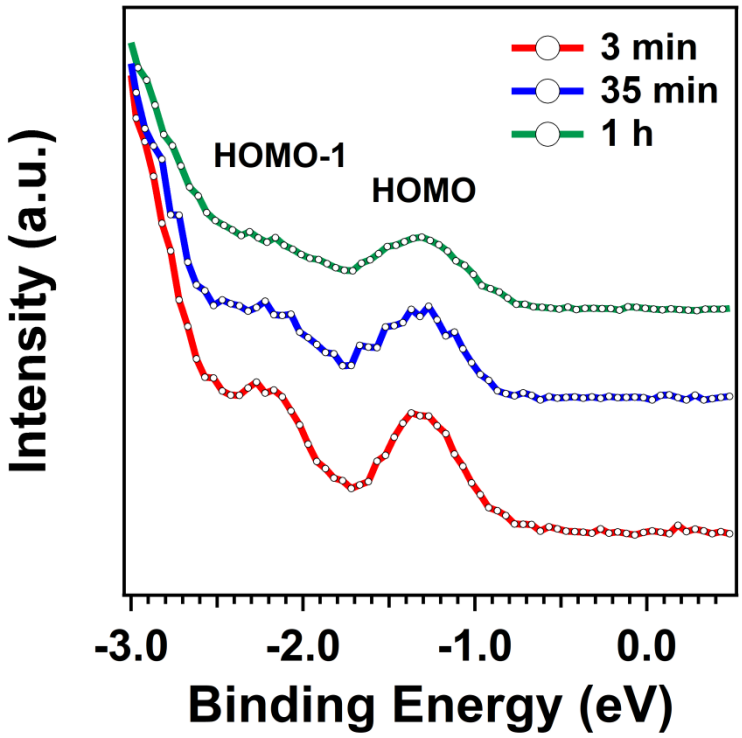

Figure 3.4 *The CoPc/Au(111) VB spectra as a function of the irradiation time by using 38 eV photon energy.*

Since the photon energy is smaller than the Co 3p ionization energy (~55 eV), the observed changes in the peaks should not be originated from the partial dissociation of the

CoPc molecule, but more likely from a higher molecular disorder induced by the photon flux. The spectrum just after the irradiation (3 min) is the one reported in the combined PES-IPES spectra in Figure 3.3a. Concerning the origin of this feature, previous STM measurements[17] and VB spectra of CoPc thin films[22,24,31] point out the presence of a low-lying state to the HOMO and assigned it to the Co $3d_z^2$ orbital. Accordingly, we assign h' to the single occupied molecular orbital (SOMO) originating from the Co $3d_z^2$ orbital. However, in the CoPc/Gr case h' is broader and barely observable; it is worth noting that all its peaks are broader than in the CoPc/Au(111) sample, suggesting a higher molecular disorder.

3.2 CoPc thin films excited state dynamics

Before discussing the excited state dynamics in the CoPc films, for the sake of clarity the CoPc optical properties will first be briefly reported. Figure 3.5 shows the UV/Vis absorption spectrum of a CoPc film on quartz from ref. 8. The UV/Vis absorption of CoPc shows three bands, the Q band, the B-band (Soret band) and the N-band, all involving ππ* excitation of the macrocycle[33-35]. The Q-band is split into two peaks since in the solid state the exciton coupling lifts the double degeneracy of the LUMO (ππ* states). The two peaks are located at about 1.8 eV and 2 eV, A and B respectively[10,36]. However, the presence of a transition metal with half-filled d shell origins additional excited states, πd* or CT states on the high-energy side of the Q-band[37]. Inter-molecular CT states are often coupled with intra-molecular exciton states gaining an appreciable intensity in the optical absorption spectra from excitation of the ππ* states[12 and refs therein,38]. This fact may be a first suggestion that the 3d orbitals of the transition metal are directly involved in the degree of mixing between CT and intra-molecular excitons.

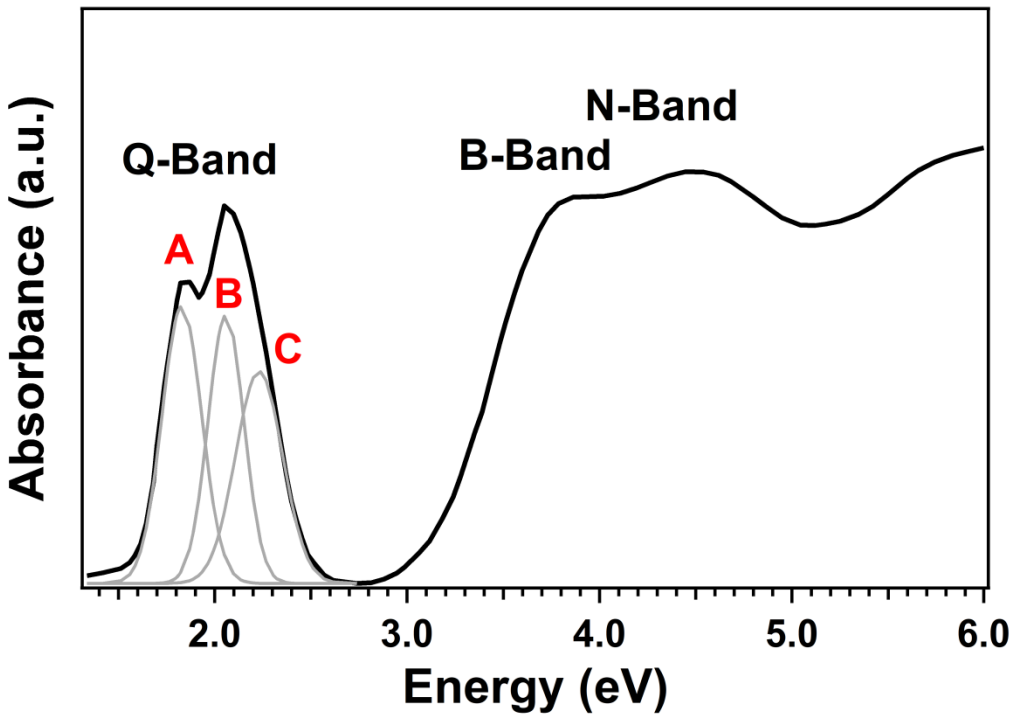

Figure 3.5 *CoPc/quartz thick film optical absorption spectrum from ref. 8.*

The excited state dynamics of the CoPc were studied by transient absorption spectroscopy (TAS) in two different time domains (15 ps and 7 ns) and time-resolved photoemission spectroscopy (TR-PES). To have comparable results with the literature[8] and point out the CoPc relaxation dynamics independently of the influence of molecular ordering, the disordered CoPc/ITO film was first studied as a reference. Figure 3.6a shows the TAS spectra in transmittance mode obtained by using three different pump pulse energies, 3.1 eV (Soret band excitation), 2.41 eV (Q-band excitation) and 1.21 eV (excitation into the CoPc band gap) at two different time delays, 0.25 ps and 15 ps. Independently of the pump energy, all the spectra in the Q-band region show two transient bands with negative signals (I and III) and one with a positive signal (II). Negative signals in TAS spectra correspond to absorption bleaching (see section 2.4.3. of Chapter 2). In this case, the band I and III represent the ground state bleaching due to the depletion of the ground state by the excitation pulse which promotes electrons from the HOMO to the LUMO (A and B components of the optical spectra, respectively). As a consequence, the excited configuration of the CoPc absorbs less in that spectral range than the ground state. The positive signal II is called induced absorption (see section 2.4.3. of Chapter 2), i.e. excited states give rise to an additional absorption not possible from the ground state (for fixed photon energy). In other words, the bands I and III represent the excitation from the singlet ground state (S_0) to the first singlet excited states (S_1). The band II corresponds to the transition from the first triplet excited state (T_1) to the second triplet excited state (T_2).

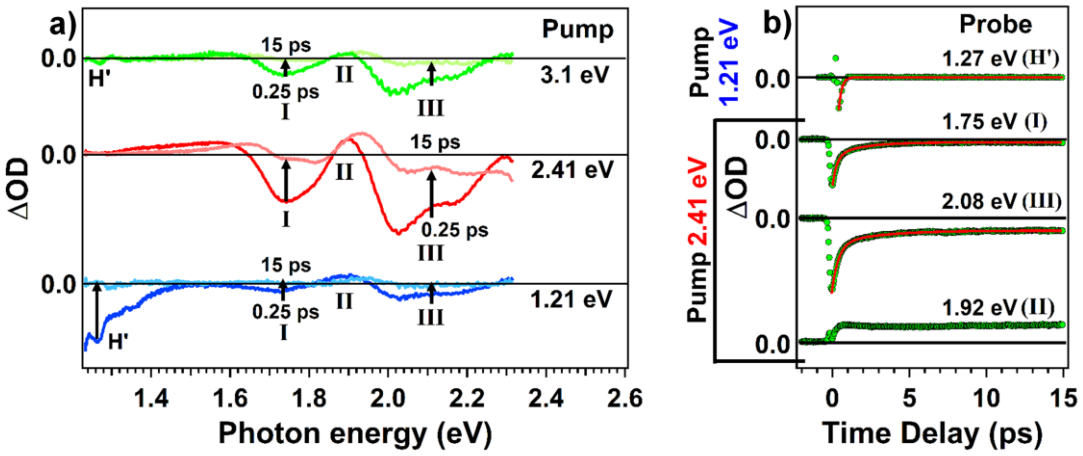

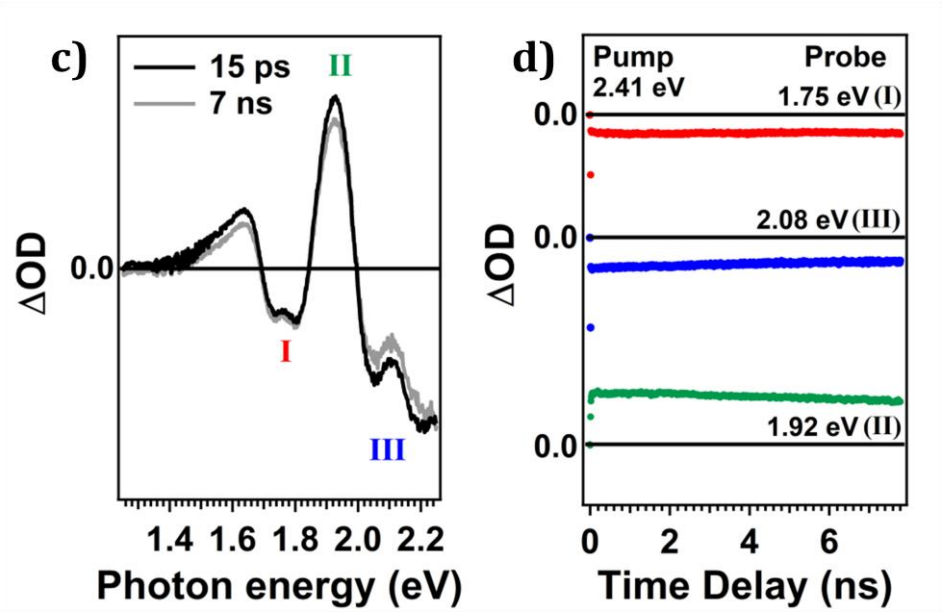

Figure 3.6 a) *TAS spectra in transmittance mode of the CoPc/ITO sample using three different pump pulse energies;* ***b)*** *Decay curves of the transient bands I, II and III using a pump pulse of 2.41 eV and of H' using a pump pulse of 1.21 eV;* ***c)*** *TAS spectra using a 2.41 eV pump pulse at time delays of 15 ps and 7 ns;* ***d)*** *Decay curves of the transient band I, II and III using a 2.41 eV pump pulse.*

Decay time	Probe photon energy			
	1.27 eV (H')	1.75 eV (I)	2.08 eV (III)	1.92 eV (II)
τ_1	208 fs	285 fs	422 fs	ns
τ_2	-	1.78 ps	2.92 ps	-

Table 3.1 *Decay times as a function of the probe photon energy of the CoPc/ITO sample estimated by using eq. 2.5 (see section 2.4.3 of Chapter 2).*

These assignments are further confirmed by the relative decay curves of each transient band (figure 3.6b). The bleaching signals I and III show decays occurring in two distinct timescales: an initial ultrafast relaxation which involves two dynamical processes (with decay times of hundreds of fs, τ_1, and of few ps, τ_2 - Table 3.1), and a longer decay of the residual signal evolving over the ns time domain (Figure 3.6c and d). The induced absorption signal II evolves over the ns time scale, as characteristic of triplet state dynamics**.** All three pumps show the same kinds of decay times. Since the 3.1 eV pump pulse excites the system into the Soret-band, (S_2), Kasha's rule predicts ultrafast inter-band (S_2 vibrational cooling) and intra-band relaxations ($S_2 \rightarrow S_1$) should be the first dynamical processes to occur (Figure 3.7). However, no differences are observed in TAS spectral feature and relaxation dynamics by exciting the system to S_1 (pump 2.41 eV) or S_2 (pump 3.1 eV). This fact allows us to point out that:

1) Intra-band relaxation of S_2 (vibrational cooling) and inter-band process ($S_2 \rightarrow S_1$) are faster than our experimental time resolution and not responsible for the initial ultrafast relaxation of the bands I and III (τ_1)

2) T_1 is populated through intersystem crossing (ISC) by S_1 rather than S_2. The process is faster than 0.25 ps (the band II has completely developed within 0.25 ps) and not assignable to τ_1 (Figure 3.7).

As we will demonstrate in the following of this section, τ_1 corresponds to the relaxation of S_1 to the ground state by the internal conversion (IC) process. The ultrafast ISC in the CoPc is rationalized supposing that the coupling between the transition metal 3d orbitals and the phthalocyanine-based exciton states provides additional channels for the relaxation of the excited states, leading to high ISC quantum yield[11,39-41]. The involvement of CT states, originated from the 3d half-filled shell, acting as intermediate in the evolution between $^1\pi\pi^*$ and $^3\pi\pi^*$ configurations may obviate the need for an unfavourable spin-orbit coupling (^2S ($^1\pi\pi^*$)$\rightarrow ^2CT \rightarrow ^2T$ ($^3\pi\pi^*$))[11]. In summary, the CoPc exciton dynamics in the Q-band energy region can be rationalized as shown in Figure 3.7.

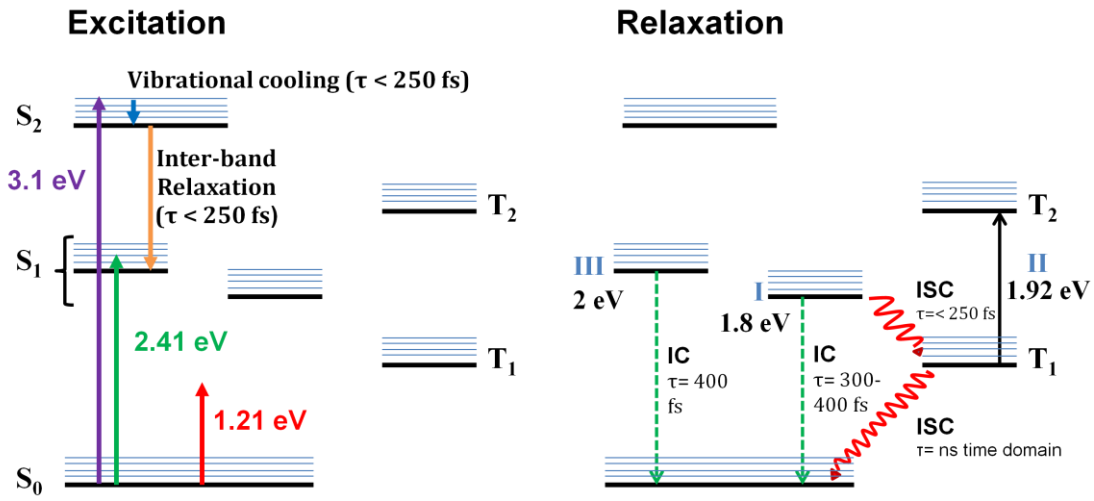

Figure 3.7 *Jablonski diagram of the relaxation excitation and relaxation processes in the system, discussed in the text. I, II, III refers to the transient bands observed in TAS spectra.*

After excitation by the pump pulse, the first singlet excited states, S_1, (transient bands I and III) have two possible de-excitations pathways over the first ps: directly relax to the ground state by IC ($S_1 \rightarrow S_0$) or populate T_1 through ISC ($S_1 \rightarrow T_1$). In any case, the complete relaxation of S_1 is not achieved over the first 15 ps and a long-lasting bleaching signal persists over the ns time domain. The induced absorption signal at 1.92 eV ($T_1 \rightarrow T_2$), similarly to the residual signal of S_1 states, is almost constant over a time scale of about 7 ns (Figure 3.6c and d). This fact suggests that no further relaxation of S_1 states occurs as long as the population of T_1 states decays to the ground state. Since no fluorescence is reported in the CoPc[42,43], it can be concluded that the coordination of the Co into the macrocycle drastically enhances the ISC yield and

the de-excitation through the triplet states becomes one of the main relaxation channels in the CoPc thin film.

In Figure 3.6a it is possible to note another feature at about 1.3 eV, marked H'. By using a 1.21 eV pump pulse (excitation energy below the CoPc optical gap) it becomes the predominant transient band in the spectra. It will be shown that the dynamic process associated with H' may specifically involve the Co $3d_z^2$ orbital. We recall that the single occupied Co $3d_z^2$ orbital gives rise to a SUMO with HOMO-SUMO energy separation of about 1.3 eV (Figure 3.3a). The lack of H' by using a 2.41 eV pump pulse may be due to its superimposition to the broad positive induced absorption signal ranging from 1.3 eV to 1.6 V (whose intensity is highly enhanced at this excitation energy).

The TAS spectra using a 2.41 eV pump pulse of the ordered CoPc/Gr and CoPc/Au(111) films are shown in Figure 3.8a.

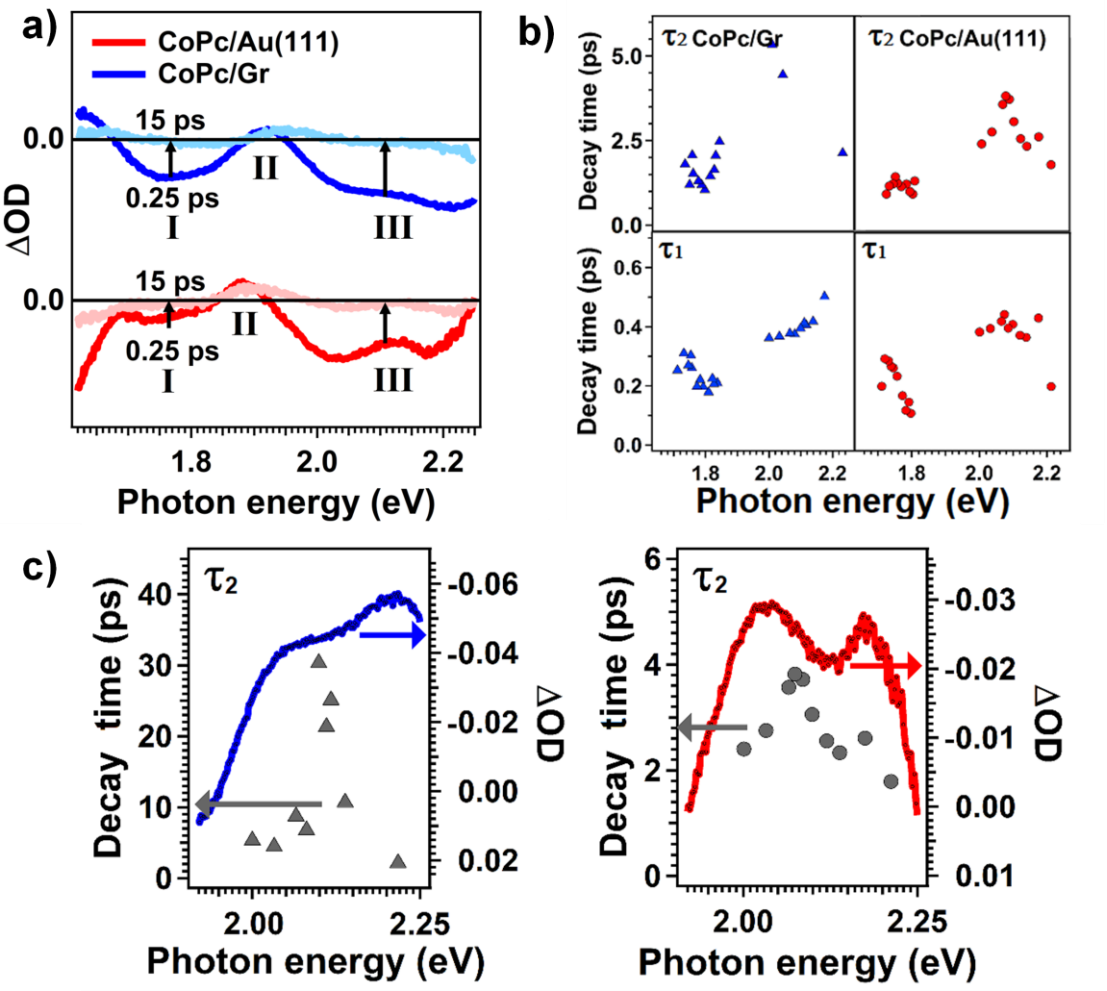

Figure 3.8 a) *CoPc/Gr and CoPc/Au(111) TAS spectra in the Q-Band energy region;* **b)** *Estimated decay times, τ_1 and τ_2, as a function of the probe photon energy in the Q-band energy region.* **c)** *Decay time τ_2, attributed to CT exciton dynamics, as function of the probe photon energy and the bleaching signal III from TAS spectra is shown for comparison.*

In this case, the measurements were performed in reflectance mode (opaque substrate) and the spectra can result mirrored with respect to the transmittance mode[44]. However, the physical meaning of the transient bands in the two cases is qualitatively the same. For this reason, the spectra in Figure 3.8a have been multiplied by -1 to facilitate the graphical comparison with the CoPc/ITO sample previously discussed. Both samples have TAS spectra qualitatively identical to those of the CoPc/ITO thin film in the Q-band region; the bleaching signals I and III show an ultrafast double exponential relaxation dynamics with decay times τ_1 and τ_2 over the whole Q-band (Figure 3.8b), and the induced absorption II decays in the ns time domain (the origin of the bands I, II, and III has been previously discussed). The decay time τ_1 is independent of the film structure: the ordered and disordered systems have values nearly identical. This fact suggests that τ_1 is due to an intra-molecular relaxation process. The decay time τ_2, as shown in Figure 3.8c, in both samples shows a maximum value at about 2.1 eV of photon energy. However, it has a clear dependence on the CoPc thin film structure, going from 4 ps in the brickstone structure to tens of ps in the herringbone structure. Gadalla et al.[8] from TAS measurements on a CoPc/quartz system report, as in our case, a relaxation dynamics centred at 2.04 eV of photon energy, tentatively attributed to the presence of a delocalized CT exciton band. Inducing a strong coupling between adjacent molecules, the perpendicularly oriented Co $3d_z^2$ may originate a band of delocalized CT exciton states allowing an efficient excitation energy transfer along the molecular stacking axis (additional relaxation channel). Considering that CT states are located in the high-energy side of the Q-band[37] (2.2 eV) and the relaxation dynamic at 2.1 eV is dependent on the molecular structure, we assign τ_2 to the CT exciton dynamics. Accordingly, the observation of a decay time τ_2 in both transient bands I and III (Figure 3.8b) can be rationalized by taking into account hybridization effects between CT and S_1 states. The degree of mixing between states is strongly related to their energy separation[38]. Due to the small energy difference between the S_1 states of the LUMO (0.2 eV), a partial CT character is expected over the whole Q-band energy region, even though with a lower degree of mixing at the low-energy side (the transient band I). Due to the rapid ISC, faster than our experimental time resolution, here it is not possible to discern if CT states effectively play an active role as intermediate in enabling the evolution from S to T configurations. Nevertheless, the comparison with TAS spectra in the literature of α-CuPc films highlights the possibility of a significant contribution of the out-of-plane Co $3d_z^2$ orbital to the CT dynamics of the CoPc. We recall that in the case of the CuPc, the single occupied metal orbital is the $3d_{x^2-y^2}$ (in-plane oriented). The TAS spectra of both systems show the bleaching signals I and III[8,39]. However, in the CuPc case only the band I show an initial ultrafast relaxation similarly to the CoPc, whereas the band III decays in hundreds of ps[39]. In CuPc films has been pointed out that, after an initial excitation along the molecular plane, the transition dipole polarization of the intermixed S_1-CT excitations turns by 65° aligning along the molecular stacking axis. Such reorientation is interpreted as the dynamics and the direction of the charge separation process[12]. We believe that in the CoPc case the perpendicular orientation of the Co $3d_z^2$ orbital along the molecular stacking axis

direction may highly enhance the efficiency of the CT and charge separation dynamics, giving rise to an additional channel for a faster relaxation of the band III. In any case, future femtosecond TAS measurements could be useful to clarify those points.

Finally, as in the CoPc/ITO case, both samples also show the band H' (Figure 3.9a), even though its relaxation dynamic differs. It has a decay time of sub-ps in the CoPc/Au(111) and of ns CoPc/Gr sample (Figure 3.9b). In the CoPc/Au(111) film is observed an additional negative peak at 1.6 eV. The transient spectra of the Au(111) substrate show the same intense negative band at 1.6 eV. We recall that TAS measurements in reflectance mode are also sensitive to the dynamical processes of the substrate. Similarly, the CoPc/Gr sample shows a broad negative band ranging from 1.25 eV to 1.5 eV not observed neither in the CoPc/Au(111) nor in the CoPc/ITO samples. The comparison between the decay curve of H' of the CoPc/Gr sample and the decay curve of the dynamics observed in the Gr substrate at the same photon energy of H' (1.27 eV) is shown in Figure 3.9c. The relaxation dynamics are identical. Therefore, in the CoPc/Gr case the origin of H' is due to the long-living dynamics of the Gr substrates and not to the molecular film.

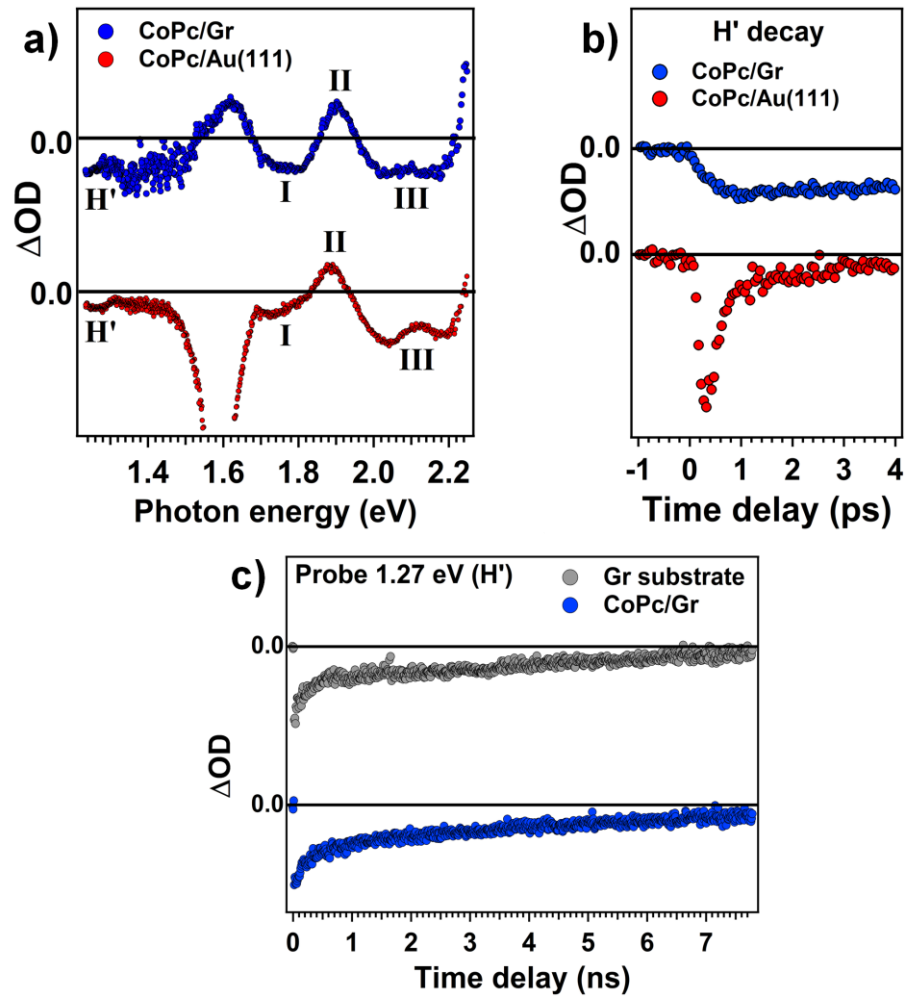

Figure 3.9 a) *TAS spectra of the CoPc/Gr and CoPc/Au(111) samples using a 2.41 eV pump pulse;* **b)** *Comparison between the decay curves of the transient*

band H' of the CoPc/Gr and CoPc/Au(111) samples; **c)** *Comparison between the decay curves at 1.27 eV of the photon energy of the CoPc/Gr sample and Gr substrate.*

To clarify the nature of the decay time τ_1 and of the band H' (in the CoPc/ITO and CoPc/Au(111) samples) we exploited the sensitivity to the states of TR-PES. The CoPc/Au(111) TR-PES spectra using a 2 eV pump pulse are shown in Figure 3.10a. The CoPc/Gr spectra are not reported since, as mentioned in discussing Figure 3.3c, due likely to the higher molecular disorder, the SOMO was barely observable without providing any additional information. After the pump pulse excitation two effects are observable, the HOMO bleaching, due to the promotion of electrons into the LUMO, and a shift in energy toward E_F of the SOMO. In the former case, we found a decay time of 298 fs (Figure 3.10b), that matches τ_1 in the TAS spectra. Considering the lack of fluorescence of the CoPc[42,43] and that the de-excitation of triplet states occurs in the ns time domain, we assign τ_1 to the non-radiative relaxation of the singlet excited states to the ground state by IC ($S_1 \rightarrow S_0$). Noteworthy, the SOMO shift shows a decay time of 148 fs. Comparable values are observed in the decay curves of H' in the CoPc/ITO and CoPc/Au(111) TAS spectra. The comparison is shown in Figure 3.10c. The comparison between TAS and TR-PES decay curves is meaningful even in the case of opposite signs. The TAS spectra signal is dependent on the mode used (transmittance or reflectance) and the chosen unit measure (ΔOD, ΔT or ΔR). We recall that using a 1.21 eV pump pulse H' becomes the predominant band in the TAS spectra (Figure3.6a). Furthermore, combined PES-IPES spectra show a HOMO-SUMO energy separation of 1.3 eV which corresponds to the photon energy of H' (1.27 eV). However, safely addressing the origin of such dynamics is far away to be trivial. The low intensity of the SOMO makes it difficult to detect a possible SOMO-LUMO transition promoted by the excitation pulse. The CoPc optical absorption spectra in the literature do not report any direct evidence of possible intra-gap absorption at 1.3 eV due to SOMO-LUMO or HOMO-SUMO excitations. Furthermore, it is not possible to safely exclude the involvement of trap-states due to film defects or other types of intra-gap states. Nevertheless, we hypothesize that a partial redistribution of the charge density between the different atomic sites of the molecule may lead to a shift in the energy of the SOMO peak. We recall that the HOMO has mostly atomic orbital contribution from the C and N atoms of the Pc macrocycle, whereas the SOMO and SUMO are localized on the Co atom[23,24]. The promotion of electrons from the HOMO to the SUMO by the pump excitation would imply the complete occupancy of the single occupied orbital and the charge redistribution toward the Co atomic site, possibly justifying the energy shift toward E_F. Calculations show that, due to the repulsion between electrons, the complete occupancy of the Co $3d_z^2$ orbital should cause an energy increase of the corresponding state by 0.2 eV[26].

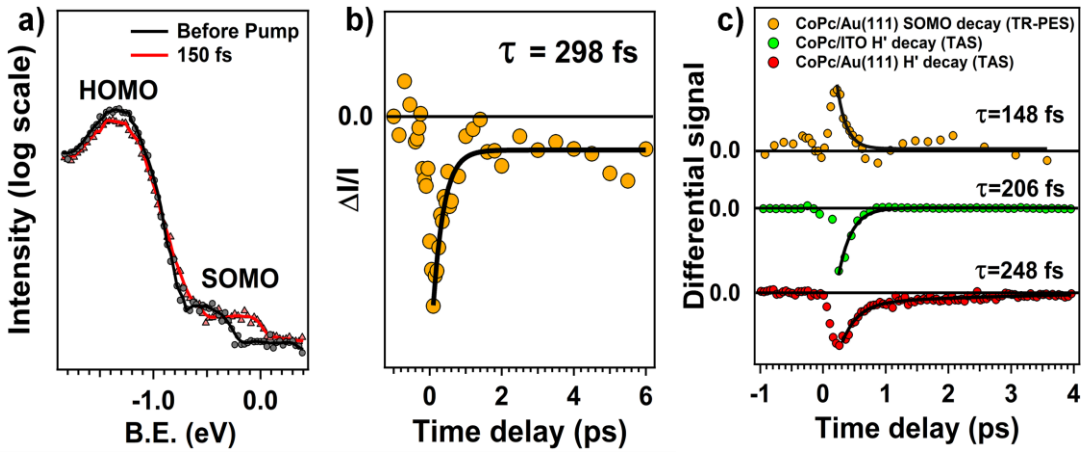

Figure 3.10 a) *CoPc/Au(111) sample TR-PES spectra before and after the pump pulse;* **b)** *decay curve of the HOMO repopulation (ΔI is defined as the difference between the PES intensity with and without the excitation pulse);* **c)** *comparison between the decay curves of the SOMO shift in the TR-PES spectra (top) and of the transient band H' of the CoPc/ITO (middle) and CoPc/Au(111) (bottom) samples in the TAS spectra.*

References:

[1] C. Qian, J. Sun, and Y. Gao. Transport of charge carriers and optoelectronic applications of highly ordered metal phthalocyanine heterojunction thin films**.** *Phys. Chem. Chem. Phys.* **2021**, 23, 9631.

[2] H. Lim, S. Yang, S.-H. Lee, J.-Y. Lee, Y. Lee, A. B. Situmorang, Y.-H. Kim, and J. W. Kim. Influence of the metal phthalocyanine molecular orientation on charge separation at the organic donor/acceptor interface. *J. Mater. Chem. C*, **2021**, 9, 2156.

[3] T. Wang, T. R. Kafle, B. Kattel, and W.-L. Chan. Observation of an Ultrafast Exciton Hopping Channel in Organic Semiconducting Crystals. *J. Phys. Chem. C* **2016**, 120, 14, 7491–7499

[4] M. Lia, W.-H. Lia, Y.-J. Hua, J. Lengb, W.-M. Tianb, C.-Y. Zhaob, J.-X. Liub, R.-R. Cuib, S.-Y. Jinb, C.-H. Chenga, and S.-L. Conga, Chin. *J. Chem. Phys.* **2021**.

[5] C. Videlot, A. El Kassmi, and D. Fichou, Photovoltaic properties of octithiophene-based Schottky and p/n junction Cells: Influence of molecular orientation *Sol. Energy Mater. Sol. Cells*, **2000**, 63, 69-82.

[6] V. Coropceanu, J. Cornil, D. A. da Silva Filho, Y. Olivier, R. Silbey, and J.-L. Bredas. Charge transport in organic semiconductors**.** *Chem. Rev.*, **2007**, 107, 926-952.

[7] S. Duhm, G. Heimel, I. Salzmann, H. Glowatzki, R. L. Johnson, A. Vollmer, J. P. Rabe, and N. Koch. Orientation-dependent ionization energies and interface dipoles in ordered molecular assemblies. *Nat. Mater.* **2008**, 7, 326.

[8] A. Gadalla, J. B. Beaufrand, M, Bowen, S. Boukari, E. Beaurepaire, O. Crégut, M. Gallart, B. Honerlage, and P. Gilliot. Ultrafast Optical Dynamics of Metal-Free and Cobalt Phthalocyanine Thin Films II: Study of Excited-State Dynamics. *J. Phys. Chem. C*, **2010**, 114, 17854–17863.

[9] W. Wu, N.M. Harrison, and A. J. Fisher. Electronic structure and exchange interactions in cobalt phthalocyanine chains. *PRB,* **2013**, 88, 024426.

[10] H. Yoshida, Y. Tokura, and T. Koda. Charge-transfer excitation bands in electro-absorption spectra of metal (Co, Ni, Cu, Zn)-phthalocyanine films. *Chemical Physics*, **1986**, 109, 375-382.

[11] M.-H. Ha-Thi, N. Shafizadeh, L. Poisson, and B. Soep. An Efficient Indirect Mechanism for the Ultrafast Intersystem Crossing in Copper Porphyrins. *J. Phys. Chem. A* **2013**, 117, 8111−8118.

[12] A. Popescu, R. A. Younts, B. Hoffman, T. McAfee, D. B. Dougherty, H. W. Ade, K. Gundogdu, and I. V. Bondarev. Monitoring Charge Separation Processes in Quasi-One-Dimensional Organic Crystalline Structures. *Nano Lett.* **2017**, 17, 6056−6061.

[13] M. C. Hanna, and A. J. Nozik. Solar Conversion Efficiency of Photovoltaic and Photoelectrolysis Cells with Carrier Multiplication Absorbers. *J. Appl. Phys.* **2006**, 100, 7, 074510.

[14] A. C. Cruickshank, C. J. Dotzler, S. Din, S. Heutz, M. F. Toney, and M. P. Ryan. The Crystalline Structure of Copper Phthalocyanine Films on ZnO(1-100). *J. Am. Chem. Soc.* **2012**, 134, 14302−14305.

[15] P. Järvinen, S. K. Hämäläinen, K. Banerjee, P. Häkkinen, M. Ijäs, A. Harju, and P. Liljeroth. Molecular Self-Assembly on Graphene on SiO_2 and h-BN Substrates. *Nano Lett.* **2013**, 13, 3199−3204.

[16] R. A. Rehman, H. J. Zhang, A. Razaq, S. M. Ramay, M. Hasan, M. A. Javed, and S. Atiq. Spectro-microscopy characterization of CoPc-Au(111) interface. *Physica E: Low-dimensional Systems and Nanostructures* **2021**, 125, 114357.

[17] D. E. Barlow, L. Scuderio, and K. W. Hipps. Scanning Tunneling Microscopy Study of the Structure and Orbital-Mediated Tunneling Spectra of Cobalt(II) Phthalocyanine and Cobalt(II) Tetraphenylporphyrin on Au(111): Mixed Composition Films. *Langmuir* **2004**, 20, 4413.

[18] A. Kumar, D. Naumenko, L. Cozzarini, L. Barba, A. Cassetta, and M. Pedio. Influence of substrate on molecular order for self-assembled adlayers of CoPc and FePc. *J Raman Spectrosc.* **2018**, 49, 1015-1022.

[19] A. Kumar thesis: *Influence of substrate on physical properties of transition metal complexes thin films*. Università degli Studi di Trieste, Trieste, **2018**.

[20] M. G. Betti, P. Gargiani, R. Frisenda, R. Biagi, A. Cossaro, A. Verdini, L. Floreano, and C. Mariani. Localized and Dispersive Electronic States at Ordered FePc and CoPc Chains on Au(110). *J. Phys. Chem. C*, **2010,** 114, 21638–21644.

[21] D. R. T. Zahn, G. N. Gavrila, and G. Salvan. Electronic and Vibrational Spectroscopies Applied to Organic/Inorganic Interfaces. *Chem. Rev*. **2007,** 107, 1161-1232.

[22] P. Gargiani, M. Angelucci, C. Mariani, and M. G. Betti. Metal-phthalocyanine chains on the Au(110) surface: Interaction states versus *d*-metal states occupancy. *PRB* **2010**, 81, 085412.

[23] E. Salomon, P. Amsalem, N. Marom, M. Vondracek, L. Kronik, N. Koch, and T. Angot. Electronic structure of CoPc adsorbed on Ag(100): Evidence for molecule-substrate interaction mediated by Co 3d orbitals. *PRB* **2013**, 87, 075407.

[24] V. V. Maslyuk, V. Y. Aristov, O. V. Molodtsova, D. V. Vyalikh, V.M. Zhilin, Y.A. Ossipyan, T. Bredow, I. Mertig, and M. Knupfer. The electronic structure of cobalt phthalocyanine. *Applied Physics A* **2009**, 94, 485-489.

[25] I. E. Brumboiu, G. Prokopiou, L. Kronik, and B. Brena. Valence electronic structure of cobalt phthalocyanine from an optimally tuned range-separated hybrid functional. *J. Chem. Phys.* **2017**, **147**, 044301.

[26] M.-S. Liao, and S. Scheiner. Electronic structure and bonding in metal phthalocyanines, Metal Fe, Co, Ni, Cu, Zn, Mg. *J. Chem. Phys.* **2001**, 114, 8.

[27] H. A. R. Aliabad, and M. Bashi. Cobalt phthalocyanine polymer for optoelectronic and thermoelectric applications. *Journal of Materials Science: Materials in Electronics* **2019**, 30, 18720–18728.

[28] J. Xiao, and P. A. Dowben. The role of the interface in the electronic structure of adsorbed metal(II) (Co, Ni, Cu) phthalocyanines. *J. Mater. Chem.* **2009**, 19, 2172–2178.

[29] J. Tauc, R. Grigorovici, and A. Vancu. Optical Properties and Electronic Structure of Amorphous Germanium. *Phys. Status Solidi B* **1966**, 15, 627−637.

[30] N. F. Mott, and E. A. Davis. *Electronic Processes in Non-Crystalline Materials*, OUP Oxford, **2012**.

[31] M. Grobosch, V. Y. Aristov, O. V. Molodtsova, C. Schmidt, B. P. Doyle, S. Nannarone, and M. Knupfer. Engineering of the Energy Level Alignment at Organic Semiconductor Interfaces by Intramolecular Degrees of Freedom: Transition Metal Phthalocyanines. *J. Phys. Chem. C* **2009**, 113, 13219–13222.

[32] J. J. Yeh, and I. Lindau. *At. Data Nucl. Data* **1985**, Tables 32, 1.

[33] A. Davidson. The effect of the metal atom on the absorption spectra of phthalocyanine films. *J. Chem. Phys.* **1982**, **77**, 168.

[34] H. Höchst, A. Goldmann, S. Hüfner, and H. Malter. X-Ray Photoelectron Valence Band Studies on Phthalocyanine Compounds. *Phys. Status Solidi B* **1976**, 76, 559.

[35] M. M. El-Nahass, Z. El-Gohary, and H.S. Soliman. Structural and optical studies of thermally evaporated CoPc thin films. *Opt. Laser Technol.* **2003**, 35, 523.

[36] M. Knupfer, T. Schwieger, H. Peisert, and J. Fink. Mixing of Frenkel and charge transfer excitons in quasi-one-dimensional copper phthalocyanine molecular crystals. *PRB* **2004**, 69, 165210.

[37] D. Potamianos, M. Nuber, A. Schletter, M. Schnitzenbaumer, M. Haimerl, P. Scigalla, M. Wörle, L. I. Wagner, R. Kienberger, and H. Iglev. Full Dynamics Description of Mg Phthalocyanine Crystalline and Amorphous Semiconductor Systems. *J. Phys. Chem. C* **2021**, 125, 18279−18286.

[38] J. P. Hernandez, and S. I. Choi. Optical Absorption by Charge-Transfer Excitons in Linear Molecular Crystals. *J. Chem. Phys.* **1969**, 50, 1524.

[39] B. W. Caplins, T. K. Mullenbach, R. J. Holmes, and D. A. Blank. Femtosecond to nanosecond excited state dynamics of vapor deposited copper phthalocyanine thin films**.** *Phys. Chem. Chem. Phys.* **2016**, 18, 11454.

[40] Y. Yan, S. Lu, R. Zhu, J. Zhou, S. Wei, and S. Qian. Ultrafast Excited State Dynamics of Modified Phthalocyanines: p-HPcZn and p-HPcCo. *J. Phys. Chem. A* **2006**, 110, 10757.

[41] A. Antipas, and M. Gouterman. Electronic States of Co, Ni, Rh, and Pd Complexes. *J. Am. Chem. Soc.* **1983**, 105, 4896.

[42] H. Isago. *Optical Spectra of Phthalocyanines and Related Compounds*. Springer: Tokyo, **2015**.

[43] P. S. Vincett, E. M. Voigt, and K. E. Rieckhoff. Phosphorescence and Fluorescence of Phthalocyanines. *J. Chem. Phys.* **1971**, 55, 8.

[44] C. Gao, X. Zhao, J. Yao, X.-Q. Yan, X.-T. Kong, Y. Chen, Z.-B. Liu, and J.-G. Tian. Sign of differential reflection and transmission in pump-probe spectroscopy of graphene on dielectric substrate. *Photonics Research* **2015**, 3, 2, A1-A9.

4. The SPV effect in semiconductor systems

The characterization of the surface photovoltage (SPV) effect in technologically important inorganic semiconductors and organic-inorganic heterojunctions is discussed in this chapter. I developed the code LEINEC (Light/Electron Induced Non Equilibrium phenomena Calculator) to model the static and transient SPV effect in semiconductor systems. The code uses two models based on the thermoionic field emission theory to simulate the experimental results[1-3]. The validity of the code in predicting the static and transient SPV has been tested in inverse photoemission and photoemission data sets from the literature[4,5,6] (SiO_2/Si, GaP and GaAs systems). In the second step, TR-PES measurements were performed on n- and p- doped SiO_2/Si(100) systems to study the dependence of the SPV relaxation dynamics on the doping and photon flux. The LEINEC code has been able to evaluate their SPV magnitude and relaxation dynamics correctly. Finally, the copper phthalocyanine (CuPc)/SiO_2/p-Si(100) heterojunction was studied by TR-PES. Transient SPV effect is observed in the molecular thin film with identical magnitude and relaxation dynamics of the Si/SiO_2 substrate, suggesting a relationship between the SPV relaxation dynamics in the two materials.

4.1 The SPV effect

As briefly mentioned in section 1.2 of Chapter 1, close to the interface or surface of inorganic semiconductor systems a perturbation of local charge balance may be present and the energy bands are bent. The band bending at the interface or surface of semiconductors may arise in two cases: when a semiconductor is in contact with a metal or a second semiconductor (Figure 4.1a), or when surface states are present at the surface of a clean semiconductor (Figure 4.1b). The perturbation of the energy levels at the interface is due to the equilibration between the Fermi levels (E_F) of the semiconductor and the metal (or the second semiconductor) when are in contact[7-10]. Similarly, the equilibration of the bulk E_F ($E_{F(bulk)}$) with the surface E_F of the surface states ($E_{F(surf.)}$) induces band bending at the surface of a clean semiconductor. For sake of clarity to the terminology used in the chapter, a short overview of the band bending is given in the following. The case of the semiconductor in contact with metal is first discussed. When a semiconductor and a metal are in contact, the E_F of the two materials must coincide at thermal equilibrium. If the work function of the semiconductor is lower than that of the metal (Figure 4.1a, n-type semiconductor with $\phi_S<\phi_M$), electrons will flow from the semiconductor to the metal to equilibrate the E_{Fs}. As a consequence, the region close to the interface of the metal is negatively charged and, due to electrostatic induction, an equal and opposite charge must exist in the semiconductor. Because of the low concentration of free carriers in the semiconductor, the induced electric field at the interface is not effectively screened. Therefore, the positive charge excess is distributed over a barrier region near the semiconductor interface, called depletion layer (lack of electrons) or more generally space charge region (SCR)[7-10].

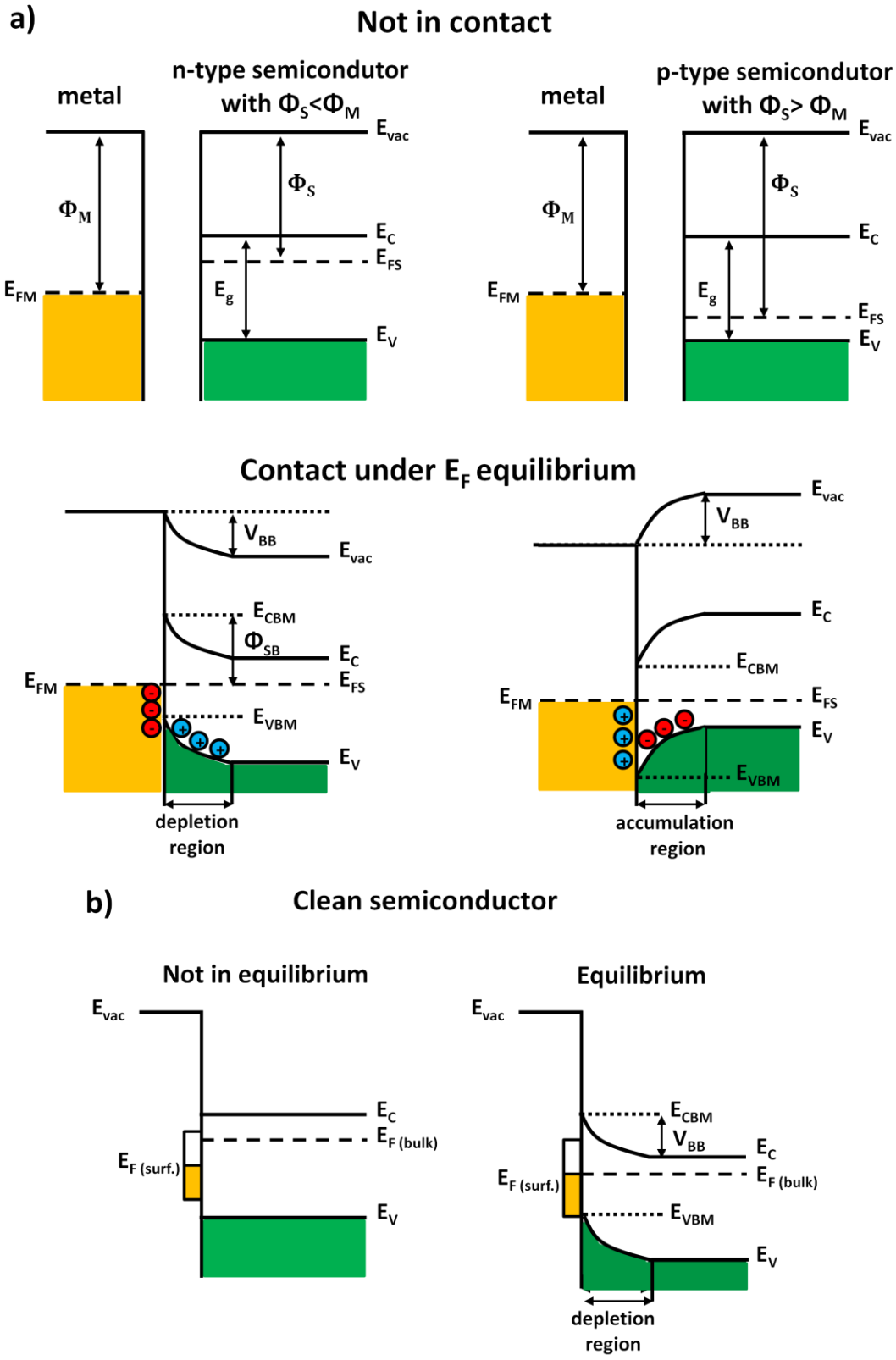

Figure 4.1 *Energy band diagrams of* **a)** *n- and p-type semiconductor contacts (equilibrium condition) and* **b)** *near the surface of a clean semiconductor (n-doped) before and after equilibrium of the bulk and surface E_F. E_{vac} is the vacuum energy, E_V and E_C are the energy of valence and conduction band*

minimum, and E_{VBM} and E_{CBM} are the energy of valence and conduction band maximum. See the text for more details.

In other words, over the whole SCR the energy band edges are continuously shifted (upward in this case). This is called band bending (V_{BB}). As a consequence, a barrier is formed at the semiconductor interface, called Schottky barrier (ϕ_{SB}). In the second case (p-type semiconductor with $\phi_S > \phi_M$), the E_F equilibrium will be achieved by electron flow from the metal to the semiconductor and the SPR is called accumulation layer (downward band bending). A conceptually identical scheme is adopted for the clean doped semiconductor case (Figure 4.1b). The semiconductor bulk E_F has to equilibrate with the surface states E_F. Usually, the surface E_F is pinned by the surface states in the mid of the gap. This is because the density of surface states is larger ($\sim 10^{15}$ cm^{-2}) than that of the bulk dopant states ($\sim 10^{8}$–10^{12} cm^{-2}). Therefore, the bulk dopant concentration does not alter the surface E_F[7-10].

The SPV effect can be schematized in three steps (Figure 4.2)[8,11]. When photons (with enough energy to promote a band-to-band transition) are absorbed by a semiconductor system, electron-hole pairs are generated. In the second step, the photo-excited electron-hole pairs are separated by the induced surface/interface electric field, generating free carriers. Depending on the direction of the electric field the free charges will move in opposite directions. As a consequence, an accumulation of charges (positive or negative) will be present near the surface/interface, generating a voltage called SPV. The generated SPV lowers the degree of band bending[1-3,8-11]. In the final step, the equilibrium is restored by the transport of electrons through thermoionic emission over the surface/interface potential barrier. In other words, the absorption of photons induces a change in the surface potential which causes band flattening. A similar effect is observed using electron fluxes, in this case, is called surface voltage (SV)[12,13].

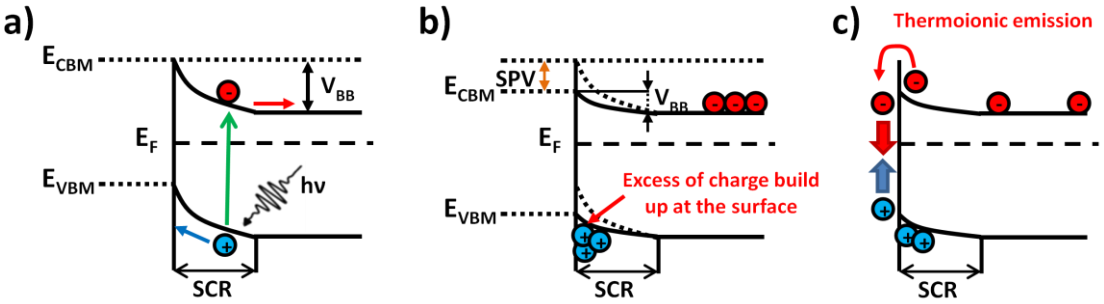

Figure 4.2 *Schematic representation of the SPV effect by a three step model in a n-type semiconductor:* **a)** *and* **b)** *evolution of the SPV in a n-type semiconductor, and following relaxation through* ***c)*** *the thermionic effect. E_V and E_C are the energy of valence and conduction band minimum, and E_{VBM} and E_{CBM} are the energy of valence and conduction band maximum.*

The E_F position is the most important bulk parameter in determining the degree of band bending. However, several additional factors determine the SPV magnitude and relaxation dynamics as the temperature, dopant and defects concentration, surface velocity recombination and the incident photons/electron flux, among others[1-3,8-11]. As a consequence, the SPV/SV dynamics can occur in an extremely wide temporal range, from ps to seconds, depending on the condition of the system[1,2,5,14-17]. Unlike many relaxation dynamic processes, the SPV decay is not a simple exponential. The potential barrier at the surface/interface is itself a function of time. After the generation of free carriers (non-equilibrium situation), the majority carriers start to restore the equilibrium by recombining with the accumulated charges close to the interface/surface via thermoionic emission (restoring the band bending). This is the step with the highest decay rate. Since the degree of band bending is gradually restored, (V_{BB} increases) the decay time becomes slower until the barrier is completely restored (SPV=0). The SPV can be seen as a continuously decelerating process.

4.2 The LEINEC code

During my PhD, I developed the LEINEC (Light/Electron Induced Non-Equilibrium phenomena Calculator) code to model and evaluate the SPV/SV effect in semiconductor surfaces and interfaces. LEINEC uses two different theoretical models based on a priori calculations[1-3]. Both models are based on the thermoionic field-emission theory developed by Schottky and Mott in 1938, used to explain the current transport in metal-semiconductor contact at thermal equilibrium[7]. The thermoionic field-emission theory is based on three fundamental assumptions:

1. The barrier height is much larger than K_BT (where K_B is the Boltzmann constant and T the temperature).
2. The thermal equilibrium is achieved at the plane of emission, hence the current-limiting process is the actual transfer of electrons across the interface between the semiconductor and the metal. The effects of drift and diffusion in the depletion region are assumed to be negligible, which is equivalent to assuming infinite mobility. It follows that the quasi-Fermi level (E_F*) of electrons remains flat throughout the depletion region and coincides with the E_F in the bulk.
3. The existence of a net current flow does not affect the equilibrium condition. This implies the possibility to consider two opposite currents in balance from the semiconductor to the metal and form the metal to the semiconductor, with different E_F*. Furthermore, the barrier shape becomes irrelevant: the current flow depends only on the barrier height value.

Accordingly, the net current is given by the relation:

$$J = A^* T^2 e^{\left(\frac{-q\Phi_{SB}}{K_B T}\right)} e^{\left(\frac{qV}{K_B T}\right)} \qquad (4.1)$$

where A* is the Richardson constant, Φ_{SB} is the Schottky barrier, q is the elemental electron charge, and V is the induced difference of potential (SPV/SV) due to the external perturbation. However, several factors are not considered. The carrier diffusion, tunnelling current, image charge effect and leakage current are neglected. The surface recombination velocity is considered small or negligible (generally not true). Anyway, despite the simplicity and the drastic approximations, the model well predicts the behaviour of many semiconductor systems. The first of the two models, namely *model 1*, calculates the steady-state SPV effect by using eq. 4.1. (the SPV magnitude soon after the photon or electron flux excitation). Following the Hecht's model of Schottky barrier[3] it has been proposed a derivation of this equation able to model the evolution in time of the SPV:

$$\tau(SPV) = \tau_D e^{\left(-\frac{SPV}{\eta K_B T}\right)} \qquad (4.2)$$

Where τ_D is the "dark" carrier lifetime and η is the ideality factor of a Schottky diode. The amount of charge carriers at the surface is connected to the SPV by the expression (valid for $K_BT \ll SPV \ll |V_{BB}|$)[17-20]:

$$\frac{SPV}{K_B T} e^{\left(\frac{SPV}{K_B T}\right)} = \frac{n_p}{n_0} e^{\left(\frac{|V_{BB}|}{K_B T}\right)} \qquad (4.3)$$

where n_0 is the doping carrier concentration, and n_p is the photo-excited carrier concentration ($n_p/n_0=\Delta_p$). The dependence of the SPV decay time leads to a decay equation for the surface charge given by[17]:

$$\frac{d\Delta_p}{dt} = \frac{-\Delta_p}{\tau(SPV)} \qquad (4.4)$$

Combining the eq. (4.3) and (4.4) the differential equation is solved:

$$SPV(t) = -\eta K_B T \ln\left(1 - \left(1 - e^{\left(\frac{SPV_0}{\eta K_B T}\right)}\right) e^{\left(-\frac{t}{\tau_D}\right)}\right) \qquad (4.5)$$

where SPV_0 is the maximum value of the SPV magnitude after excitation.

The second model, namely *model 2*[1,2 and refs therein], as the first approximation considers only the SPV due to excitation of surface states and photon absorption in the space charge region, assuming negligible the contribution from the bulk (diffusion of photo-generated free electrons and holes from the bulk). It assumes that the SPV is primarily caused by a variation in the negative charge density at the semiconductor surface and that the total density of the acceptor and donor states is located at the interface. The sources of surface charges can be due to absorbed species on the surface or to semiconductor contacts and interface states. In the first case, the charge is considered fixed and the exchange of electrons is very slow. In the second case, the photo-generated carriers quickly interact with the surface charge, and transitions via surface states are assumed to be fast. The capture and emission of electrons close to the surface/interface in the two cases are considered by an

electron capture coefficient. Accordingly, a general equation that describes two situations, steady-state condition and SPV decay, is obtained:

$$-\frac{n_s(0)}{2V_{BB}\sqrt{1-\frac{SPV}{V_{BB}}}}\frac{dSPV}{dt} = R_0 e^{\frac{SPV}{\eta K_B T}} - R_0 - R^* \qquad (4.6)$$

Where $n_s(0)$ is the initial surface charge of the semiconductor, R_0 is the bulk to surface flow of carriers in dark conditions and R* is the bulk to surface flow of photo-generated electrons/holes.
Under continuous illumination the steady-state situation is achieved and the SPV reach a "saturation" (SPV_0) value (dSPV/dt=0) and the eq. 4.6 can be written as:

$$SPV_0 = \eta K_B T \ln\left(\frac{R^*}{R_0} + 1\right) \qquad (4.7)$$

This equation can be compared to the one derived within the classic thermoionic emission theory:

$$SPV_0 = \eta K_B T \ln\left(\frac{I_{ph}}{j_0} + 1\right) \qquad (4.8)$$

Where I_{ph} is the current due to photo-generated carriers, and j_0 is the saturation current in a Schottky diode. However, in this model have been introduced terms that specifically consider the carrier diffusion, the surface velocity recombination as well as the attenuation of the incident photon flux passing through the semiconductor.
Switching off the illumination, the SPV from the saturation value $SPV=SPV_0$ (at $t=t_1=0$) after a certain time (t_2) will decrease to SPV=0. The bulk to surface flow of photo-generated electrons/ holes stops, therefore R*=0. And from the eq. 4.6, in the case of $SPV \ll V_{BB}$, it is obtained:

$$t_2 \approx \frac{n_s(0)}{2V_{BB}R_0}\left(SPV(t_2) - SPV_0(t_1) + \eta K_B T \ln\left(\frac{e^{\frac{SPV_0(t_1)}{\eta K_B T}} - 1}{e^{\frac{SPV(t_2)}{\eta K_B T}} - 1}\right)\right) \qquad (4.9)$$

From the comparison of the two models (eq. 4.5 and 4.9), it is possible to note that in *model 1* the SPV decay can be modelled just by using two parameters τ_D and η (for a fixed T). On the contrary, *model 2* considers several additional parameter characteristics of the semiconductor system. The calculation of $n_s(0)$ involves the dopant concentration and the degree of band bending. In the R* calculation are included the SPR width and the photon flux (as well as its intensity decrease passing through the sample). In R_0 are included the surface velocity recombination, the density of donor/acceptor states and the shift of EF due to the dopant concentration. All these additional parameters offer a more versatile model to reproduce the experimental data, involving a larger set of properties of the system studied in the calculation. As it will be shown in the following of this chapter, the *model 1*, due to its simplicity presents critical aspects to be overcome. The ideality

factor, η, is intended as a phenomenological parameter[16] which in many cases becomes a "corrector factor" to accurately reproduce the experimental data. In literature are reported simulations which use η values completely out of the optimal range of 0.5-2 (>10)[11,14,21], leading to questioning its effective physical meaning in these cases.

Figure 4.3 shows the interface of the LEINEC code and the two types of output obtained by performing a simulation, the steady-state SPV 3D map and the SPV decay curve for a fixed SPV magnitude. LEINEC allows simulating the SPV steady-state dependence in a wide range of parameters (dopant concentration, temperature, band bending and photon flux) producing a graphical 3D output. An example is shown in Figure 4.3b where the SPV magnitude is modelled as a function of a range of V_{BB} and photon fluences.

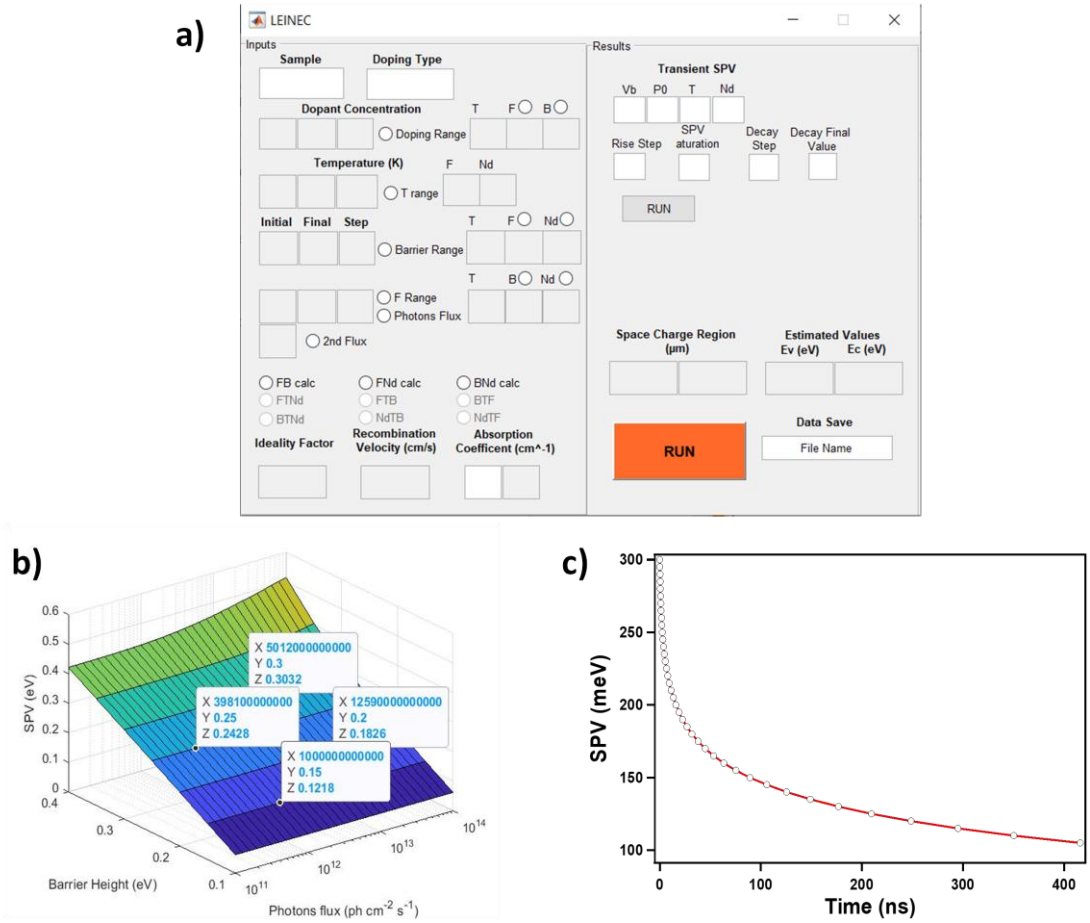

Figure 4.3 a) *Graphical interface of the LEINEC code; examples of graphical outputs of* ***b)*** *a steady state SPV simulation as a function of the photon flux and the barrier height and of* ***c)*** *the SPV relaxation dynamics for a fixed SPV initial shift of 300 meV. In Figure 4.3b X is the photon fluence, Y is the barrier height and Z is the SPV magnitude.*

Once determined the SPV magnitude after photon or electron excitation, it is possible to simulate its evolution in time (Figure 4.3c). However, several additional chemical-physical properties are considered to correctly evaluate the SPV effect, such as the dielectric constant, effective electron/hole mass, exciton binding energy, the density of the states of

the valence and conduction band, band gap, intrinsic carrier concentration and absorption coefficient. All these parameters can be included in the calculation by compiling an external file, which LEINEC automatically recall during the simulation. In this way, it is possible to create a virtual library and simulate every desired semiconductor system.

4.2.1 SPV parameter dependence

The most important parameters which strongly influence and determine the SPV magnitude and the relaxation dynamics can be summarized in the band gap, surface velocity recombination, dopant concentration, number of defects, temperature and incident photon/electron flux[1-3]. The role of the incident photon flux is the more intuitive among all. The magnitude of the SPV is determined by how many free charges are generated in the semiconductor. Higher fluxes will increase the possibility to generate more free electrons and holes increasing the SPV magnitude. However, the number of generated free charges is also related to the absorption coefficient of the material. Depending on the temperature the recombination of the free electrons and holes can be more or less effective. Lowering the temperature the diffusion length of free charges is enhanced and there is a higher probability that they reach the surface/interface without recombining. The effect of the dopant concentration is more complex.

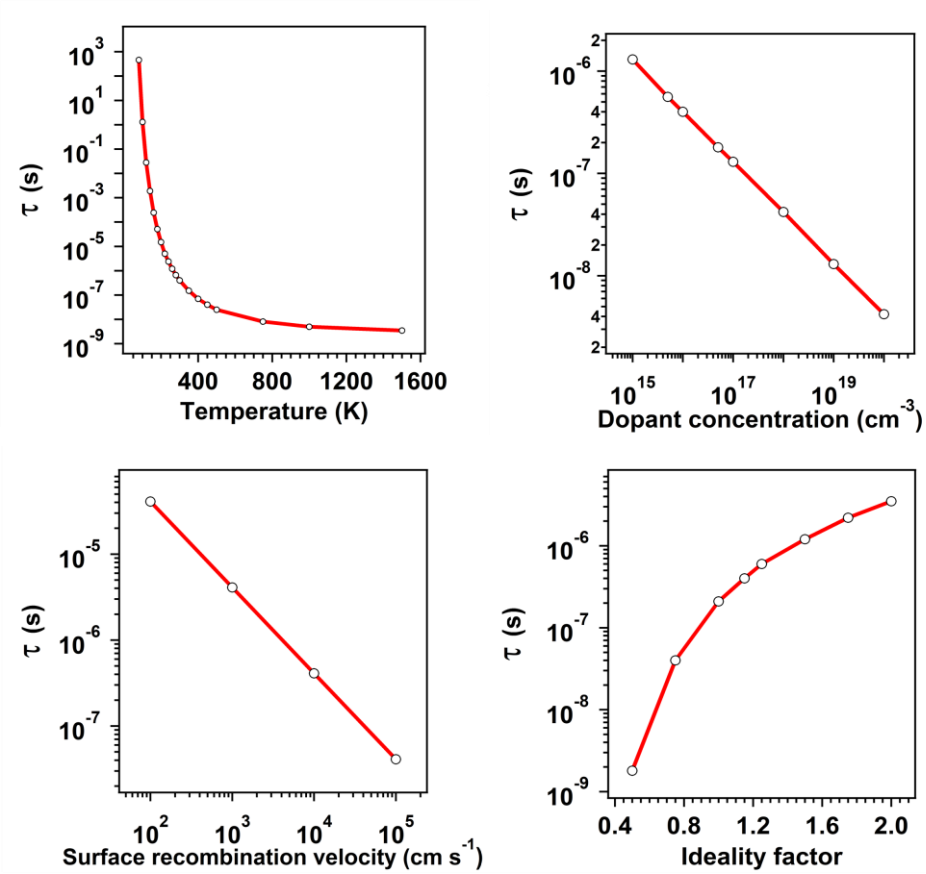

Figure 4.4 *Simulation of the SPV decay time (τ) as a function of the temperature* **(top left)**, *dopant contrantion* **(top right)**, *surface recombination velocity* **(bottom left)** *and ideality factor* **(bottom right)** *in a p-Si/SiO_2 system with SPV magnitude of 300 meV after photon excitation. For a given variable, the other parameters were set as T= 298 K, dopant concentration=10^{15} cm^{-3}, surface velocity recombination= 10^3 cm s^{-1} and ideality factor= 1.*

Band bending is due to the lack of free carriers in the semiconductor to screen the induced electric field. The doping of a semiconductor provides free electrons or holes. As a consequence, the width of the SCR is reduced as the dopant concentration increases. When the SCR is thin the charges can tunnel through the barrier and increase the recombination efficiency lowering the SPV effect[22-24]. On the other hand, increasing the dopant concentration the E_F is shifted toward the conduction or valence band, tuning the difference in work function between the materials in contact. In this case, the degree of band bending may be enhanced or lowered. Concerning the surface recombination velocity, it is clear that a low value (low recombination rate) leads to higher SPV magnitude and vice versa. Finally, the defects can influence two of the parameters above discussed. Defects lead to the formation of trap states which enhance the probability of recombination of the free carriers. On the other hand, defects can act as a dopant in semiconductors. Anion or cation vacancies lead to intrinsically n- or p-doped semiconductors, representing a similar case of the dopant concentration effects.

A simulation of the influence of these parameters on the SPV relaxation dynamics is shown in Figure 4.4 (SiO_2/p-Si sample with SPV magnitude= 300 meV after irradiation). In all cases, the SPV relaxation dynamic shows a strong variability. Differences of several orders of magnitude are observed by varying only one parameter. However, the most important difference can be noted as a function of the temperature. The SPV decay time (τ) ranges from ns to hundreds of s by varying the temperature from 1000 K to 80 K, respectively. Finally, Figure 4.4 shows the SPV decay time as a function of the ideality factor. In the models is introduced as a phenomenological factor in terms of describing the capture of free electrons by surface states, having a similar meaning to the ideality factor in Schottky diodes[7]. But unlike for Schottky diodes, where η varies between 1 and 2, here η ranges from 0.5-2 for different models of a free surface[25]. For example, $\eta<1$ when trapping occurs at the surface/interface and $\eta\sim2$ when significant trapping occurs in the SCR[26].

4.3 LEINEC simulations of SPV and SV effects in GaAs, GaP and SiO_2/Si systems

The validity of the code in predicting the static and transient SPV has been tested in inverse photoemission and photoemission data sets from the literature[4,5,6] (Figure 4.5). The reported IPES spectra of GaP and GaAs samples were recorded out of this thesis work. The n- and p-GaAs(110) wafer have $2x10^{18}$ cm^{-3} (S doped) and $5x10^{17}$ cm^{-3} (Zn doped) dopant concentration. The n-GaP(110) sample (S doped) has $3x10^{17}$ cm^{-3} dopant concentration.

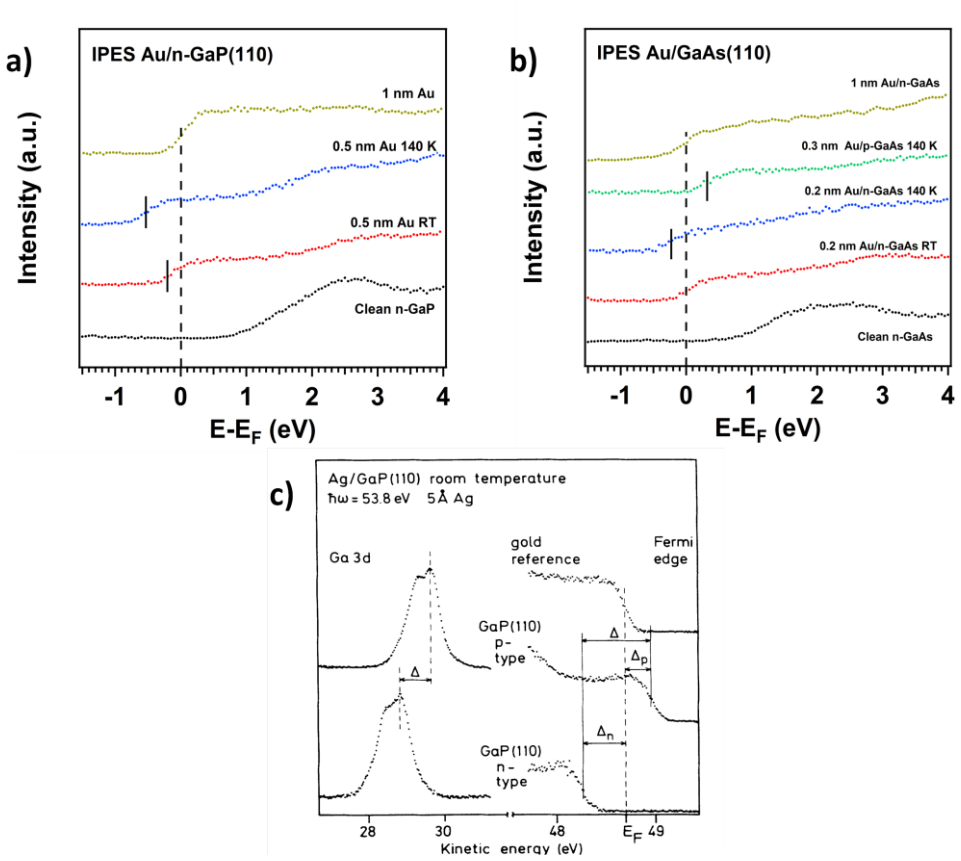

Figure 4.5 a) *Au/n-GaP(110) and* **b)** *n- and Au/p-GaAs(110) IPES spectra at RT and 140 K;* **c)** *n- and p-doped Ag /GaP(110) PES spectra from ref. 4.*

The clean GaP(110) and GaAs(110) surfaces were obtained by cleaving *in situ* pre-notched bars of section 5x5 mm^2. Thin layers of Au (few Å) were grown on the GaP and GaAs surfaces by thermal evaporation in UHV from a resistively heated tungsten basket keeping the samples at room temperature. The SV effect was detected by IPES on both systems and a thermoionic field emission model for the GaP system was published in the past[7]. The n- and p-doped GaP spectra are reported from PES measurements of ref. 4. The n-GaP(110) (S doped) and p-GaP(110) (Zn doped) samples of ref. 4 have dopant concentrations of 2x10^{17}-2x10^{18} cm^{-3} and 3.7 x10^{17} cm^{-3}, respectively. The SPV shifts in the PES data (Ga 3d and VB) were recorded for a metal deposition equivalent to 5 Å at room temperature for both (Figure 4.5c). The corresponding spectrum of the Au E_F reference is shown on the right side (Au reference). An SPV shift of -0.46 eV and +0.26eV to the E_F of the Au reference was observed for the n- and p-doped Ag/GaP(110) systems, respectively. The IPES spectra of n-GaP, n-GaAs and p-GaAs samples with Au deposition 1 nm are shown in Figures 4.5a and b. Depending on the temperature different shifts, due to the SPV effect, are observed. In the case of the Au/n-GaP system shifts of -0.25 eV and -0.5 eV are detected by measuring at RT and 140 K, respectively. The Au/GaAs systems show shifts of –0.2 eV in the n-doped and of +0.35 eV in the p-doped sample at 140 K. No shift is observed at RT for both. As expected an increase in the SPV magnitude is observed by decreasing the temperature.

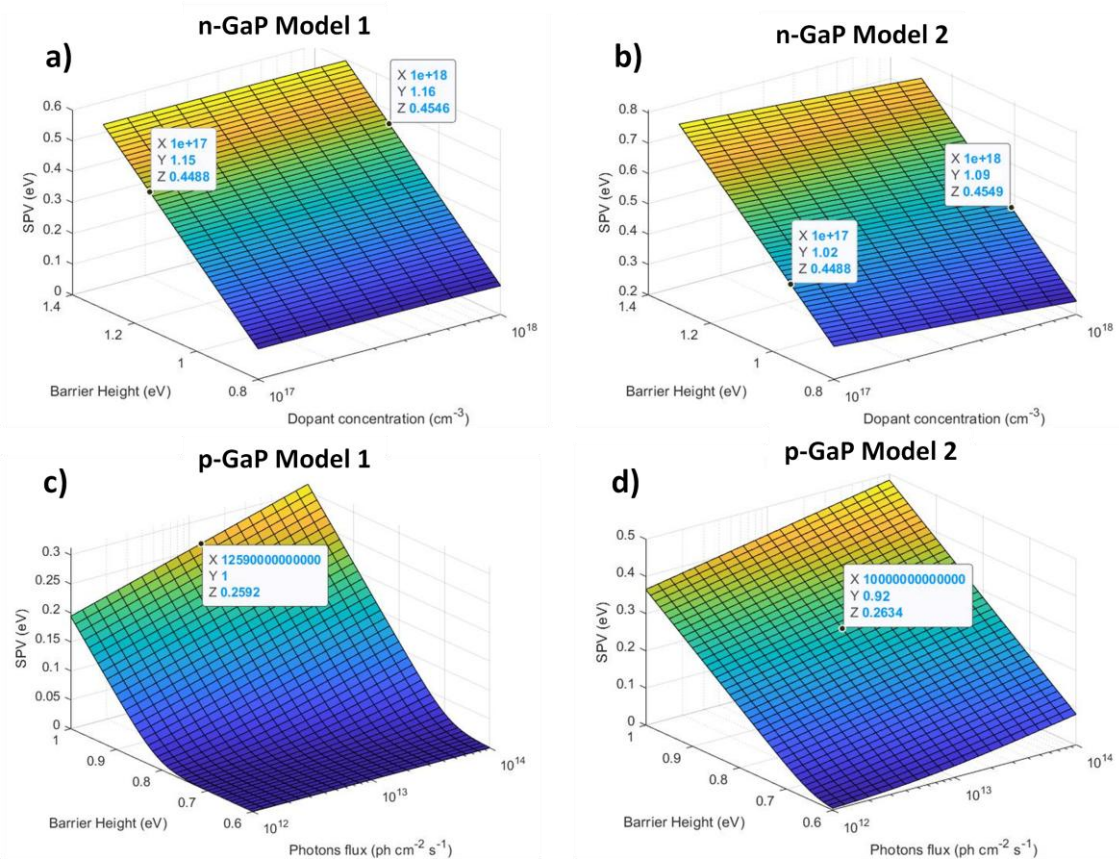

Figure 4.6 *LEINEC evaluations of the SPV effect in PES spectra of* **a) b)** *n-GaP and* **c) d)** *p-GaP samples of ref. 4. The simulations are performed as a function of the barrier height and photon flux by using the models 1 and 2. X is the photon flux, Y is the barrier height and Z is the SPV magnitude.*

Sample	PES SPV shift (eV)	Literature barrier height (eV)	Model 1 barrier height (eV)	Model 2 barrier height (eV)
n-GaP	0.45	0.9-1.1a	1.15	1.05
p-GaP	-0.26	0.76-0.88a	1	0.92

Table 4.1 *Summary of the SPV shifts observed in PES spectra (ref. 4), barrier height values from the literature and the calculated barrier height of the n-GaP and p-GaP samples.* [a]*refs. 27,28.*

Lowering the temperature the efficiency of the recombination processes is reduced and the charge mobility enhanced. The LEINEC simulations of the steady-state SPV shift of the PES and IPES spectra are shown in Figures 4.6 and 4.7, respectively.

The PES data from ref. 4 are accurately reproduced. The SPV shifts observed in PES spectra and the results of the code simulations are summarized in Table 4.1. An S_{RV} value of 10^3 cm s^{-1} and unitary η were used in the *model 2* simulations. It should be noted that in

this case by adjusting the η it is possible to obtain a more accurate value of Φ_{SB} for a fixed SPV shift.

The SV shifts observed in IPES spectra and the results of the code simulations are summarized in Table 4.2. The reported LEINEC simulations (Figure 4.7) were performed only by the *model 1*, because the model 2 is not able to calculate SV effect induced by electron fluxes. The reference values of the barrier height at RT for the GaP and GaAs samples were known from literature[27-30]. No reference was reported for the low temperature case of 140 K. However, as a general rule the Schottky barrier dependence on the temperature can be approximated by[31,32]:

$$\Phi_{SB} = \frac{1}{2}\left(E_g - \frac{\Delta}{3}\right) + \delta_m \qquad (4.10)$$

where E_g is the semiconductor indirect band gap, Δ the spin-orbit splitting and δ_m is a parameter that depends on the metal deposited over the semiconductor surface. Considering the increase of E_g lowering the temperature, the barrier height of both n- and p-type samples should equally increase with decreasing temperature. However, from 300 K and 140 K, the decrease of E_g in both samples is very low, from 1.48 eV to 1.42 eV in the GaAs and from 2.42 eV to 2.36 eV in the GaP. Accordingly, assuming comparable values of Φ_{SB} at 140 K and RT should not be a drastic approximation. As can be seen in Table 4.2, the *model 1* well reproduces the IPES data.

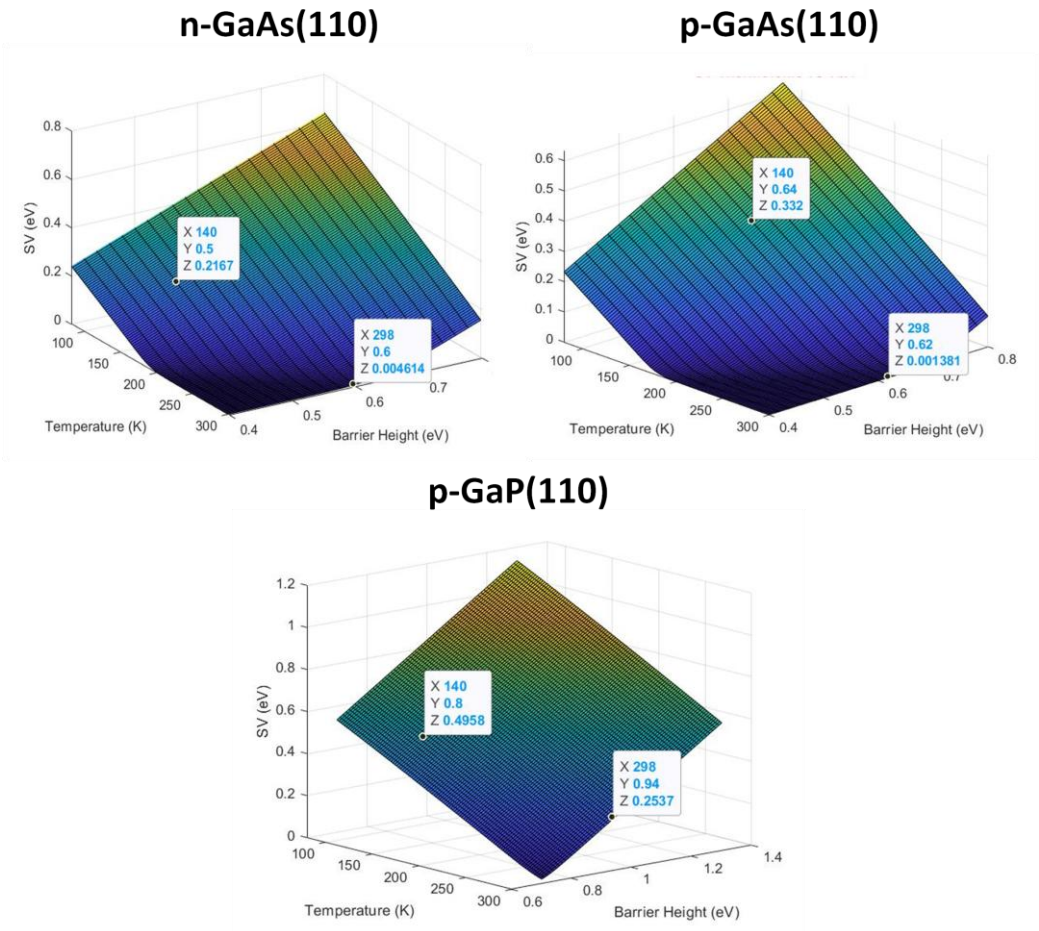

Figure 4.7 *LEINEC evaluations of the electron-induced SV effect in IPES spectra of the GaAs and GaP samples. The code calculates the SV magnitude in fixed ranges. In this case the SV degree as a function of the temperature and barrier height. X is the temperature, Y is the barrier height and Z is the SV magnitude.*

Sample	IPES SV shift (eV)		Literature barrier height (eV)		Model 1 barrier height (eV)	
	RT	140 K	RT	140 K	RT	140 K
n-GaP	-0.25	-0.5	0.9-1.1[a]	-	0.94	0.80
n-GaAs	0	-0.2	0.65-0.8[b]	-	0.6	0.5
p-GaAs	0	0.35	0.6-0.7[b]	-	0.62	0.64

Table 4.2 *Summary of the SV shifts observed in IPES spectra (ref. 6), barrier height values from the literature and the calculated barrier height using the model 1 of the n-GaP, n-GaAs and p-GaAs samples.* [a]*refs. 27,28 and* [b]*refs. 29,30.*

For a barrier height of about 0.6 eV, no SPV effect is predicted for both n- and p-GaAs samples at RT. In the p-GaAs case, the assumption of a similar Φ_{SB} value at 140 K to RT is valid. For a shift of +0.35 eV, it is estimated a 0.64 eV barrier. In the n-GaAs case, a slight deviation is observed. For low temperature, the code predicts a barrier height of 0.5 eV. In the n-GaP sample, for an SPV shift of -0.25 the code estimates a Φ_{SB} in agreement with the literature (0.94 eV), but also in this case a slightly lower Φ_{SB} is predicted at 140 K (0.8 eV).

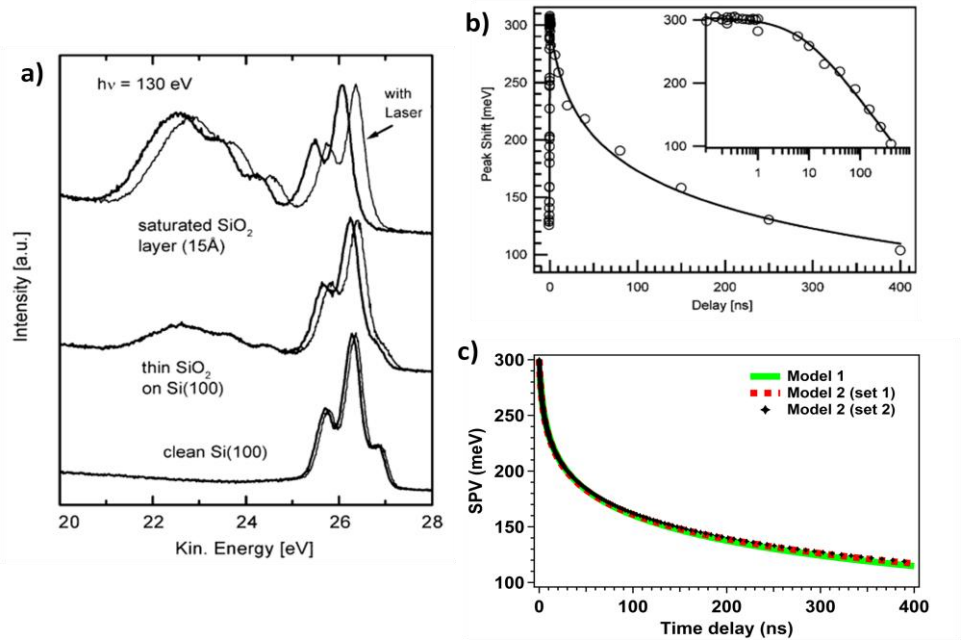

Figure 4.8 a) *Si 2p XPS of the SiO_2/Si(100) sample with and without synchronized laser illumination (λ= 1064 nm, laser fluence 10 μJ/cm^{-2}, Δt= 50 ps) from ref. 5;* **b)** *Si 2p peak shift of the SiO2/Si(100) sample (15 Å oxide layer) as function of the time delay (ref. 5). The inset shows the data on a logarithmic time scale;* **c)** *LEINEC simulations of the Si 2p peak shift (SPV effect) by means of the model 1 and of the model 2 (by using two different set of parameters, set 1 and set 2).*

Model	η	τ_D (μs)	N (cm^{-3})	SRV (cm s^{-1})
1	1.3	12	-	-
2 (set 1)	1.25	-	$5x10^{16}$	$4.4x10^{3}$
2 (set 2)	1.25	-	$1x10^{15}$	$3x10^{4}$

Table 4.3 *Summary of the parameters used in the model 1 and 2 to reproduce the SPV decay curve of the $Si2p_{3/2}$ core level shift of ref. 5. Set 1 and set 2 refer to different sets of parameters that accurately reproduce the experimental data.*

Validated the efficiency of the code in predicting the steady-state SPV effect, a further test was performed for the transient SPV case. The LEINEC code was used to simulate the evolution in time of the SPV shift observed in a p-Si/SiO_2 system of ref. 5. The PES and TR-PES data are reported in Figure 4.8. They observed an increasing shift of the Si2p peak energy as a function of the oxide layer thickness, reaching an SPV saturation value of 300 meV for a 1.5 nm SiO_2 nominal thickness (Figure 4.8a). Figure 4.8b shows the SPV decay curve of the 300 meV Si2p core level shift (empty dots). The solid curve is the simulated SPV decay curve of ref. 5 by using the same model, namely *model 1* in this thesis. The parameters used in ref. 5 to model the SPV shift over time are reported in Table 4.3. Since the *model 1* was successfully used to reproduce the experimental data, in the following only the results of the *model 2* are discussed. The *model 2* requires more specific parameters than the *model 1*, such as the dopant concentration (N), the surface velocity recombination (S_{RV}), and the degree of band bending (V_{BB}), among others. Unfortunately, in ref. 5 the sample doping is not reported, and the S_{RV} value in an oxidized Si system can range from 10^2 to 10^4 cm s^{-1} [33]. Furthermore, the PES spectra are reported in kinetic energy: from the $Si2p_{3/2}$ binding energy, it is possible to calculate the V_{BB} value[14,34,35]. Therefore, three variable parameters were present during the code simulations. However, by increasing the photon fluence no further SPV shift was observed after 300 meV, indicating the achievement of the SPV saturation. Accordingly, a V_{BB} value equal to the SPV saturation was assumed as an approximation (flat band condition). It should stress that this assumption is not generally true: theoretically, the SPV saturation value should represent the degree of band bending, but in literature, SPV saturation values lower than the estimated band bending are observed[14]. The decay curves obtained by using the *model 2* are shown in Figure 4.8c together with that one of the *model 1* for comparison. The parameters used to model the SPV decay curve are summarized in Table 4.3. By using the *model 2*,

two sets of parameters accurately reproduce the experimental data. This is a consequence of the presence of two variable parameters, S_{RV} and N. In both, the SRV ranges in the possible values reported in the literature. Concerning N, considering the notable SPV shift of 300 meV it was possible to assume a low dopant concentration. Pierucci et al.[14] reported an SPV shift of about 100 meV for a SiO_2/p-Si sample with a dopant concentration of $7.5x10^{14}$ cm^{-3}. No SPV shift was observed for high doping ($4x10^{19}$ cm^{-3}). Accordingly, an estimation of the dopant concentration in the range 10^{15}-10^{16} cm^{-3} seems reliable. It should be stressed that also η was a possible variable. However, its value strongly determines the curve shape. To accurately reproduce the shape of the experimental curve it was necessary to assume an η value of 1.25, a value comparable to that of the *model 1* (η =1.3).

4.4 Study of the SPV dependence on the photon flux and doping in SiO_2/Si(100) systems

The dependence of the SPV dynamics on the type of dopant and photon flux in SiO_2/Si(100) systems was studied by TR-PES. The p-doped (B) and n-doped (As) samples have dopant concentrations (N) $8x10^{14}$ cm^{-3} (16.85 Ω×cm) and $1.6×10^{19}$ cm^{-3} (0.004 Ω×cm), respectively. The dopant concentration was calculated from the sample resistivity[7]. The steady-states of the samples were characterized by PES. All measurements were performed at room temperature. From the Si2p core level it was determined the E_F position (E_F - E_{VBM}) and the degree of band bending (V_{BB}) at the SiO_2/Si interface as given respectively[14,34,35]:

$$(E_F - E_{VBM}) = E_B Si2p_{3/2} - 98.74\ eV \qquad (4.11)$$

and

$$V_{BB} = (E_F - E_V) - (E_F - E_{VBM}) \qquad (4.12)$$

where 98.74 eV is the energy difference between the valence band maximum and the $Si2p_{3/2}$ core level[34,35]. Since PES is surface-sensitive, the E_F - E_V value (E_v is the valence band energy position in the bulk) is determined according to[7]:

$$(E_F - E_V) = K_B T \ln\left(\frac{N_V}{N}\right) \qquad (4.13)$$

Where N_v is the effective density of states in the valence band and N is the density of acceptors or donors. Figure 4.9 shows the Si2p core level of the n- and p- SiO2/Si(100) samples after 3 hours of annealing at 800 K. The Si $2p_{3/2}$ peak is located at 99.38 eV and 99.53 eV in the p-doped and n-doped samples, respectively. The PES spectra were referenced to the Au E_F directly in contact with the samples. Accordingly to eq. 4.11, the degree of band bending results of -0.37 eV and +0.32 eV in the p-doped and n-doped sample, respectively. The oxide layer nominal thickness was estimated of about 2 nm

(calculated by the area ratio between the Si and SiO_2 peaks). The properties of both samples are summarized in Table 4.4. The SiO_2/p-Si(100) sample will be discussed first. Figure 4.10a shows the Si2p peak measured before and at t=0 ns (SPV maximum value after pump excitation) by using 15.5 µJ cm^{-2} of pump fluence (λ= 343 nm). A notable shift of 95 meV toward lower binding energy, due to the SPV, is observed. Additional TR-PES measurements using different pump fluencies were performed to verify the SPV saturation condition. The SPV magnitude varies from 45 meV to 95 meV by increasing the pump fluence from 0.066 µJ cm^{-2} to 15.5 µJ cm^{-2}. However, the SPV saturation of 95 meV is already achieved with 0.46 µJ cm^{-2} pump fluence (Figure 4.10b). Notably, by using the higher pump fluence (15.5 µJ cm^{-2}), the SPV temporal evolution differs from the others involving two dynamical processes. This is shown in Figure 4.10c.

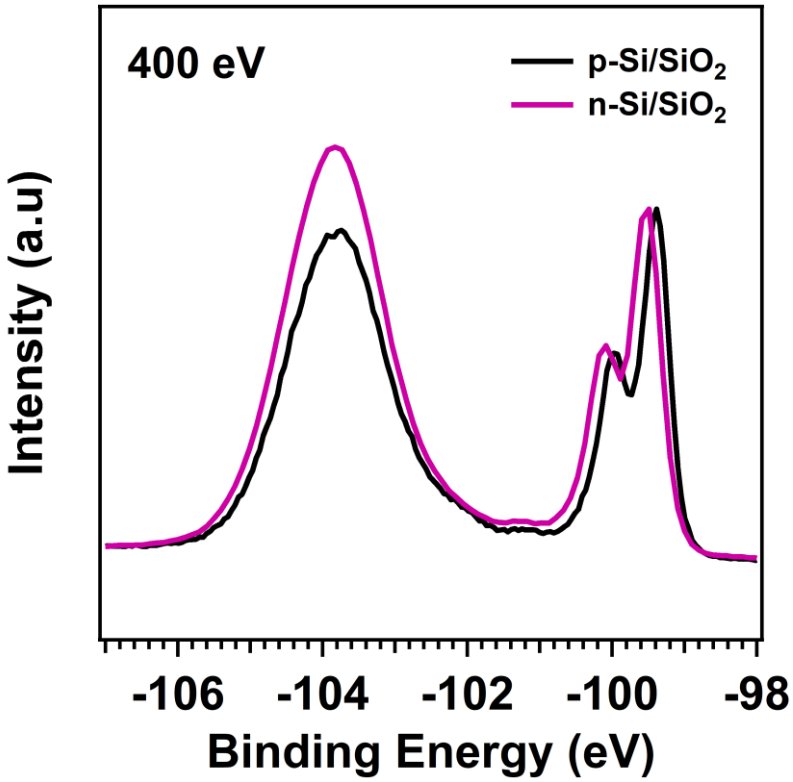

Figure 4.9 *Si2p core levels of the SiO_2/p-Si(100) and SiO_2/n-Si(100) samples by using hv=400 eV of photon energy.*

Type	ρ (Ωxcm)	Doping (cm^{-3})	$Si2p_{3/2}$ (eV)	E_F-E_{VBM} (eV)	E_F-E_V (eV)	V_{BB} (eV)	SCR (nm)
p	16.85	$8x10^{14}$	99.38	0.64	0.27	-0.37	800
n	0.004	$1.6x10^{19}$	99.53	0.79	1.11	+0.32	5

Table 4.4 *Summary of the SiO_2/p-Si(100) and SiO_2/n-Si(100) sample properties. The SCR is calculated from equation*[7] $SCR = \sqrt{\frac{2\varepsilon\varepsilon_0|V_{BB}|}{qN}}$, *where ε and ε_0 are the material and vacuum permittivity, respectively, and q the elementary charge of the electron.*

The estimated decay times using different pump fluencies are summarized in Table 4.5. It is necessary to stress that the SPV relaxation dynamics is a non-exponential decay. The attempt to approximate the data by a sum of different exponential decays has to be intended only as a rough estimation of reference values for the following discussion. Actually, using a high fluence, after an initial fast relaxation (τ_1), the decay curve shows an identical temporal evolution of the $Si2p_{3/2}$ energy shift with comparable decay time (τ_2) to the lower fluence case.

Figure 4.11a shows the $Si2p_{3/2}$ core level of the SiO_2/n-Si(100) sample measured before the pump pulse and at t=0 ns (111 µJ cm^{-2} pump fluence). Also in this case an energy shift, due to the SPV, is observed. However, despite the use of a higher flux than in the case of the p-doped sample, it shows a lower SPV magnitude. No SPV is observed for lower fluencies (not shown). The SPV decay curve (Figure 4.11b) shows a faster relaxation dynamic, with τ= 1.6 ns (Table 4.5), as compared to the p-doped sample. This is expected because of the higher dopant concentration. Increasing the doping the SCR width is reduced. When the SCR is thin the charges can tunnel through the barrier and increase the recombination efficiency[22-24]. Several works in literature report SPV relaxation dynamics of similar n- and p-doped SiO_2/Si systems (comparable dopant concentration and oxide layer thickness) to this work[5,14,17]. However, the SPV magnitude and decay time differ case by case. Bröcker et al.[17] report an SPV relaxation dynamics of a SiO_2/p-Si sample evolving over 800 ns. Pierucci et al.[14] observed the complete decay of the SPV in the range of tens of µs. In this study, the p-doped sample shows an even faster relaxation dynamics of about 100 ns. Finally, in the case of SiO_2/n-Si system[14], a relaxation dynamics of hundreds of ns is reported, in contrast to our observation of about 1 ns. To clarify the origin of such differences, the relaxation dynamics observed in this study were modelled by LEINEC. In the following, the simulation results are discussed and compared to the results reported in the literature.

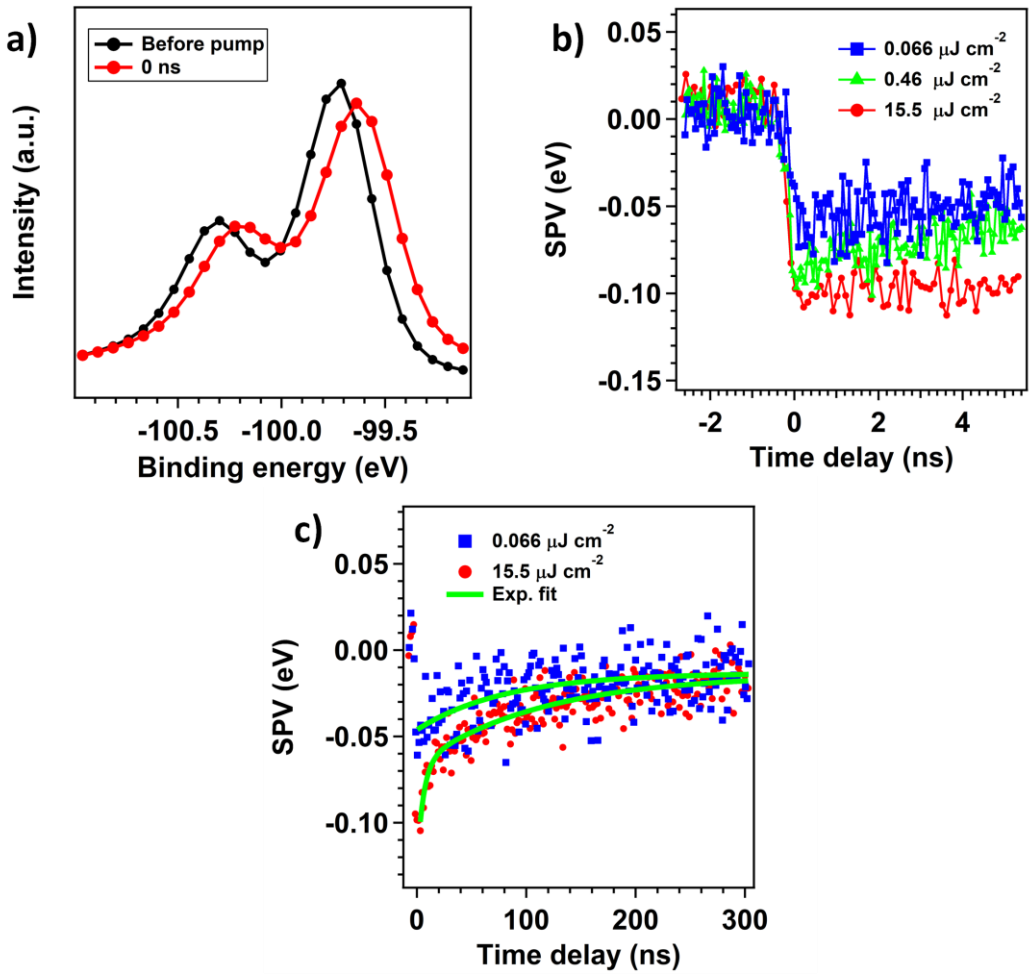

Figure 4.10 a) *SiO_2/n-Si(100) Si2p core level shift after the 15.5 μJ cm^{-2} pump pulse (λ=343 nm) by using hv=400 eV of probe photon energy; decay curves of the $Si2p_{3/2}$ shift by using different pump fluencies* **b)** *within 5 ns and* **c)** *300 ns time delays.*

Sample	Fluence (μJ cm^{-2}) λ=343 nm			
	0.066	0.46	15.5	111
SiO2/p-Si	τ= 88 ns	τ= 103 ns	τ_1= 5.9 ns τ_2= 112 ns	-
SiO2/n-Si	-	-	-	τ= 1.6 ns

Table 4.5 *Summary of the SPV decay time of the SiO_2/p-Si(100) and SiO_2/n-Si(100) samples.*

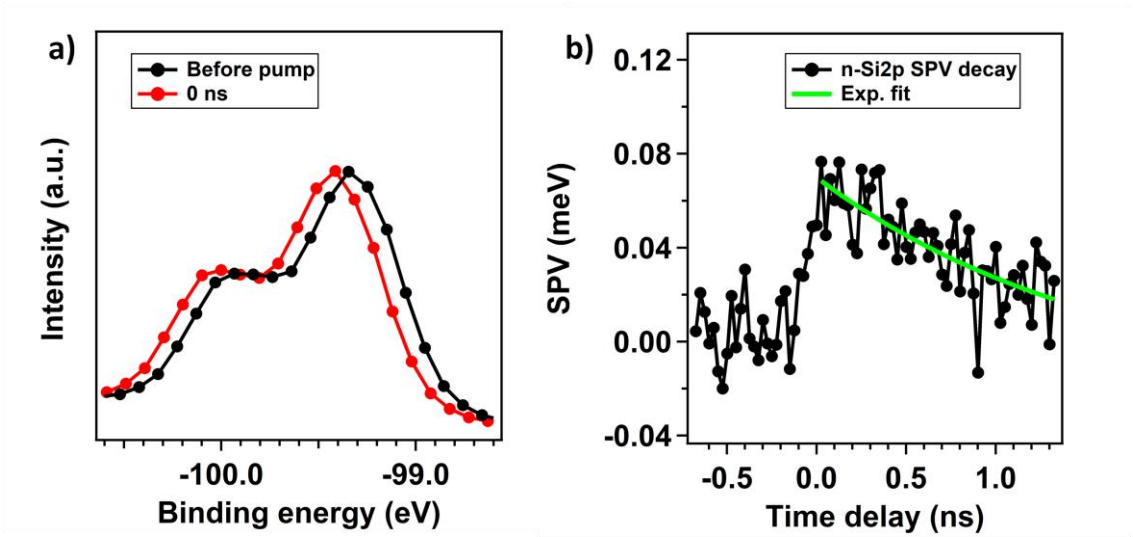

Figure 4.11 a) *SiO_2/n-Si(100) Si2p core level shift after the 111 µJ cm^{-2} pump pulse, hv= 400 eV photon energy and* **b)** *the relative decay curve.*

The simulation of the relaxation dynamics for the p- and n- doped SiO_2/Si(100) samples at different pump fluences are reported in Figure 4.12. The parameters used in the simulations are summarised in Table 4.6. Depending on the model, different parameters are required to fit the SPV decay curves. In *model 1*, for a fixed temperature (298 K), the ideality factor (η) and the "dark" carrier lifetime (τ_D) are the two variable parameters. In *model 2*, η and the degree of band bending (V_{BB}) were the most important parameters in modelling the experimental data. However, several additional parameters characteristic of the sample were required, such as the dopant concentration, and the surface velocity recombination (S_{RV}). Accordingly, the *model 2* should provide more insight to address the origin of the differences in the SPV relaxation dynamics mentioned above for similar samples. Both models accurately fit the SPV decay curves in case of low fluences (Figures 4.12a and b). From the *model 1* were estimated τ_D= 0.43 µs and η= 0.8. A similar η value (0.9) is obtained by the *model 2*. As previously mentioned, in *model 2* the degree of band bending, calculated from the Si2p core level (370 meV), highly determines the accuracy of the SPV relaxation dynamic simulation. In this regard, two different sets of parameters accurately reproduce the experimental decay curve (Figure 4.12b). The dashed red curve (set 2) is the simulation by using the experimental value of the band bending (370 meV). However, as reported in Table 4.6, in this case it is necessary to assume a high value of surface recombination velocity of $5x10^6$ cm s^{-1}. Such a value is reported for the bare silicon, which is not the case[33]. The formation of an oxide layer over the silicon surface leads to covalent Si-O bonds, drastically reducing the surface dangling bonds (which act as recombination centres)[33,36].

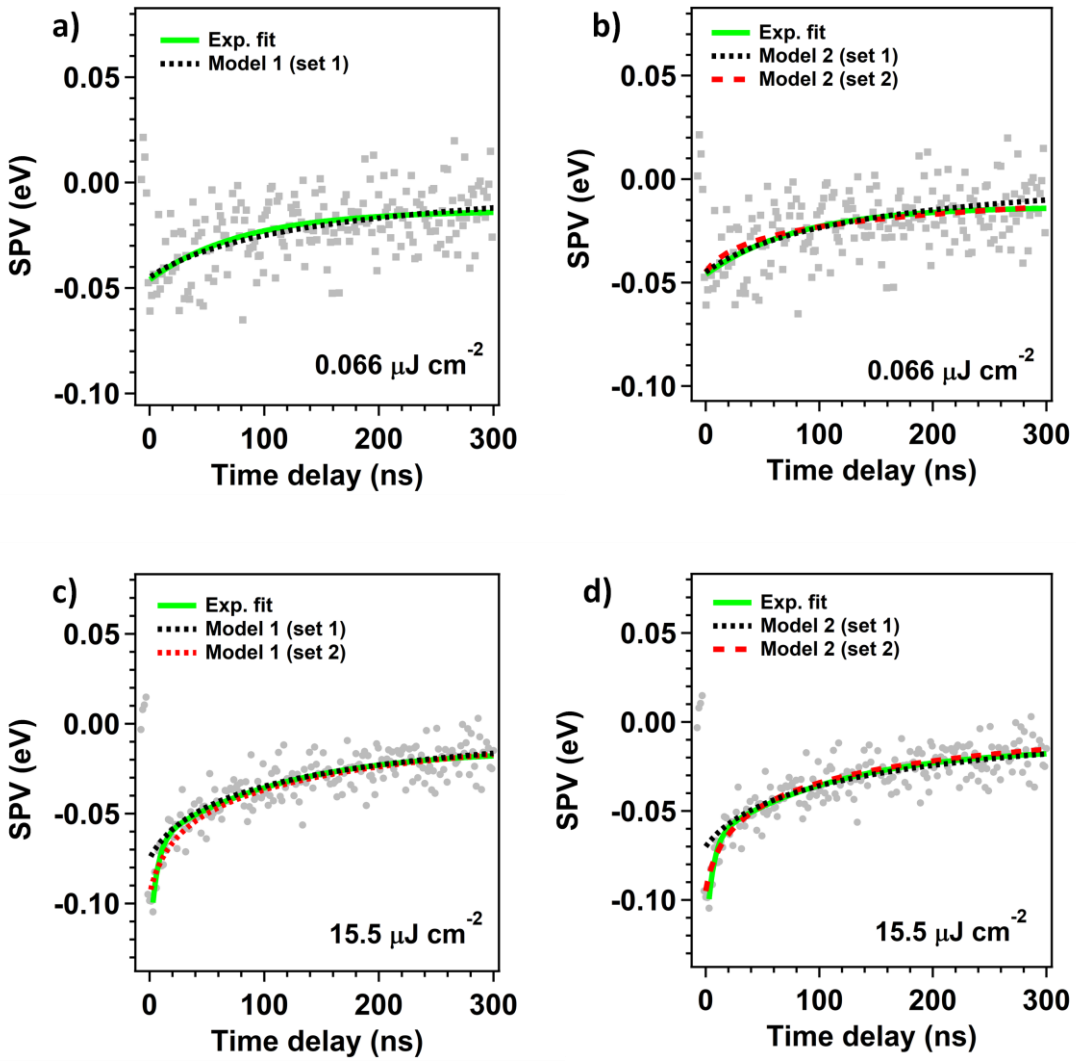

Figure 4.12 *LEINEC simulations of the SiO_2/p-Si(100) SPV decay curves at different pump fluencies by using* **a) c)** *the model 1 and* **b) d)** *the model 2. Set 1 and set 2 are different set of parameters used for a given model to simulate the experimental decay curves. Details on the set of parameters are reported in Table 4.6.*

Fluence ($\mu J\ cm^{-2}$)	Model 1			Model 2			
	SPV (meV)	η	τ_D (μs)	SPV (meV)	η	VBB (meV)	S_{RV} ($cm\ s^{-1}$)
0.066 (set 1)	46	0.8	0.43	46	0.9	95	700
0.066 (set 2)	-	-	-	46	0.4	370	$5x10^6$
15.5 (set 1)	75	0.9	0.47	70	0.9	95	450
15.5 (set 2)	95	0.9	0.47	95	0.85	95	500

Table 4.6 *Summary of the parameters used in the model 1 and the model 2 to reproduce the experimental SiO_2/p-Si(100) SPV decay curves. Set 1 and set 2 are intended as different set of parameters used to simulate the same SPV decay curve.*

As a consequence, in passivated Si sample the surface velocity recombination value is much lower, in the order of 10^2-10^4 cm s^{-1}. The second set of parameters (dashed black curve of Figure 4.12b) uses a much lower V_{BB} of 95 meV (the SPV saturation value observed by using 15.5 μJ cm^{-2} pump fluence) and an S_{RV} of 700 cm s^{-1}. This fact highlights the criticism of those models: multiple sets can graphically reproduce the experimental decay curves. Therefore, particular attention is required to the correct choice of the simulation parameters. They must have physical meaning. In this case, accordingly to the assumptions of the *model 2*, a V_{BB} value different from the experimental one should not be formally correct. However, since the model itself is based on approximations, it may not be able to satisfactory modelling the experimental data, as in this case (an S_{RV} of $5x10^6$ cm s^{-1} is even less realistic). The assumption of a V_{BB} of 95 meV can be partially rationalized considering that, despite the theoretical SPV saturation value should be 370 meV (degree of band bending), we rather observe the achievement of the saturation at 95 meV. In other words, we tentatively assume as a potential barrier the SPV saturation value instead of the effective one. The LEINEC simulations for high pump fluence (15.5 μJ cm^{-2}) are shown in Figures 4.12c and d. Two different sets of parameters are used to fit the SPV decay curve also in this case. Using similar η, τ_D and S_{RV} values to the low fluence case, the decay curves are reproduced (Table 4.6). However, in both models, the shape of the initial part of the fit does not exactly match the experimental curve. A Slightly deviation is observed. Also in this case, in the *model 2* was necessary to assume a potential barrier equal to the SPV saturation rather than the experimental value. The LEINEC simulations of the SiO_2/n-Si SPV decay curve are shown in Figure 4.13. Table 4.7 summarizes the parameters used. A slight deviation of the simulation to the experimental curve is observed for both models. Moreover, in both cases, the parameters used are questionable. From *model 1* is obtained η= 15 and τ_D= 1 ns. High values of η (>10) are reported in the literature for SiO_2/Si and other semiconductor systems[11,14,21]. However, it is a strong deviation from the ideal range of 0.5-2. The decrease of τ_D with increasing doping is consistent with the established carrier lifetime dependence on the resistivity in Si[37]. However, an τ_D of 1 ns is anyway surprisingly low: three orders of magnitude lower than the SiO_2/p-Si(100) system and reported values for similar SiO_2/n-Si samples[14] (hundreds of ns).

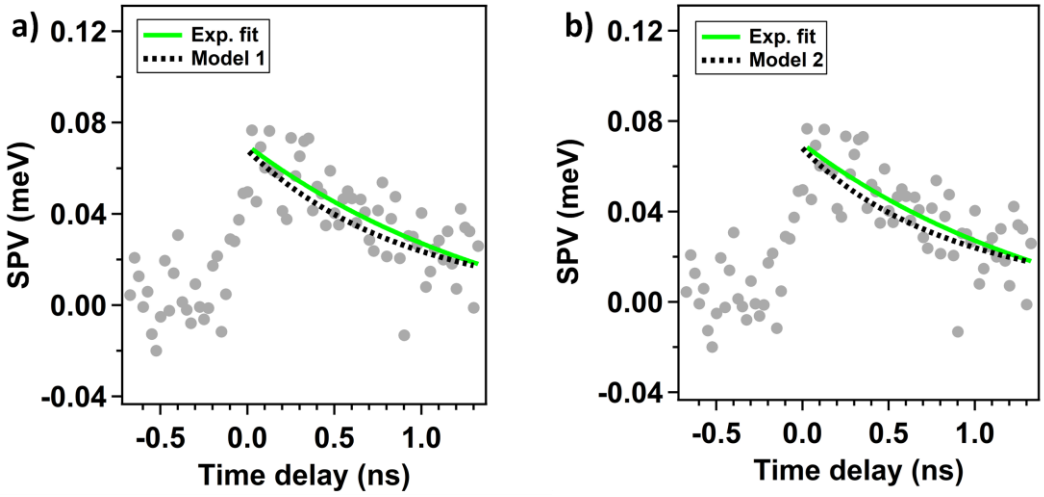

Figure 4.13 *LEINEC simulations of the SiO_2/n-Si(100) SPV decay curve by using* **a)** *the model 1 and* **b)** *the model 2.*

Fluence ($\mu J\ cm^{-2}$)	Model 1			Model 2			
	SPV (meV)	η	τ_D (ns)	SPV (meV)	η	VBB (meV)	S_{RV} ($cm\ s^{-1}$)
111	68	15	1	68	5	68	$2.7x10^3$

Table 4.7 *Summary of the parameters used in the model 1 and the model 2 to reproduce the experimental SiO_2/n-Si(100) SPV decay curve.*

On the other hand, by the *model 2* more reasonable values are estimated; η= 5 and SRV= $2.7x10^3$ cm s^{-1}. The SRV value, despite the increase to that calculated in the SiO_2/p-Si (about 500 cm s^{-1}), still ranges in the values reported in the literature (10^2-$3x10^4$ cm s^{-1}). Such an increase can be rationalized by considering the higher dopant concentration: when the depletion region is thin the charges can tunnel through the barrier and the recombination efficiency increase[22-24]. However, it is not possible to safely exclude that the Si2p peak shift is due to a different dynamical process induced by the high fluence of the pump. The relaxation dynamic occurs in a time domain highly similar to the initial fast relaxation observed before in the SiO_2/p-Si system (τ_1= 5.9 ns).

Previous studies show a strong correlation between the SPV relaxation dynamics and the pump fluence[14,17,20]. When the laser fluence exceeds a certain threshold (depending on the sample) the SPV effect saturates. It is shown that by using laser fluence above the saturation, a modification in the shape of the curves and longer decay time are observed[14]. As a consequence, the decay curves cannot be approximated by the thermionic model. In this case, it is assumed that the thermionic de-excitation process is not efficient enough to relax the total amount of photo-generated charges. Long et al.[20] show that, at high fluence, bulk recombination processes become dominant (not considered in the models).

Nevertheless, in the SiO_2/p-Si(100) SPV relaxation dynamic it is not observed a longer decay time by using high fluencies, and the shape of the decay curve differs only in the first

part (tens of ns). After 100 ns the low and high pump fluence decay curves match, showing identical relaxation dynamics for long time delays. For this reason, a further simulation was performed assuming a lower SPV saturation value (about 70 meV). This assumption equals considering the fast relaxation dynamics of a few ns as a different dynamical process to the SPV. The corresponding simulation should reproduce only the SPV relaxation dynamics. The so-obtained curves still accurately fit the experimental data (without considering the initial fast relaxation). Noteworthy, the fits cross the previous simulation (dashed red curves) after tens of ns, a time comparable to the complete relaxation of the fast dynamical process. Accordingly, two scenarios are possible. The experimental decay curve is due to the contribution of two different relaxation dynamics, in which the "real" SPV magnitude is about 70 meV and an additional process leads to the further 20-25 meV shift. On the other hand, it is well established that high fluencies lead to more complex SPV relaxation dynamics not correctly evaluable by the thermoionic model. A more systematic characterization is required to clarify this point.

Ref.	Type	Doping (cm^{-3})	Fluence ($\mu J\ cm^{-2}$)	Oxide layer (nm)	|SPV| (meV)	Decay time	η	τ_D (μs)
This study	p	$8x10^{14}$	15.5	2	95	100 ns	0.9	0.47
5	p	10^{15}-10^{16}*	15	1.5	300	400 ns	1.3	12
17	p	10^{15}-10^{16}*	0.7	1.5	150	40 ns	2	0.7
14	p	$7.5x10^{14}$	0.37	-	120	1-10 μs	5	2.5
This study	n	$1.6x10^{19}$	111	2	68	1.6 ns	15	10^{-3}
14	n	$4x10^{19}$	60	-	50	100 ns	3	0.1

Table 4.7 *Summary of the parameters used in literature and in this study to simulate the SPV decay curves of p- and n-doped SiO_2/Si systems. *values not reported from the literature, but estimated by LEINEC (section 4.3).*

Finally, the comparison between the results of this study and the literature[5,14,17] is discussed in the following. Table 4.7 summarises the sample properties and simulation parameters used in this work and the literature. The SPV relaxation dynamics of literature were modelled by the same model above discussed, namely model 1. For this reason, the model 2 results are not reported. In refs. 5 and 17 the dopant concentration is not reported. However, in chapter 4.3 a reasonable estimation has been provided by LEINEC simulations (10^{15}-10^{16} cm^{-3}). Similarly, in ref. 14 the oxide layer thickness is not discussed. However, to grow the oxide over-layer a similar thermal procedure was used. Comparable oxide thicknesses of a few nm can reasonably be assumed. Considering first the SiO_2/p-Si system, different SPV magnitude and relaxation dynamics are reported for highly similar systems. In this study and ref. 14 are observed SPV saturation values of about 100 meV

(using comparable pump fluences). On the contrary, in ref. 5 by using a comparable pump fluence, to this study and ref. 14, a shift of 300 meV is observed. They report a dependence of the SPV magnitude on the oxide layer thickness. With lower oxide thickness, the SPV magnitude decreases. Accordingly, small differences in the oxide layer thickness (which are an estimation) may justify the different SPV magnitude. However, it is difficult to address the strong difference between the SPV relaxation dynamics in the three cases: 100 ns in this study (SPV of 95 meV), 400 ns (SPV of 300 meV) in ref. 5 and 1-10 µs (SPV of 120 meV) in ref. 14. According to the theory, a higher SPV magnitude would require a longer relaxation dynamic. On the contrary, the 300 meV SPV relaxation dynamic in ref. 5 is faster than the 120 meV SPV relaxation dynamic in ref. 14. The same authors of ref. 5 report further SPV characterization of the same SiO_2/p-Si sample as a function of the photon fluence in ref. 17. Using lower pump fluence (than that used in ref. 5) as expected they observe a lower SPV shift of 150 meV and a faster relaxation dynamic (40 ns). However, in modelling the SPV relaxation dynamic they assume a lower τ_D (0.7 µs) to the high flux case (τ_D= 12 µs). This is in contradiction with the concept of the thermoionic process: as the SPV decrease, the band bending at the surface is lowered. This means that the free charges to recombine via thermoionic emission (restoring the equilibrium) have to overcome a higher potential barrier and the carrier lifetime is enhanced (higher τ_D). Furthermore, they also use a higher η value (to the high flux case), in contrast to the observation of ref. 14: increasing η values were required in the simulation for increasing fluences.

Similarly, the comparison between similar SiO_2/n-Si systems in this work and ref. 14 highlights differences, in the SPV relaxation dynamics, difficult explainable. By using comparable pump fluencies on samples with highly similar dopant concentrations, comparable SPV shifts (about 50-60 meV) are observed. Nevertheless, the respective relaxation dynamics evolve in different time domains: 1 ns and hundreds of ns. In modelling, completely different η and τ_D values are required.

This final discussion has the aim to stress the limitations to overcome in the actual models. The "versatility" of η may lead to use it as a correction factor. Despite the efficiency of the models in reproducing the experimental SPV relaxation dynamic, discrepancies between different studies are present. In similar samples, pronounced differences are observed in the SPV dynamics and different parameters are used in modelling. Better parameterization of the system physical properties has to be included in the presently available models to correctly address the origin of the differences in SPV dynamics in different systems.

4.4.1 The CuPc/SiO_2/p-Si(100) heterojunction

The characterization of the SPV influence in organic/inorganic heterojunctions has been performed on a CuPc/SiO_2/p-Si system. CuPc thin films of 0.7 nm and 2.2 nm nominal thicknesses were grown on the SiO_2/p-Si sample discussed in the previous section. Figure 4.14 shows the Si2p, C1s and N1s core levels of the bare substrate and at the two different CuPc film thicknesses. The presence of C before the deposition is

due to the normal presence of weak C contaminations also in UHV (after CuPc deposition the C1s peak shape differs). After the deposition of a 2.2 nm CuPc film the Si2p peak intensity is low but still observable.

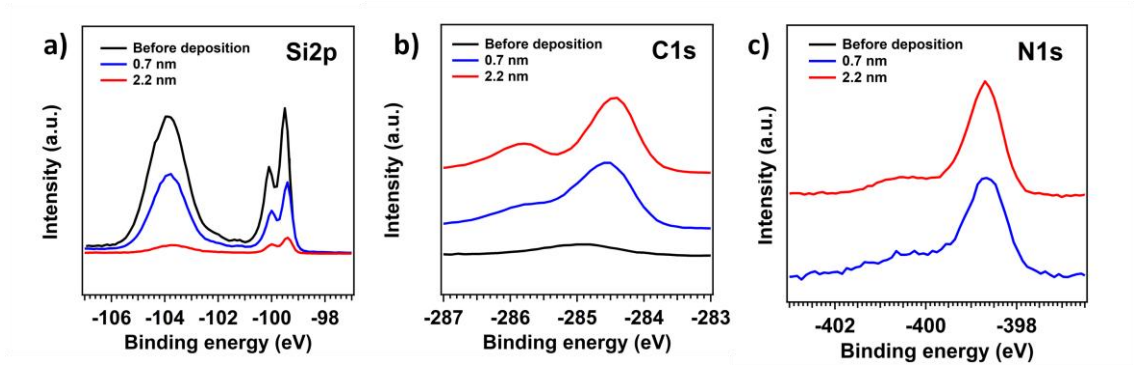

Figure 4.14 a) *Si2p,* **b)** *C1s and* **c)** *N1s core level of the CuPc/SiO_2/p-Si sample at different film thicknesses.*

This is an ideal condition to study both the SPV dynamics of the CuPc and Si and how the formation of an interface influences the relaxation dynamics. The TR-PES Si2p, C1s and N1s core levels before the pump pulse (λ=343 nm) and at t=0 for the 0.7 nm and 2.2 nm CuPc films, and their relative decay curves are shown in Figure 4.15. Both CuPc core levels show an energy shift toward lower binding energy, as in p-type semiconductors. Noteworthy, the C1s and N1s peak shifts magnitude equal that of the Si2p. Furthermore, their relaxation dynamics are identical within 7 ns and no differences are observed in the Si2p SPV decay curve before and after deposition. Accordingly, it is assumed that all relaxation dynamics evolve in the range of hundreds of ns, as in the bare SiO_2/p-Si case discussed in the previous section. Several studies are reported in the literature about the CuPc excited state dynamics[38-41], showing relaxation dynamics from hundreds of fs to hundreds of ps, i.e. processes much faster than the relaxation dynamics observed in the present work. The only exception concerns the decay of CuPc triplet excited states whose lifetime is reported in the 5-8 ns time range[38]. However, this value is still much faster than our dynamics, and the assumption of a 100 meV rigid shift of all CuPc core levels due to the rearrangement of the electronic configuration from singlet to triplet states is questionable (the C2p and N2p frontier orbital would be mostly affected rather than the relative core levels).

SPV spectroscopy performed by Kelvin probe force microscopy points out changes in the surface potential of CuPc/Si(100) and CuPc/ITO films with magnitude and relaxation dynamics comparable to our case[42,43]. Accordingly, we assign the C1s and N1s peak shifts to the SPV effect. The identical SPV magnitude and relaxation dynamics of the CuPc and the SiO_2/p-Si(100) substrate suggest a direct relationship between the two processes. Rationalizing the energy level alignment at the interface in organic semiconductors by using the inorganic band bending theory is not completely correct. Several differences are present between the two types of systems. The molecular ordering, the presence of molecular dipole and the different types of the carrier transport mechanism, among others,

are additional factors to consider to correctly modelling the SPV effect in organic heterojunctions[10].

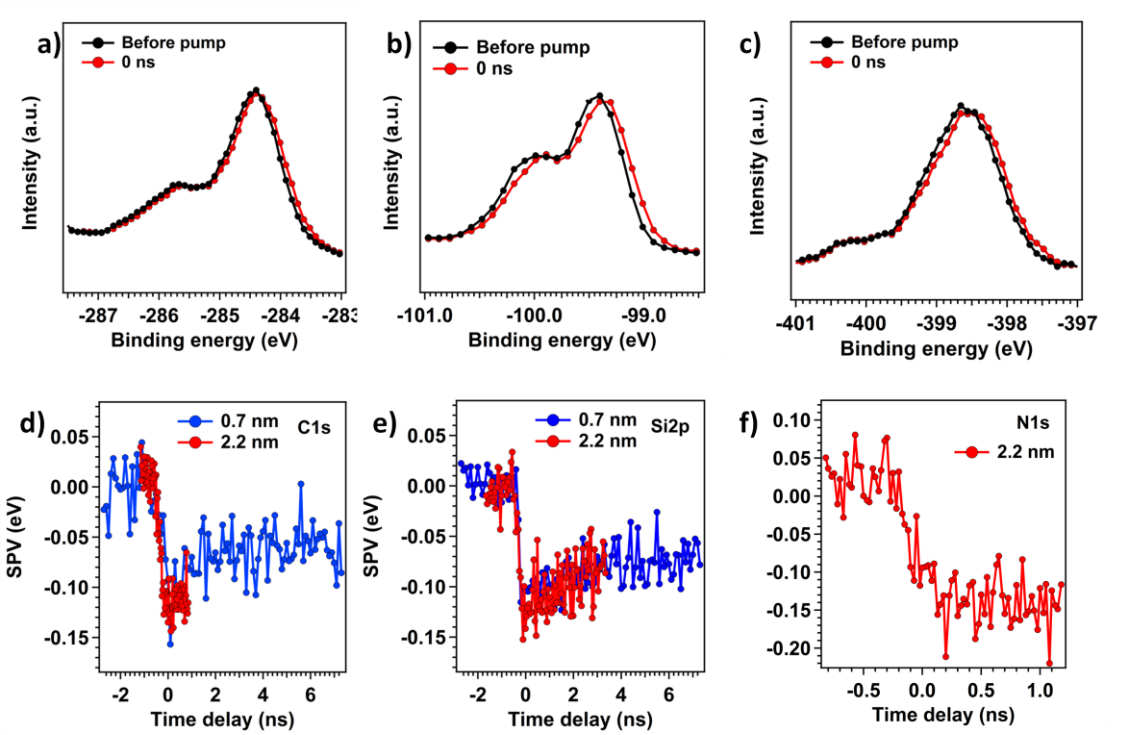

Figure 4.15 a) *C1s,* **b)** *Si2p and* **c)** *N1s core level of the CuPc/SiO_2/p-Si sample before and after pump excitation, and* **d) e) f)** *the relative decay curves.*

However, several studies report similarities in the behaviour of organic semiconductors to the inorganic when forming interface systems[10,44-46]. Gorgoi et al.[46] by combined PES-IPES measurements demonstrated the formation of band bending at the CuPc/H-Si(111) interface. They observed the saturation of the HOMO and LUMO shift (0.4 eV) after depositing 15 nm thickness CuPc film. However, in CuPc films thinner than 3 nm no band bending is detected resulting (no shift of the HOMO and the LUMO were observed). Due to the low film thickness, at the CuPc interface, it is not possible to distribute the excess charges induced by the equilibration of the energy levels (according to the inorganic model) over the required SCR width. Accordingly, considering the CuPc film thickness of 2.2 nm, band bending should not be present at the CuPc interface in this study. Nevertheless, the experimental data suggest a strong correlation between the observed CuPc relaxation dynamics and the SPV effect. After equilibration at the SiO_2/Si interface, the Si and the SiO_2 are negatively and positively charged, respectively. Since the SiO_2 layer is extremely thin (2 nm), on the other side of the oxide layer, the CuPc/SiO_2 interface, the excess of positive charge should not be effectively screened, influencing the CuPc layer charge distribution. In other words, we tentatively assume that to counterbalance the excess of positive charge, at the SiO_2 surface that faces the organic film, negative charging of the CuPc layers may be induced. As a consequence, the CuPc core levels shift and their relaxation dynamics would directly reflect the "reorganization" of the carriers induced by

the SPV effect in the SiO_2/p-Si(100) substrate, leading to identical relaxation dynamics. This assumption may be an oversimplification, nevertheless, this preliminary study provided useful insight about the SPV dynamics in organic heterojunctions. To fully understand their dynamics a more systematic approach is necessary. A detailed characterization of the formation of the CuPc band bending as a function of the increasing film thickness and relative SPV dynamics, as well as TR-PES measurements of CuPc thin films grown on Si substrate with a thicker SiO_2 layer (enough to screen the SiO_2/Si interface influence), will be performed in the next future.

References:

[1] M. A. Reshchikov, M. Foussekis, and A. A. Baski. Surface photovoltage in undoped n -type GaN. *Journal of Applied Physics* **2010**, 107, 113535.

[2] M. Foussekis, J. D. McNamara, A. A. Baski, and M. A. Reshchikov. Temperature-dependent Kelvin probe measurements of band bending in p-type GaN. *Applied Physics Letters* **2012**, 101, 082104.

[3] M. H. Hecht. Time dependence of photovoltaic shifts in photoelectron spectroscopy of semiconductors. *Phys. Rev. B* **1991**, 43, 12102–12105.

[4] M. Alonso, R. Cimino, and K. Horn. Surface Photovoltage Effects in Photoemission from Metal-GaP(110) Interfaces: Importance for Band-Bending Evaluation. *PRL* **1990**, 64, 16.

[5] W. Widdra, D. Bröcker, T. Gießel, I. V. Hertel, W. Krüger, A. Liero, F. Noack, V. Petrov, D. Pop, P. M. Schmidt, R. Weber, I. Will, and B. Winter. Time-resolved core level photoemission: surface photovoltage dynamics of the SiO2/Si(100) interface. *Surface Science* **2003**, 543, 87–94.

[6] B. Adamowicz, M. L. Grilli, M. Pedio, C. Ottaviani, A. Campo, M. Capozi, C. Quaresima, and P. Perfetti. Inverse Photoemission and Kelvin Probe Studies of the Au/GaP(110). *Interface Vacuum* **1995**, 46, 509.

[7] S. M. Sze, and Kwok K. Ng. Physics of Semiconductor Devices. John Wiley & Sons, Inc., **2007.**

[8] T. Dittrich, and S. Fengler. *Surface Photovoltage Analysis of Photoactive Material*. World Scientific, **2020**.

[9] Z. Zhang, and J. T. Yates, Jr. Band Bending in Semiconductors: Chemical and Physical Consequences at Surfaces and Interfaces. *Chem. Rev.* **2012**, 112, 5520−5551.

[10] H. Ishii, N. Hayashi, E. Ito, Y. Washizu, K. Sugi, Y. Kimura, M. Niwano, Y. Ouchi, and K. Seki. Kelvin probe study of band bending at organic semiconductor/metal interfaces: examination of Fermi level alignment. *Phys. Stat. Sol. (a)* **2004**, 201, 6, 1075–1094.

[11] M. Ogawa, S. Yamamoto, K. Fujikawa, R. Hobara, R. Yukawa, S. Yamamoto, S. Kitagawa, D. Pierucci, M. G. Silly, C.-H. Lin, R. Y. Liu, H. Daimon, F. Sirotti, S.-J. Tang, and I. Matsuda. Relaxations of the surface photovoltage effect on the atomically controlled semiconductor surfaces studied by time-resolved photoemission spectroscopy. *Phys. Rev. B* **2013**, 88, 165313.

[12] M. Cantoni, R. Bertacco, A. Brambilla, F. Ciccacci . Photon- and electron-induced surface voltage in electron spectroscopies on ZnSe(001). *Journal of Electron Spectroscopy and Related Phenomena* **2009**, 173, 84–87.

[13] M. Cantoni, R. Bertacco, A. Brambilla, M. Finazzi, L. Duò, F. Ciccacci, A. Verdini, L. Floreano, A. Morgante, M. Passoni, C. S. Casari, and A. Li Bassi. Fe nanoparticles on ZnSe: Reversible temperature dependence of the surface barrier potential. *PRB* **2012**, 85, 155456.

[14] D. Pierucci, M. G. Silly, H.Tissot, P. Hollander, F. Sirotti, and F. Rochet. Surface photovoltage dynamics at passivated silicon surfaces: influence of substrate doping and surface termination. *Faraday Discussions***, 2022.**

[15] Y. Yao, X. Sun, B. Ding, D.-L. Li, X. Hou, and C.-Q. Wu. A combined theoretical and experimental investigation on the transient photovoltage in organic photovoltaic cells. *Appl. Phys. Lett.* **2010**, 96, 203306.

[16] H. Lim, H. Kwon, S. K. Kim, and J. W. Kim. Delayed Triplet-State Formation through Hybrid Charge Transfer Exciton at Copper Phthalocyanine/GaAs Heterojunction. *J. Phys. Chem. Lett.* **2017**, 8, 4763−4768.

[17] D. Brocker, T. Gießel, and W. Widdra. Charge carrier dynamics at the SiO2/Si(100) surface: a time-resolved photoemission study with combined laser and synchrotron radiation. *Chem. Phys.* **2004**, 299, 247–251.

[18] R. J. Hamers, and D. G. Cahill. Ultrafast time resolution in scanned probe microscopies: Surface photovoltage on Si(111)–(7×7). *J. Vac. Sci. Technol. B* **1991**, 9, 514–518.

[19] R. J. Hamers, and K. Markert. Atomically resolved carrier recombination at Si(111)-7×7 surfaces. *Phys. Rev. Lett.* **1990**, 64, 1051–1054.

[20] J. P. Long, H. R. Sadeghi, J. C. Rife and M. N. Kabler. Surface space-charge dynamics and surface recombination on silicon (111) surfaces measured with combined laser and synchrotron radiation. *Phys. Rev. Lett.* **1990**, 64, 1150–1161.

[21] A. Pietzsch, A. Föhlisch, F. Hennies, S. Vijayalakshmi, and W. Wurth. Interface photovoltage dynamics at the buried BaF_2/Si interface: Time resolved laser-pump/synchrotron-probe photoemission. *Appl. Phys. A* **2007**, 88, 587–592.

[22] M. H. Hecht. Role of photocurrent in low-temperature photoemission studies of Schottky-barrier formation *Phys. Rev. B* **1990**, 41, 11, 7918–7922.

[23] A. Bauer, M. Prietsch, S. Molodtsov, C. Laubschat, and G. Kaindl. Systematic study of the surface photovoltaic effect in photoemission. *Phys. Rev. B* **1991**, 44, 4402–4005.

[24] G. A. Mulhollan, A. V. Subashiev, J. E. Clendenin, E. L. Garwin, R. E. Kirby, and T. Maruyama. Photovoltage Effects in Photoemission from Thin GaAs Layers. *Physics Letters A* **2001**, 282, 309–318.

[25] L. Kronik, and Y. Shapira. Surface photovoltage phenomena: theory, experiment, and applications. *Surf. Sci. Rep.* **1999**, 37, 1.

[26] B. I. Bednyi, and N. V. Baidus. Effect of recombination in the space charge region on the illuminance characteristics of the surface photo-emf of GaAs and InP. *Semiconductors* **1993**, 27, 7, 620-622.

[27] M. Kusaka, N. Hiraoka, M. Hirai, and S. Okazaki. Electrical properties of p-type GaP Schottky barrier under stress. *Surface Science* **1980**, 91, 264-270.

[28] K. E. Miyano, R. Cao, T. Kendelewicz, A. K. Wahi, I. Lindau, and W. E. Spicer. Reaction and barrier formation at metal-GaP(110) interfaces. *Phys. Rev. B* **1990**, 41, 2, 1076-1089.

[29] H. Cheng, X.-J- Zhang, and A. G. Milne. Schottky-barrier diodes of MBE-deposited Antimony on n and p Gallium Arsenide. *Solid-State Electronics* **1984**, 27, 12, 1117-1122.

[30] C. J. Spindt, M. Yamada, P. L. Meissner, K. E. Miyano, A. Herrera, W. E. Spicer, and A. J. Arko. Au and Al Schottky barrier formation on GaAs (100) surfaces prepared by thermal desorption of a protective arsenic coating. *Journal of Vacuum Science & Technology B* **1991**, 9, 2090-2094.

[31] J. Tersoff. Schottky Barrier Heights and the Continuum of Gap States. *Phys. Rev. Lett.* **1984**, 52, 465-468.

[32] J. Tersoff. Schottky barriers and semiconductor band structures. *Phys. Rev. B* **1985**, 32, 6968-6971.

[33] S. Rouvimov, B. Kim, T.-C. Jo, and D. K. Schroder. Surface recombination velocity of silicon wafers by photoluminescence. *Appl. Phys. Lett.* **2005**, 86, 112110.

[34] F. J. Himpsel, B. S. Meyerson, F. R. McFeely, J. F. Morar, A. Taleb-Ibrahimi, and J. A.Yarmoff. *Proceedings of Enrico Fermi School on "Photoemission and Adsorption Spectroscopy of Solids and Interfaces with Synchrotron Radiation"*, eds. M. Campana and R. Rosei, Amsterdam, **1992**.

[35] F. J. Himpsel, F. R. McFeely, A. Taleb-Ibrahimi, J. A. Yarmoff, and G. Hollinger. Microscopic structure of the SiO_2/Si interface. *Phys. Rev. B* **1988**, 38, 6084-6096.

[36] E. Yablonovitch, D. L. Allara, C. C. Chang, T. Gmitter, and T. B. Bright. Unusually Low Surface-Recombination Velocity on Silicon and Germanium Surfaces. *Phys. Rev. Letters* **1986**, 57, 2, 249-252.

[37] R. J. Hamers, and D. G. Cahill. Ultrafast time resolution in scanned probe microscopies. *Appl. Phys. Lett.* **1990**, **57**, 2031-2033.

[38] B. W. Caplins, T. K. Mullenbach, R. J. Holmes, and D. A. Blank. Femtosecond to nanosecond excited state dynamics of vapor deposited copper phthalocyanine thin films**.** *Phys. Chem. Chem. Phys.* **2016**, 18, 11454.

[39] M. Lia, W.-H. Lia, Y.-J. Hua, J. Lengb, W.-M. Tianb, C.-Y. Zhaob, J.-X. Liub, R.-R. Cuib, S.-Y. Jinb, C.-H. Chenga, and S.-L. Conga. Influence of the Molecular Stacking Pattern on the Excited State Dynamics of Copper Phthalocyanine Films. Chin. *J. Chem. Phys.* **2021.**

[40] M.-H. Ha-Thi, N. Shafizadeh, L. Poisson, and B. Soep. An Efficient Indirect Mechanism for the Ultrafast Intersystem Crossing in Copper Porphyrins. *J. Phys. Chem. A* **2013**, 117, 8111−8118.

[41] A. Popescu, R. A. Younts, B. Hoffman, T. McAfee, D. B. Dougherty, H. W. Ade, K. Gundogdu, and I. V. Bondarev. Monitoring Charge Separation Processes in Quasi-One-Dimensional Organic Crystalline Structures. *Nano Lett.* **2017**, 17, 6056−6061.

[42] S. Sadewasser, and M. Ch. Lux-Steiner. Local surface photovoltage spectroscopy of Cu-phthalocyanine clusters on different Substrates. *J. Vac. Sci. Technol. B* **2010**, 28, C4D29.

[43] Y. Yao, X. Sun, B. Ding, D.-L. Li, X. Hou, and C.-Q. Wu. A combined theoretical and experimental investigation on the transient photovoltage in organic photovoltaic cells. *Appl. Phys. Lett.* **2010**, 96, 203306.

[44] H. Lim, H. Kwon, S. K. Kim, and J. Won Kim. Delayed Triplet-State Formation through Hybrid Charge Transfer Exciton at Copper Phthalocyanine/GaAs Heterojunction. *J. Phys. Chem. Lett.* **2017**, 8, 4763−4768.

[45] E. Moons, A. Goossens, and T. Savenije. Surface Photovoltage of Porphyrin Layers Using Kelvin Probe Technique. *J. Phys. Chem.* **1997**, 101, 8492-8498.

[46] M. Gorgoi, and D.R.T. Zahn. ''Band bending'' in copper phthalocyanine on hydrogen-passivated Si(111). *Organic Electronics* **2005**, 6, 168–174.

5. The TR-XAS end-station

This chapter describes the new TR-XAS end-station, in which X-ray absorption spectroscopy (XAS) can be performed in a pump-probe fashion by exploiting the pulsed nature of synchrotron radiation. The optical set-up of TR-XAS offers the possibility of variable non-collinear laser – X-ray beam geometry, to tune the relative penetration depths and excitation volumes. In pump-probe spectroscopy the penetration depths must be chosen to optimize the spatial overlap between the beams, maximizing the pump excitation yield and the signal-to-noise ratio (S/N)[1,2]. In solids, the X-ray penetration depth may strongly differ from that of the laser one. For this reason, variable geometry is mandatory to optimize the excitation volumes, making the TR-XAS feasible for large classes of materials. The presented TR-XAS set-up is developed according to the configuration used at the BACH beamline[3,4] (Elettra synchrotron), which provides a time resolution of about 80-100 ps.

5.1 Motivation of a variable geometry

In the TR-XAS experiments performed at branch A of the BACH beamline, the laser beam enters the experimental chamber at a fixed angle of 22° to the X-ray photon beam (Figure 5.1a). The X-ray fluorescence emission is detected by an ultrafast micro-channel plate (MCP) at the angle of 22° in the scattering plane of the sample, introducing the reflectivity induced by the laser in the MCP signal. Moreover, using a fixed experimental geometry condition it is not possible to optimize the laser-X-ray excitation volume (Figure 5.1b). To overcome these constraints, a new TR-XAS end-station with variable mutual geometry between pump, probe and detector has been designed and built.

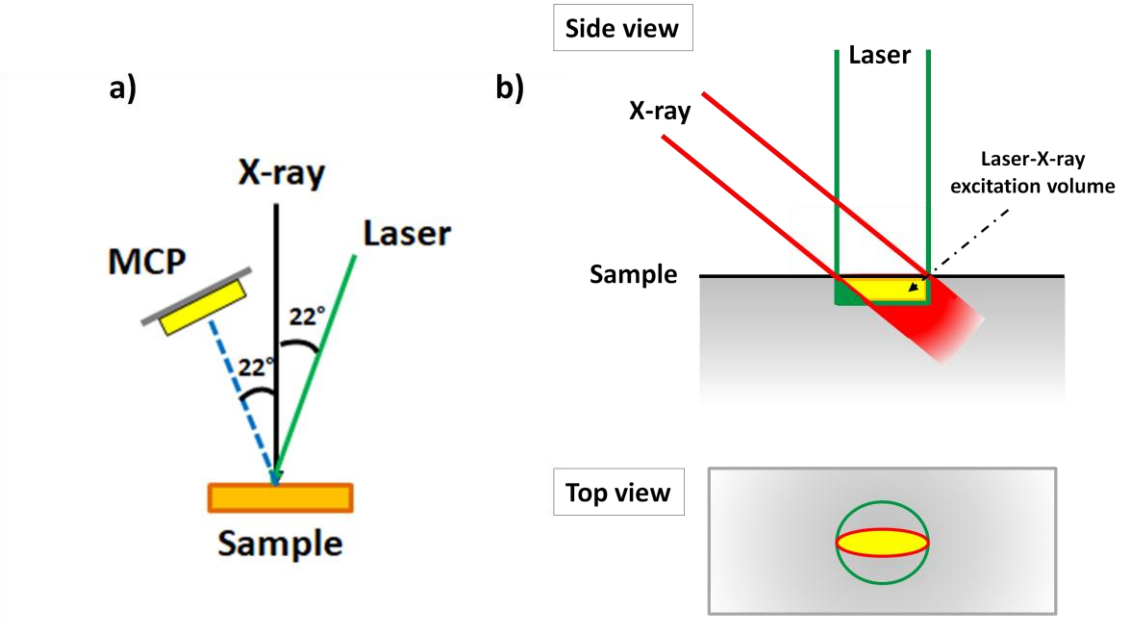

Figure 5.1 a) *TR-XAS experimental setup of the main chamber at BACH;* **b)** *X-ray-laser surface and volume overlap in X-ray-based pump-probe experiments.*

In pump-probe experiments the volume probed should match as closely as possible the volume of the sample excited by the pump pulse. In UV-VIS laser-based pump-probe experiments the wavelengths and the optical properties of the two beams are similar, easily achieving an optimal spatial overlap. On the contrary, by using an X-ray probe the matching of volumes faces the problem created by the fairly low interaction cross-section between the pump and probe beams. In opaque solid samples, the X-ray penetration depth is usually much larger than that of the optical laser, highly depending on the sample orientation to the X-ray. As a consequence, the typical excitation depth of the pump is in the order of 50 nm, while in the X-ray case depending on the edge under study, it may exceed 1 µm. Optimal spatial overlap and homogeneous excitation of probed volume are mandatory requirements to maximize the pump excitation yield and the S/N [1,2]. This experimental condition could be achievable by the new TR-XAS end-station with variable geometry between laser, X-ray and detector. Figure 5.2 shows an example of a simulation of the S/N at different experimental configurations at the Ge L_3 edge (laser pump λ= 400 nm). The optimized S/N is obtained in a non-collinear geometry. Depending on the configuration used the maximization of the S/N is achieved at different sample angles (α).

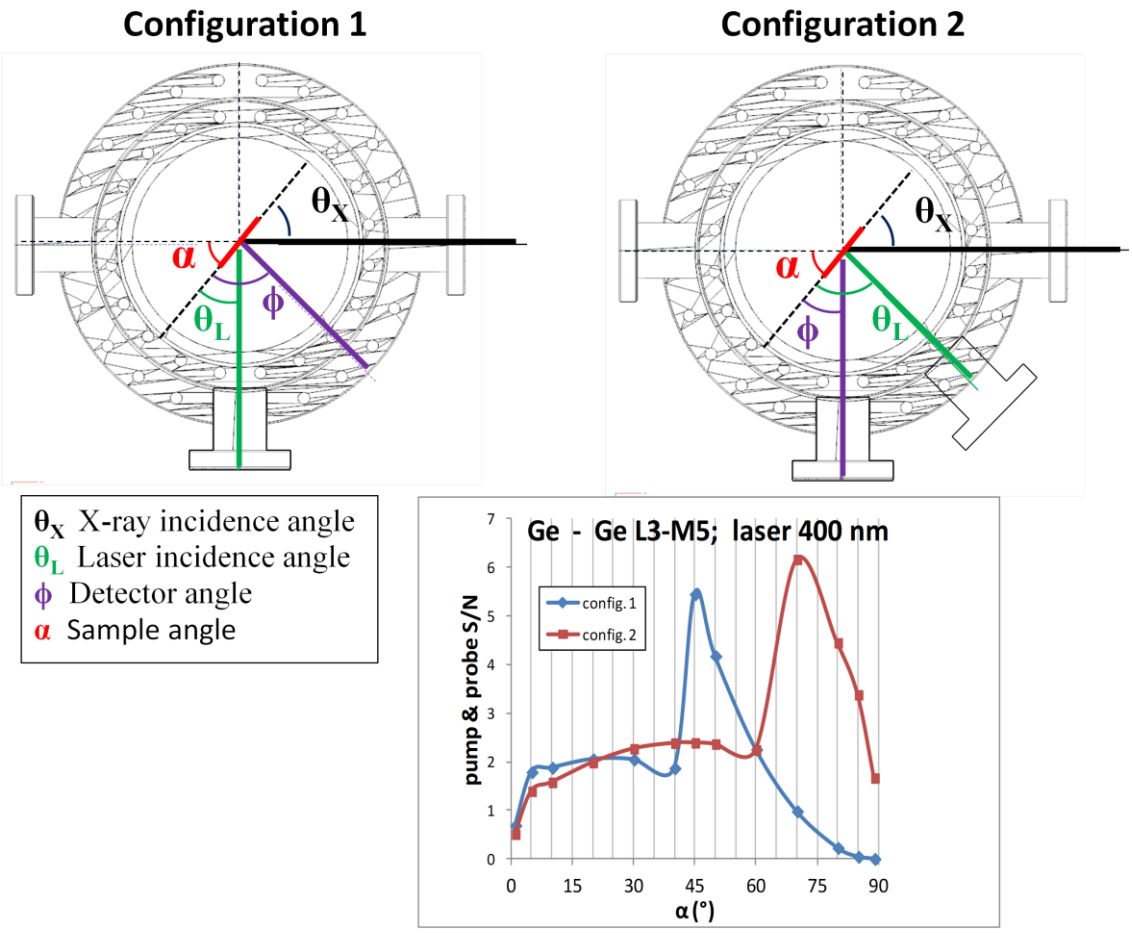

Figure 5.2 *Simulation of the S/N as a function of the sample orientation of the Ge L_3 edge (laser pump λ=400 nm) at two different experimental configurations.*

The evaluation of the S/N at different experimental configurations reported in Figure 5.2 was performed by means of the new T-XRES code. The code has been developed as an auxiliary tool to the TR-XAS chamber to a priori optimize the experimental condition. The code can evaluate the laser-X-ray excitation volume, the detector efficiency (for a given absorption edge), the fluorescence signal in steady-state XAS experiments as well as the S/N in time-resolved mode as a function of the chosen experimental geometry.

5.1.1 The T-XRES code

T-XRES (Time-resolved X-Ray Experiment Simulator) is a code developed as an auxiliary tool to the TR-XAS end-station. T-XRES is intended as a user-friendly calculation tool, meant for reliable and precise numerical simulations of steady-state and time-resolved X-ray measurements. For a given X-ray-laser geometrical configuration, the code evaluates their spatial overlap as well as the resultant excitation volume by considering the effective penetration depth in the material of the two beams. The fluorescence signal in steady-state measurements and the S/N in time-resolved experiments can be evaluated in different ranges of laser, X-rays and detector geometries, making the code a powerful tool to a priori optimize the experimental condition[2]. For a given detection geometry, the static fluorescence signal is given by[2,5]:

$$If = I_0 K \frac{\mu_{abs}(E)}{\sin(\theta)} \frac{\left(1-e^{-Ad}\right)}{A} \qquad (5.1)$$

with:

$$A = \frac{\mu_{tot}(E)}{\sin(\theta)} + \frac{\mu_{tot}(Ef)}{\sin(\varphi)} \qquad (5.2)$$

where I_0 is the incident X-rays flux, K describes the detector characteristics and spectroscopic parameters of the transition due to X-rays absorption, μ_{abs} and μ_{tot} the absorption coefficients at the incident beam energy (E) and at the fluorescence energy (E_f), (θ and ϕ are the respectively incident beam and fluorescence angles to the sample surface)[2,6-8].

The S/N in time-resolved experiments is calculated by the equation[1,2]:

$$\frac{S}{N} = \sqrt{\frac{I_0 K \frac{\mu_{abs}(E)\left(1-e^{-AZ_x}\right)}{\sin(\theta) \quad A}}{\frac{2}{(\Delta * f)^2}}} \qquad (5.3)$$

where A is given by eq. 5.2, Z_x is the X-rays penetration depth and Δ is the relative spectral difference between excited and ground state. The photo-excitation yield, f (or pump ratio), induced by the laser is evaluated using the relation:

$$f = \frac{I_{0L}}{\rho F(\theta) Z(\theta)_L} [1 - R_L(\theta)] \left[1 - e^{-\rho \sigma_{opt} \frac{Z_L}{\cos(\theta_R)}}\right] \qquad (5.4)$$

where I_{0L} is the number of incident laser photons (note that in this case the entry for photon flux becomes the number of incoming photons, not photons s^{-1}), ρ is the sample density, F(θ) is the focal area impinged by the laser, $Z_L(\theta)$ is the laser penetration depth, $R_L(\theta)$ is the sample reflectivity, and σ_{opt} is the optical absorption cross[9] section of the sample (θ is the laser incidence angle to the sample surface).

It is possible to use the code in two different ways: evaluating the number of photons required to have a fixed S/N, or vice versa evaluating the S/N for fixed laser/X-ray fluxes. As graphical output, it is generated a 3D map of the S/N over all the possible laser-Xray geometries. A critical factor for an accurate simulation is the excitation yield. It should be precisely known, but it is rarely measured during X-ray-based time-resolved experiments. It is important to emphasize that, an estimation of the excitation yield from the sample characteristics and the laser pulse parameters is not accurate since scattering and nonlinear absorption contributions are ignored. The relative spectral difference, Δ, is defined as:

$$\Delta = \frac{C_{ex} - C_g}{C_g} \qquad (5.5)$$

where C_{ex} and C_g are the fluorescence counts from the excited and ground state, respectively. A Δ value has to be provided as input to the routine. Usually, it is determined experimentally, however, assuming Δ values of a few percentages is generally a good approximation.

Figure 5.3 reports a few examples of graphical output from T-XRES simulations. Figure 5.3a and b show, respectively, the calculated fluorescence signal in steady-state XAS as a function of the X-ray incidence angle (to the sample surface) and detection angle, and the calculated S/N as a function of the X-ray and laser incidence angles on a Ge sample (Ge L_3 edge, pump 400 nm). The maximum S/N is predicted for X-ray at grazing incidence. As shown in Figure 5.3c this is due to the comparable penetration depths between the two beams (hundreds of nm) when X-rays are grazing on the sample surface. However, one critical aspect of the T-XRES calculations is that the self-absorption effect is not included in the model, for the moment. This effect dramatically affects XAS measurements lineshape when the X-rays incidence angle approaches the grazing incidence condition. Similarly, detection geometries of the fluorescence signal close to the normal emission enhance the self-absorption effect. Optimization of the program including the self-absorption effect as a function of the X-ray and detection geometry is planned. This will be accomplished by using theoretical models proposed in literature[2,10-12] together with

experimental data from XAS systematic studies on selected samples. The T-XRES code is currently in the beta-testing phase.

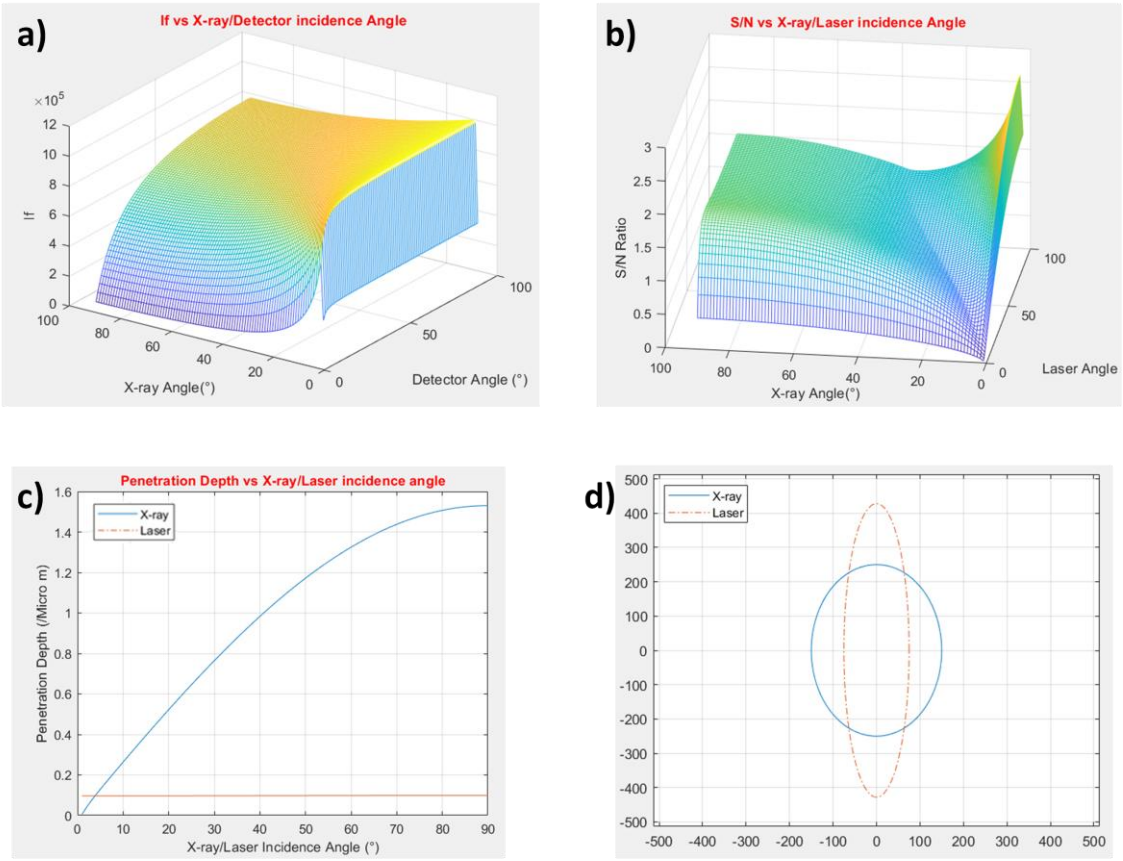

Figure 5.3 *Example of T-XRES simulations of* **a)** *the FY signal in steady state XAS and* **b)** *of the S/N in TR-XAS experiments as a function of the X-ray and laser incidence angles; T-XRES evaluation of the* **c)** *X-ray and laser penetration depths as a function of the incidence angle and of the* **d)** *overlap between the spots of the two beams.*

5.2 The TR-XAS setup

The TR-XAS setup is currently operating in commissioning at the branch B of the BACH beamline at the Elettra synchrotron (Figure 5.4). BACH is designed for light-polarization-dependent experiments in the energy range 35–1600 eV[3,4]. It is based on two elliptical undulators as photon sources optimized in the low (~50–150 eV) and high (~600–1000 eV) energy ranges, and it is characterized by high photon flux, high resolution, and the control of the light polarization. The prefocusing section is based on a Kirkpatrick–Baez system made of two spherical mirrors, allowing the complete decoupling between the horizontal and the vertical focusing. Thanks to this configuration an easier and more precise alignment of the two optical elements is possible. The Padmore monochromator is equipped with three different higher-solution gratings (SG1-3), which together cover the

whole available energy range, and a fourth grating (SG4), with a lower groove density, provides a higher flux in the high-energy range. The first three gratings allow resolving powers of 20000-6000, 20000-6000 and 15000-5000 in the energy ranges 35-200 eV, 200-500 eV and 500-1600 eV respectively. The fourth grating operates in the 300-1600 eV range providing higher flux with reduced resolving power (10000-2000). After the monochromator, the beamline is split into two branches (A and B) with different refocusing properties.

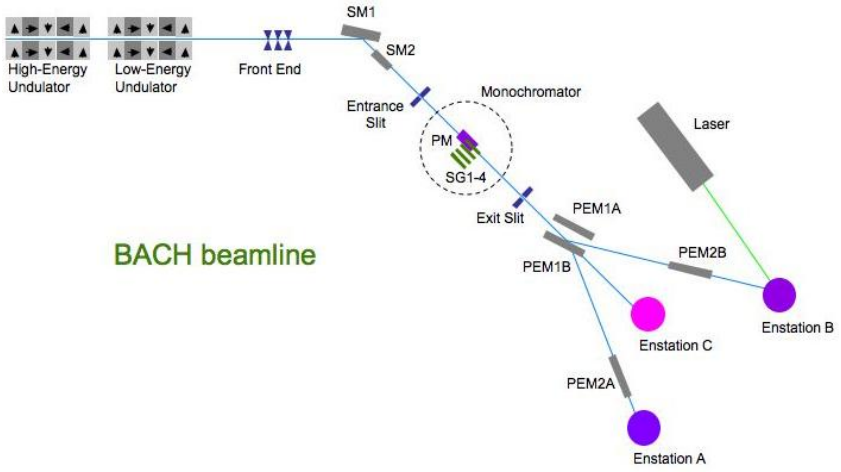

Figure 5.4 *Schematic illustration of the BACH beamline at Elettra synchrotron.*

The refocusing section of branch B is based on two planes of elliptical mirrors (PEM1B and PEM2B). The vertical refocusing mirrors are kept as close as possible to the experimental chambers, to work with a vertical spot size of about 30 μm. The spot size on the sample can be as small as 250x30 μm^2. However, when beam damage effects are critical, the spot size can be increased to 300x300 μm^2. The flux in the experimental chamber ranges between $1.2 \cdot 10^{12}$ photons s^{-1} at 125 eV and $6x10^{10}$ photons s^{-1} between 900 eV and 1250 eV. A complete and detailed description of the beamline layout, the parameters of the various optics, and the theoretical performances of BACH can be found in refs 3 and 4.

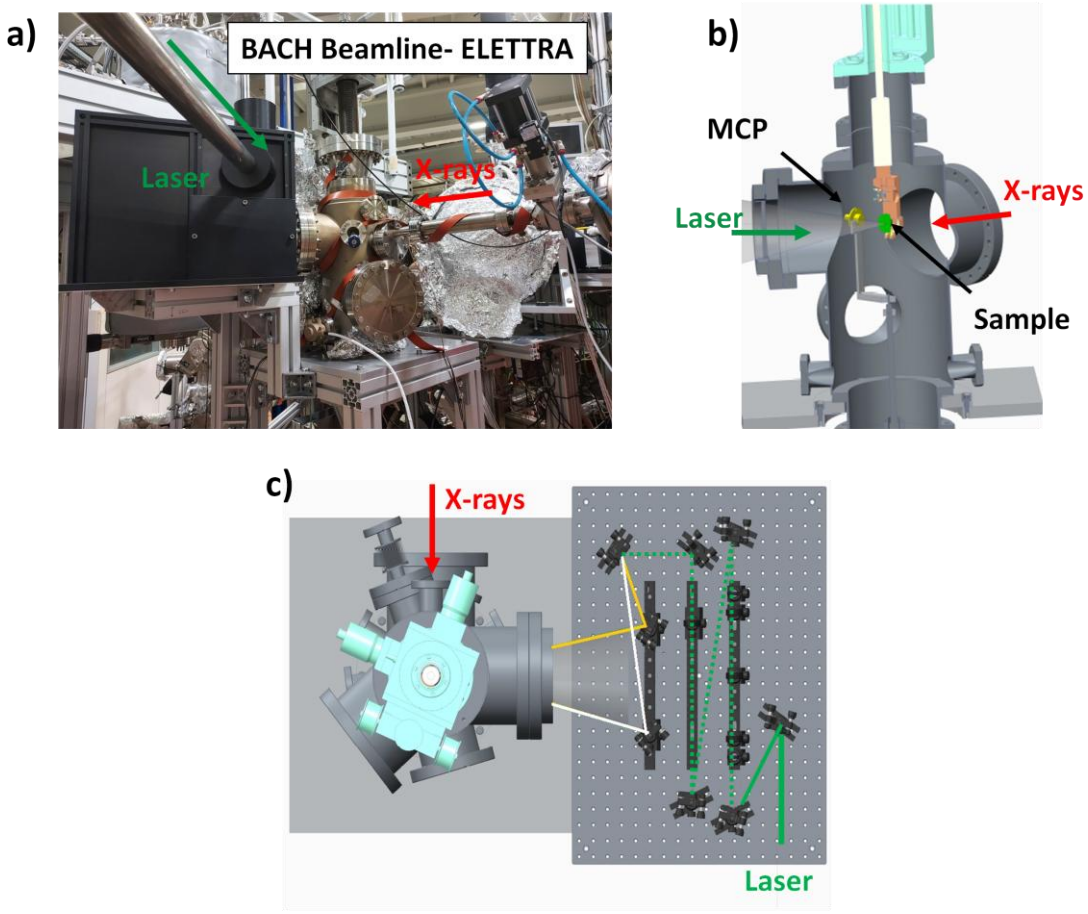

Figure 5.5 a) *Photo of the TR-XAS endstation at the BACH beamline of Elettra; Illustrations of the* **b)** *TR-XAS chamber setup and* **c)** *top view of the laser optical setup, by moving the last mirror the incidence angle of the laser can be varied in a angle corner width of 33°.*

The TR-XAS end-station has been designed to perform high-resolution XAS and time-resolved XAS (TR-XAS) on solid samples. Steady-state XAS can be performed at the same time in total electron (TEY) and fluorescence yield (FY). The X-ray fluorescence emission is detected by an ultrafast micro-channel plate (Hamamatsu F4655-13 MCP15) detector freely rotatable (1° resolution) around the axis chamber. An additional degree of freedom is provided by the motion along the z-axis (height) and the tilt angle. A scheme of the experimental setup is shown in Figure 5.5. The MCP (Figure 5.6) is a detector consisting of millions of very-thin, conductive glass capillaries (4 to 25 μm in diameter) fused and sliced into a thin plate. Each capillary, or channel, works as an independent secondary-electron multiplier to form a two-dimensional electron multiplier.

The MCP is sensitive to a wide range of radiation including UV, VUV, soft X-ray photons and neutrons, offering many advantages over conventional detectors: compactness, good timing properties due to short length, high gain, and excellent pulse height distribution. The Z movement of the detector is necessary for TR-XAS measurement in out-of-plane geometry (away from the scattering plane of the sample) to avoid reflectivity induced by the laser in the MCP signal and reduce self-absorption in the FY signal. The

MCP tilt angle is used to maximize the FY signal in the out-of-plane geometry (Figure 5.6b).

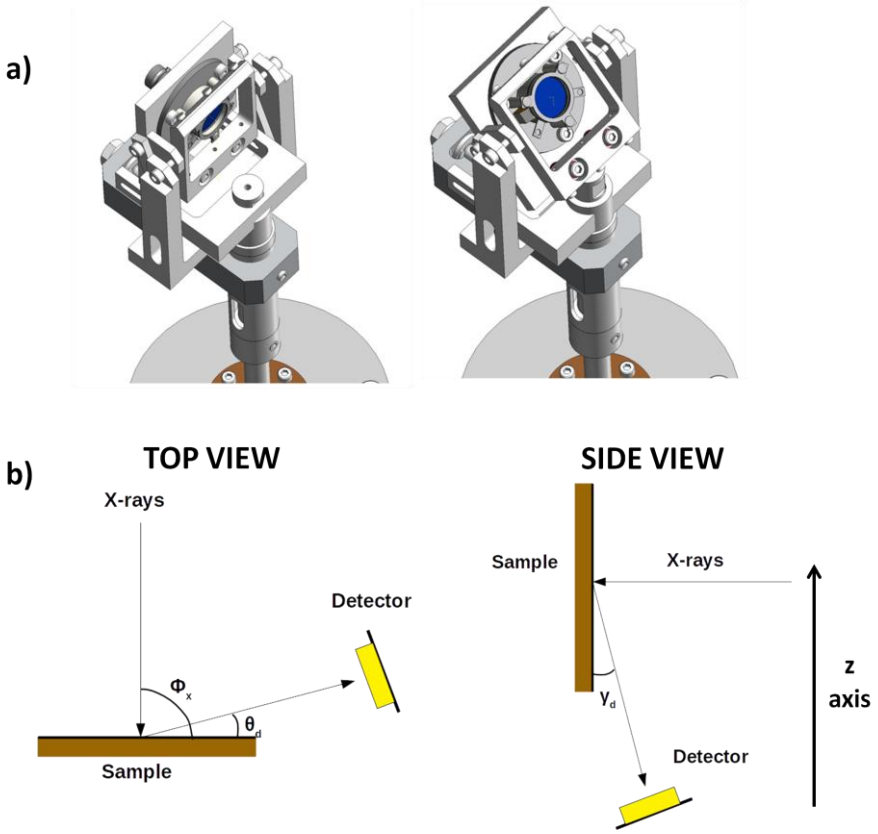

Figure 5.6 a) *Illustration of the MCP for in-plane (left) and out-of-plane (right) detections: the MCP angle can be adjusted between 0° and 45°;* **b)** *detector geometries along the beams incidence plane (top view) and the z axis (side view), where θ_d and γ_d are the detection and MCP tilt angles, respectively.*

The fluorescence emission solid angle and detection solid angle have to match as closely as possible to reduce signal losses due to the detector-sample distance. A variable temperature (100 - 300 K) sample holder is mounted on a 4-axis manipulator. A photodiode is mounted over the sample-holder to measure the incident laser and X-rays flux directly in the experimental chamber. The polar angle of the manipulator can be rotated (2° resolution) to vary the X-ray incidence angle on the sample. The chamber setup, the MCP motion system and the sample-holder were developed in-house. The system operates in ultra-high vacuum (UHV) conditions, with a typical base pressure of 2×10^{-9} mbar. The laser beam enters the experimental chamber through a quartz window with a variable incidence angle on the sample.

The laser optical table is designed to allow an angle corner width of 33° simply moving the last mirror of the laser optical path (Figure 5.5c). Currently, the laser interfaced to this setup is the MIRA Optima 900-F HP (Coherent), a Ti:Sa with a fundamental wavelength of 800 nm. The laser source operates at a repetition rate of 83.3 MHz and delivers ~25 nJ, ~100 fs, (800 nm) laser pulses. The optical system operates without laser amplification,

limiting the power of the pump pulse. This constraint strongly affected TR-XAS experiments during the commissioning. The laser repetition rate can be varied using a pulse picker selecting up to 1/18 of the laser pulses (30% power loss), enabling a wider experimental time window in case of "slow" dynamical processes. Non-linear beta barium borate (BBO) crystal is used for generating the second harmonic (400 nm). The laser is focused on the sample by a fixed 1000 mm focusing lens, while the focus size is adjusted operating on the sample position. An essential feature of the laser system is the module for the synchronization of the oscillator to an external source (i.e. the Elettra storage ring). It is an integrated phase shifter that allows to vary the delay between synchrotron and laser pulses. The photon-counting approach adopted[13], allows performing TR-XAS experiments fully exploits the available x-ray photon flux at the 500 MHz repetition rate of Elettra providing continuous snapshots of the transient state spectra (multi-bunch mode). A scheme of the detection and acquisition system[13] is shown in Figure 5.7. The pump and probe synchronization is achieved by exploiting the radio frequency (RF) master clock of Elettra which provides the time structure of the generated radiation. The RF is divided by a timing unit allowing the remote control of the relative time delay by phase-shifting the oscillator frequency to the master RF. The phase stabilization of the laser source is achieved via a synchronization unit, which locks the laser oscillators to the Elettra master RF with a time jitter <2 ps.

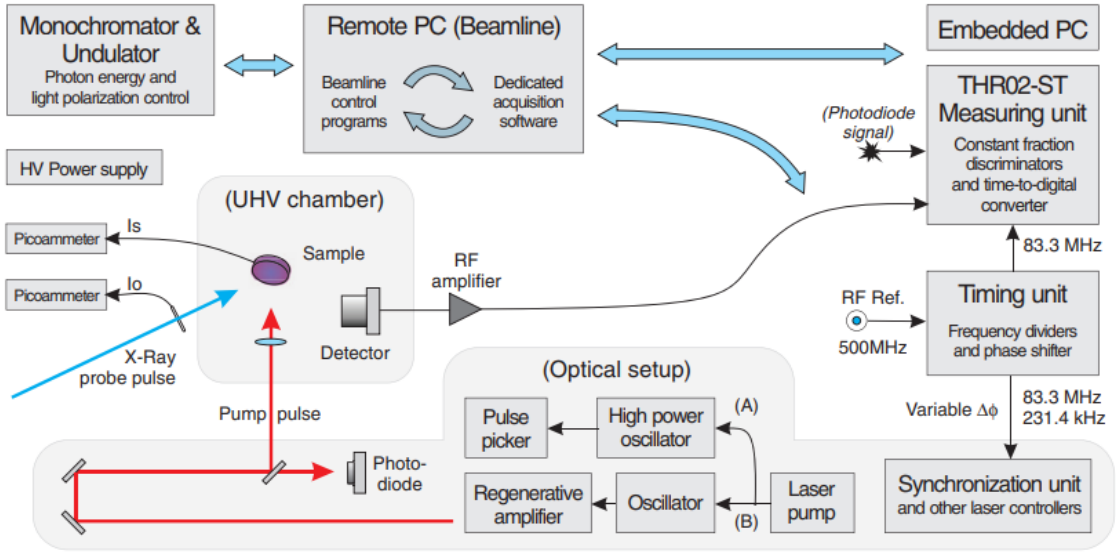

Figure 5.7 *Schematic layout of the experimental setup of the TR-XAS detection and acquisitions systems reported from ref. 13. It is based on three main sections: the beamline environment (UHV chamber, picoammeters, power supplies, undulator, monochromator, and remote PC), the optical setup (laser sources and controllers), and the measuring setup (THR02-ST measuring unit, timing unit and embedded PC).*

After a trigger signal, the THR02-ST measuring unit[14] starts recording the arrival time of all the detected events over a configurable time window (typically a complete synchrotron revolution period). The MCP analogue output signal is amplified, shaped, and

widened to about 4 ns so that the signal can be digitized using a constant fraction discriminator (CFD). The CFD output is finally recorded by the THR02- ST unit. The timing unit can be used to perform phase-shifted TR-XAS spectra, with 50 ps minimum step.

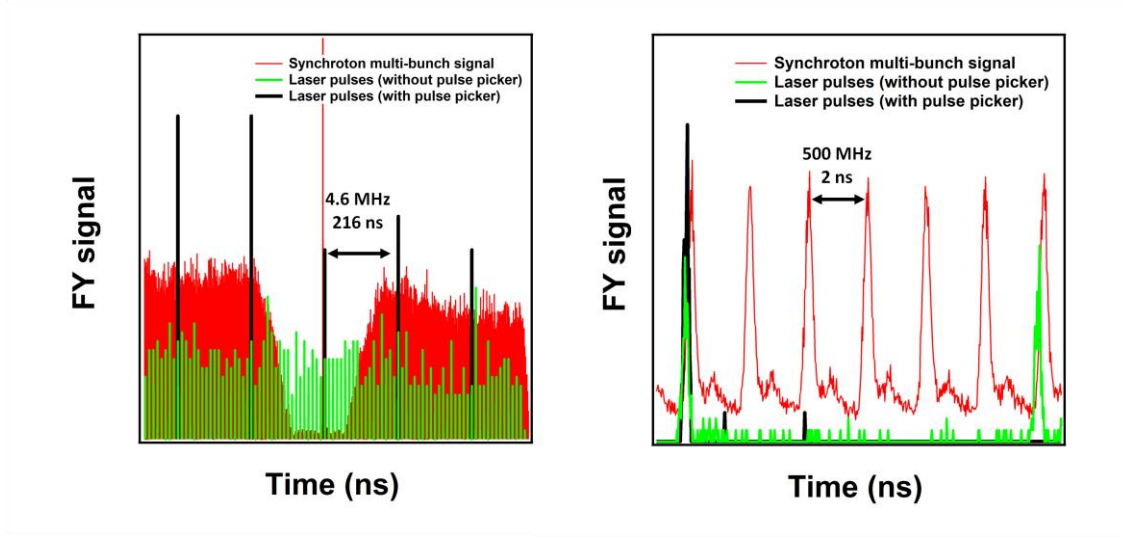

Figure 5.8 *Typical acquisition time histograms (counts vs consecutive photon bunches) over two synchrotron bunch revolutions of the laser and X-ray pulses* ***(left)****. The x-ray fluorescence signal clearly inherits the time structure of the storage ring filling pattern (2 ns time separation between two consecutive photon pulses), while the standard deviation (FWHM = 130 ps) of each measured pulse is wider than the typical width of electron bunches (60 ps). In normal laser operation mode (83.3 MHz rep. rate), six X-ray probe bunches impinge the sample between two consecutive pump pulses, allowing to measure relaxation dynamics in a 12 ns time window. By using a pulse picker the time window is extendable up to 216 ns* ***(right)****.*

Typical acquisition time histograms as a function of photon bunches and photon energy are shown in Figure 5.8. The detection rate is determined by the maximum dynamical range of the detector ($5x10^6$ counts s^{-1} or 0.04 photons per bunch). The combination of this acquisition strategy with an ultrafast MCP detector (rise time ~300 ps[15]) results in an acquisition system that is fast enough to isolate the X-ray pulses coming from each consecutive photon bunch, maintaining a linear response over the entire X-ray flux range.

Finally, the spatial alignment between pump and probe beams is made by using a YAG wafer placed below the sample. The X-ray and laser spots are superimposed by using a CCD camera. The laser beam position is moved until an optimal spatial overlap is achieved. For the temporal overlap, the pump laser scattered from the sample is detected by the MCP and singled out in the counts versus time histogram (Figure 5.8). From this picture, the relative time delay between the pump and probe sources can be directly observed and adjusted by acting on the phase shifter in the timing unit.

5.3 Results of the commissioning

Steady-state and time-resolved XAS measurements were performed in FY mode by using the MCP detector described in the previous section. For the chamber setup optimization, the first step consisted in testing the TR-XAS endstation performances characterizing the detector efficiency in the photon energy range of 40-1200 eV at different experimental geometries. All incidence and detection angles of the beams and detector reported are referenced to the sample surface. The efficiency of the MCP detector was characterized by measuring the FY signal of absorption edges in model samples, from the Si $L_{2,3}$ edge (100 eV) to the Ge $L_{2,3}$ edge (1270 eV). The incident photon flux was measured by a photodiode directly mounted on the sample holder. The MCP efficiency at normal emission resulted in the 10% range, in agreement with MCP specifications[15]. The MCP setup allows the free rotation of the detector around the whole emission solid angle of the sample. In this way, an evaluation of the angular dependence of the FY signal counts as a function of the MCP detection angle at different edges was performed. An example is shown in Figure 5.9b for the Ge $L_{2,3}$ edge. The expected FY intensity was calculated by the eq. 5.1. The comparison between the FY calculation and the experimental data is quite good. The disagreement between calculated and measured FY at X-ray angles close to the normal incidence (90° to the sample surface) is ascribed to self-absorption effects[2,10,11] not accounted for by the T-XRES code.

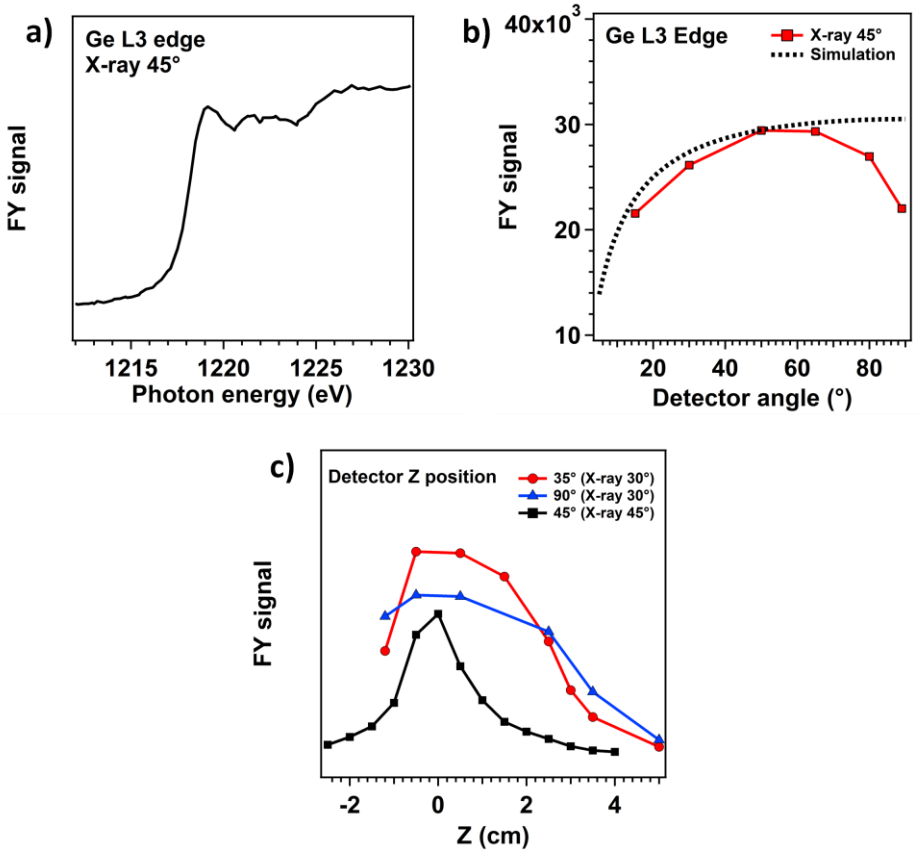

Figure 5.9 a) *steady state XAS spectrum of the Ge L_3 edge and the FY signal dependence, at the Ge L_3 edge, on the detection geometry along the* **b)** *incidence plane (the dashed curve is the calculate FY dependence by T-XRES code),* **c)** *and the z axis.*

Normal emission geometry enhances self-absorption contributions, while grazing emission is the optimal geometry to avoid self-absorption effects in the XAS spectra. Optimal agreement between simulation and experimental data is observed at grazing emission. Exploiting the Z-motion of the MCP, further characterization of the out-of-plane FY signal solid angle was performed. In the case of in-plane detection, reflectivity induced by the laser in the MCP signal may be significant, affecting the quality of XAS spectra.

Figure 5.9c show the dependence of the FY signal at the Ge L_3 edge as a function of the detector Z position for different MCP-X-ray geometries. At Z=0 (incidence plane of X-ray, in-plane detection) the FY intensity is dependent on both the X-ray incidence and detection angle. By varying the X-ray incidence angle a notable broadening of the emission solid angle is observed. At 45° the FY maximum is highly peaked at Z=0 (sample plane), while at 30° a "broadened" distribution of the intensity maximum, up to 2.5 cm below the sample plane, is observed. This situation suggests constraints in the out-of-plane detection for TR-XAS experiments. The advantage to avoid the reflectivity induced by the laser in the out-of-plane geometry, on the other hand, may lead to a low FY signal (depending on the X-ray incidence angle) compromising the S/N in TR-XAS measurements. Theoretical models to account for the FY solid angle as a function of Z in the soft X are not reported in the literature. Further optimization of the T-XRES code will include the modelling of the FY signal as a function of the Z-axis. Additional sample characterizations (systematic study at different element edges) will be performed to address this point. The characterization of a structurally anisotropic sample, 4H-SiC, was performed at different X-ray-detector geometries (Figure 5.10). For a fixed detection angle (grazing emission, 15°) drastic changes in the spectral shape are observed going from normal incidence to grazing incidence (30°) of the X-ray (Figure 5.10a). Figure 5.10b, c and d highlight the importance of the experimental configuration used. Both the X-ray incidence and detection angles modify the relative intensity between spectral features. The intensity of the resonance peaks is enhanced at specific geometries and reduced in other.

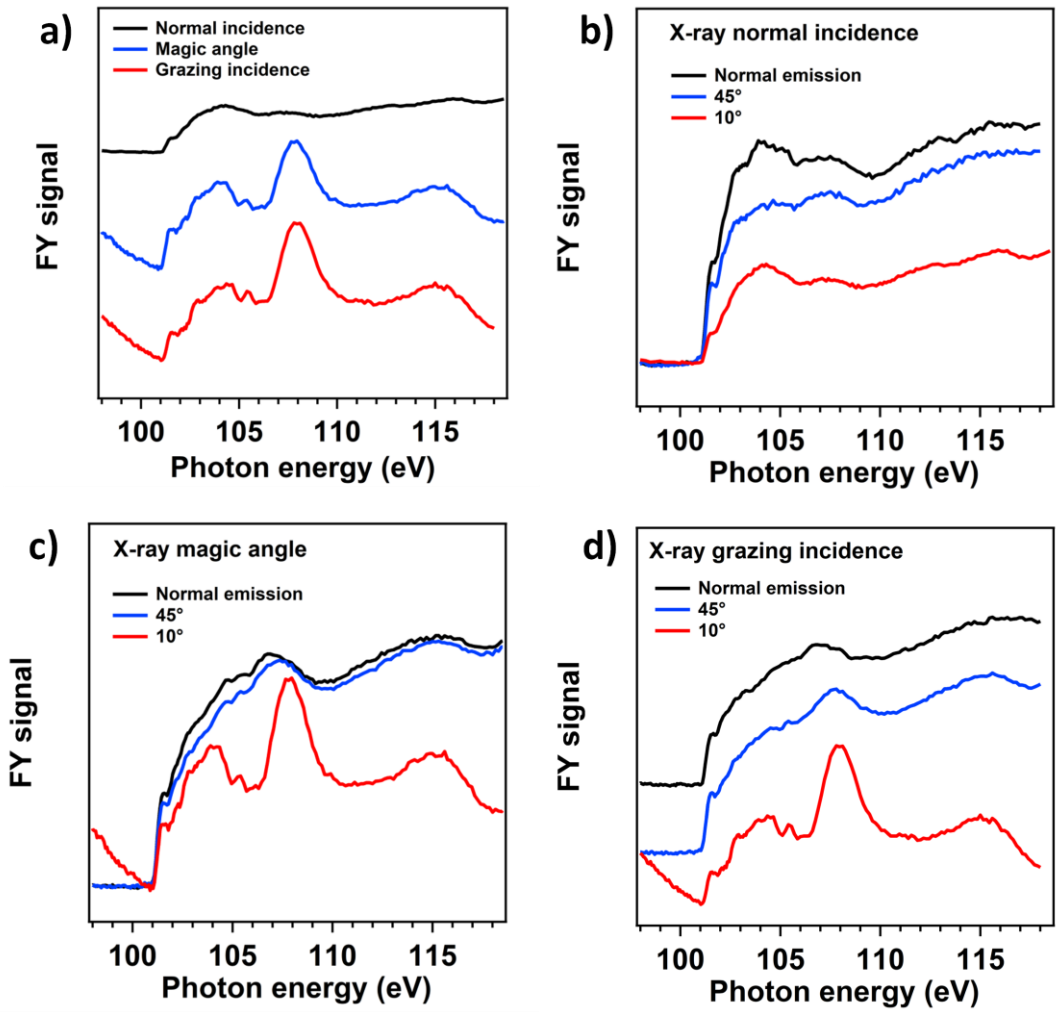

Figure 5.10 *Steady state XAS spectra of 4H-SiC sample.* **a)** *Dependence of the FY signal on the X-ray incidence angle, at a detection angle of 15°;* **b) c)** *and* **d)** *Dependence of the FY signal on the detection angle for fixed X-ray incidence angle.*

By pilot laser on-laser off XAS experiments on a 6H-SiC sample, the dependence of the FY signal on the experimental X-ray geometry was tested. Figure 5.11a shows the 6H-SiC C K edge raw data (i.e. without normalization by the structures of the beamline optics as measured by the I_0, see ref. 5) obtained with (laser On) and without (laser Off) laser excitation (400 nm, the maximum of the sample optical absorption) at two X-ray incidence angles, normal incidence (90°) and grazing incidence (20°). Notable spectral differences are observable between laser on-laser off spectra at grazing incidence, demonstrating a complex scenario of dynamical processes over the whole NEXAFS region of the 6H-SiC C K edge. Since in laser on-laser off measurements the FY signal is not discriminated in time by the MCP, the spectra represent an average picture of the excited state dynamics. In other words, the laser on spectrum is a convolution of the laser-induced spectral difference between consecutive pump pulses. This means that the spectral differences observed at grazing incidence are due to "slow" relaxation dynamics in the time domain of the laser repetition rate (83.3 MHz, 12 ns). Noteworthy at X-ray normal incidence a dramatic increase of the FY signal between laser on-laser off spectra is present. Figure 5.11b shows

the evaluation of the pump ratio as a function of the X-ray incidence angle. Accordingly, such spectral difference is not purely addressable to the X-ray geometry. In contrast, a lower pump ratio is predicted at normal incidence. Considering that the spectra were measured on the scattering plane, reflectivity changes induced by the laser in the MCP signal may justify such an effect. Finally, a TR-XAS experiment was performed on a 6H-SiC sample at the Si $L_{2,3}$ edge. Figure 5.11c shows the spectra obtain as a function of the time delay up to 1 ns (X-ray normal incidence). A relaxation dynamics of the resonance peak at about 103 eV with 210 ps decay time is observed, demonstrating the feasibility of time-resolved experiments at the TR-XAS end-station. However, the relative spectral difference, ΔA, is unexpectedly high (10%). Similarly to the laser on-laser off measurements, the spectra were acquired in the scattering plane of the sample. A partial contribution to the FY signal induced by the laser may be present. However, the dramatic spectral differences observed at the C K edge here are not detected. The data analysis of both laser on-laser off and TR-XAS spectra is currently in progress. Further experiments exploiting the out-of-plane detection geometry of the MCP will provide relevant insights to clarify the effects discussed above.

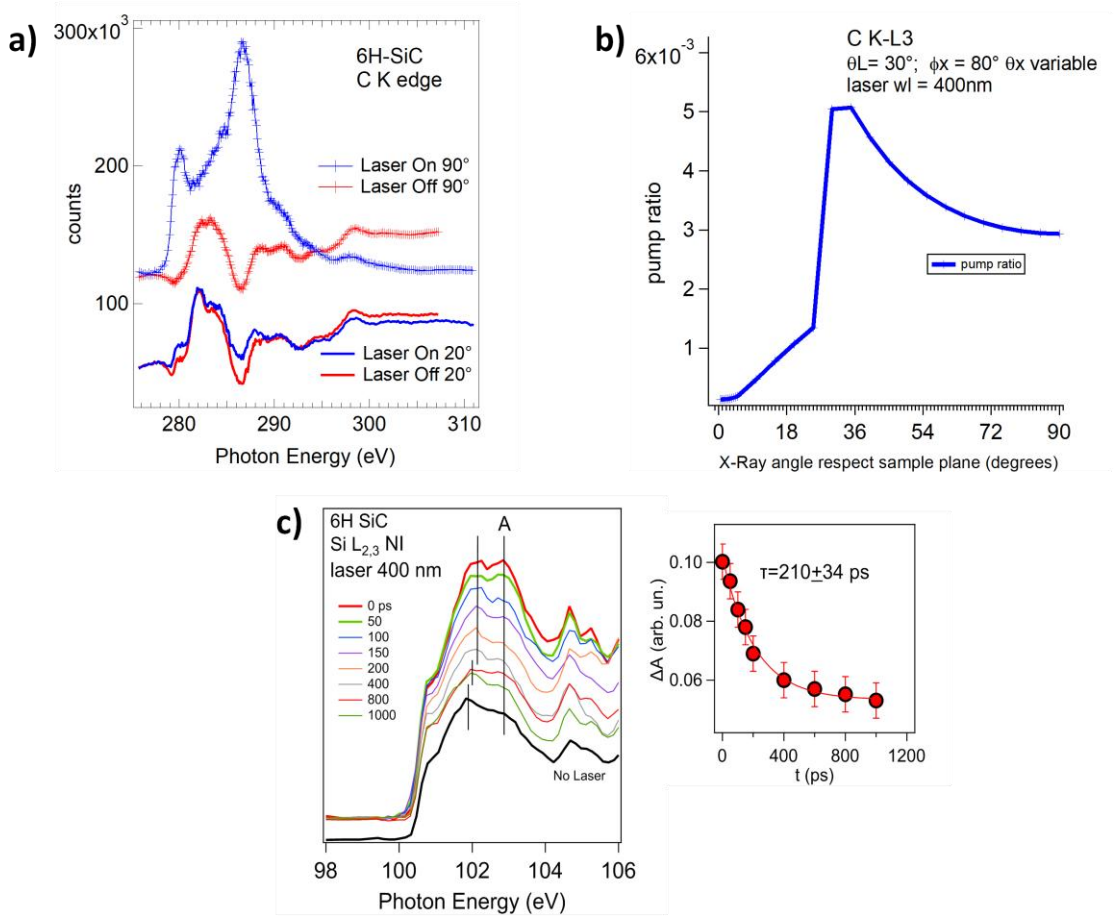

Figure 5.11 a) *Raw data of the 6H-SiC C K edge with and without laser excitation at X-ray normal and grazing incidence;* **b)** *T-XRES evaluation of the pump ratio, i.e. the fraction of excited species;* **c)** *TR-XAS spectra of the 6H-SiC Si L3 edge (X-ray normal incidence) as a function of the time delay up to 1 ns (left) and decay curve of the relaxation dynamics of the resonance peak at 103 eV (right). ΔA is*

defined as the difference between spectra with and without laser excitation, normalized over the without laser excitiation data.

Further characterization of the CoPc and CuPc systems by TR-XAS experiments is planned, even by using a different laser source. We aim to get further information on the possible interconnection between the CoPc long-living excited states and the molecular ordering. Open questions remain on the CuPc/SiO_2/p-Si(100) heterojunction as well as for the dynamics observed in the bare substrate. TR-XAS measurements of the SiO_2/Si will provide additional information on the substrate dynamics to clarify the origin of the additional relaxation process observed (with a decay time of 5.9 ns) using high pump fluence in TR-PES measurements (see Chapter 4 section 4.4), as well as the possible contribution of lattice deformation and heating effects in the substrate SPV dynamics (they occur in comparable time scale).

References:

[1] C. Bressler, and M. Chergui. Ultrafast X-ray Absorption Spectroscopy. *Chem. Rev.* **2004**,104, 1781-1812.

[2] M. Bianchini, and P. Glatzel. A tool to plan photon-in/photon-out experiments: count rates, dips and self-absorption, *Journal of Synchrotron Radiation* **2012**, 19, 911–919.

[3] M. Zangrando, M. Zacchigna, M. Finazzi, D. Cocco, R. Rochow, and F. Parmigiani. Polarized high-brilliance and high-resolution soft x-ray source at ELETTRA: The performance of beamline BACH. *Rev. Sci. Instrum.* **2004**, 75, 31.

[4] M. Zangrando, M. Finazzi, G. Paolucci, G. Comelli, B. Diviacco, R. P. Walker, D. Cocco, and F. Parmigiani. BACH, the beamline for advanced dichroic and scattering experiments at ELETTRA. *Rev. Sci. Instrum.* **2001**, 72, 1313.

[5] J. Stöhr. *NEXAFS Spectroscopy*. Springer Series in Surface Sciences; Springer Berlin Heidelberg:

Berlin, Heidelberg, **1992**.

[6] L. G. Parratt. Surface Studies of Solids by Total Reflection of X-Rays. *Physical Review* **1954**, 2, 95, 359-369.

[7] M. S. del Rìo, et al. *XRAYLIB tables (X-Ray fluorescence cross-section.* European Synchrotron Radiation Facility and University of Sassari, www.esrf.eu.

[8] *CXRO X-Database: Atomic Scattering Factor*. http://henke.lbl.gov/optical_constants/sf

[9] E. D. Palik. *Handbook of Optical Constants of Solids*. Academic Press, Boston, **1985**.

[10] L. Tröger, D. Arvanitis, K. Baberschke, H. Michaelis, U. Grimm, an d E. Zscheh. Full correction of the self-absorption in soft-fluorescence extended X-ray absorption fine structure. *PRB* **1992**, 46, 6, 3283-3288.

[11] P. Pfalzer, J.-P. Urbach, M. Klemm, S. Horn, Marten L. denBoer, Anatoly I. Frenkel, and J. P. Kirkland**.** Elimination of self-absorption in fluorescence hard-x-ray absorption spectra. *PRB* **1999**, 60, 13, 9335-9339.

[12] D. Haskel. FLUO: *Correcting XANES for self-absorption in fluorescence measurements*. University of Washington, USA, **1999**. Haskelphys.washington.edu.

[13] L. Stebel, M. Malvestuto, V. Capogrosso, P. Sigalotti, B. Ressel, F. Bondino, E. Magnano, G. Cautero, and F. Parmigiani. Time-resolved soft x-ray absorption setup using multibunch operation modes at synchrotrons. *Review of Scientific Instruments* **2011**, *82*, 123109-44913.

[14] See http://www.elettra.trieste.it/ilo.

[15] See www.hamamatsu.com for Hamamatsu Photonics.

6. Conclusions

This thesis work provides a deeper insight into the exciton dynamics and charge separation effects in semiconductor systems through time-resolved spectroscopies. TAS and TR-UPS have been used to gather information on the de-excitation pathways and charge transfer in molecular films. TR-XPS provides a detailed understanding of charge separation processes induced by the SPV. The influence of the molecular ordering in CoPc thin films is investigated by a multi-technique approach (time-resolved photoemission and optical spectroscopies), demonstrating the connection between the CT process and molecular structure. CoPc films were grown onto ITO, graphene and Au(111) substrates obtaining three different molecular structures, respectively, disordered, herringbone and brickstone. By using combined PES-IPES measurements, the molecular orbitals involved in the CoPc excited state dynamics were clarified. To determine the CoPc relaxation dynamics independently of the influence of molecular ordering, the disordered film was first studied as a reference. TAS measurements show competitive de-excitation through IC and ISC processes. However, relaxation from triplet excited states (populated by ISC) is the preferential relaxation pathway, resulting in long-living CoPc excited states. An additional ultrafast relaxation process (decay time of about 200 fs) is observed in the transient spectra. However, its origin was not determinable by solely TAS measurements. The complementary use of TAS and TR-PES measurements allowed us to point out the direct involvement of the Co $3d_z^2$ orbital in this dynamic process. An energy shift of the SOMO (originated from the Co $3d_{z^2}$ orbital) is observed in the TR-PES spectra. We tentatively explain the SOMO energy shift as a partial redistribution of the charge density between the phthalocyanine macrocycle and the Co atom. The promotion of electrons from the HOMO to the SUMO by the pump excitation would imply the complete occupancy of the single occupied orbital and charge redistribution toward the Co atomic site. Calculations show that, due to the repulsion between electrons, the complete occupancy of the Co $3d_{z^2}$ orbital should cause an energy increase of the corresponding state by 0.2 eV.

Since these dynamical processes are intra-molecular relaxation, no differences are observed in their time evolution in ordered CoPc films. Identical decay times are observed. At variance, the different molecular arrangement leads to differences in the CT exciton relaxation dynamics. Enhanced CT exciton lifetime is observed in CoPc film with herringbone structure (decay time of tens of ps) to the brickstone structure (decay time of a few ps), demonstrating the possibility of optimizing CT processes in the molecular film depending on the molecular structure.

Charge separation effects were investigated in the CuPc/SiO_2/p-Si(100) heterojunction. The static and transient SPV at the CuPc/SiO_2/p-Si(100) interface were systematically measured using TR-PES and modelled through the LEINEC code (developed in this thesis work). The code was able to evaluate their SPV magnitude and relaxation dynamics correctly, clarifying the role of the sample properties and experimental conditions in the SPV dynamical processes. The CuPc thin film shows a transient SPV effect with identical magnitude and relaxation dynamics of the SiO_2/Si(100) substrate, highlighting a direct

connection between the SPV relaxation dynamics of the inorganic substrate with the organic film. To address the origin of the SPV dynamics in the molecular film, a detailed characterisation of the SPV effect in n- and p-doped SiO_2/Si(100) substrates was performed. Both samples show a significant SPV effect. The SiO_2/p-Si(100) system ($8x10^{14}$ cm^{-3} dopant concentration) show increasing Si2p core level shifts (46 meV- 95 meV), due to the SPV, for increasing laser fluences (0.066 μJ cm^{-2}-15.5 μJ cm^{-2}). The analysis of the Si2p shift decay curves, measured by TR-PES, reveals an SPV decay time of about 100 ns. Noteworthy, a second decay time of 5.9 ns is observed by using high pump fluence. The origin of such decay time may be due to an additional dynamical process to the SPV relaxation dynamic. A more systematic characterization is required to clarify this point. In the n-doped SiO_2/Si(100) sample ($1.6x10^{19}$ cm^{-3} dopant concentration) a Si2p core level shift, due to the SPV, of 68 meV is observed. The SPV relaxation dynamic shows a decay time of 1.6 ns, many times faster than the SiO_2/p-Si(100) case. The LEINEC code was then used to model the experimental data. Accordingly, we tentatively explain the presence of the SPV effect in the CuPc by an induced effect from the SiO_2/Si substrate. Since the SiO_2 layer is thin (2 nm) as compared to the typical SCR width, the excess of positive charge, due to the energy level equilibration with the Si, should not be effectively screened at the CuPc/SiO_2 interface. In other words, we assume that to counterbalance the excess of positive charge, at the SiO_2 surface that faces the organic film, negative charging in the CuPc layers may be induced. As a consequence, the CuPc core levels shift and their relaxation dynamics would directly reflect the "reorganization" of the carriers induced by the SPV effect in the SiO_2/p-Si(100) substrate, leading to identical relaxation dynamics.

Despite the valuable number of information provided by the spectroscopic approach reported in the studies discussed above, TAS and TR-PES do not provide any information on the possible correlation between the structural dynamics and the electronic relaxation processes over time. On the contrary, X-ray absorption offers this advantage by probing both the electronic and structural properties of the system at the same time. With the aim of better understanding the structural evolution in the dynamics of electronic properties, we developed a new experimental end-station for time-resolved X-ray absorption spectroscopy, in which excited state dynamics can be characterised with 80-100 ps resolution. The new experimental end-station offers a completely variable geometrical configuration between pump (laser), probe (X-ray) and detector (MCP). The variable geometry allows for optimising the laser-X-ray excitation volumes, maximising the S/N, making TR-XAS experiments feasible for large classes of materials. The complete mobility of the MCP around the sample plane and along the Z-axis (height position to the sample) allows to optimise the detection of the fluorescence signal (for a given laser-X-ray geometrical configuration) and avoids reflectivity induced by the laser in the MCP signal, as well as self-absorption effect. The T-XRES code has been developed as an auxiliary tool to the TR-XAS end-station to evaluate a priori the optimal experimental condition. Preliminary results of the commissioning are shown demonstrating the feasibility of the TR-XAS experiment. At the moment, the optical system operates without laser amplification, limiting the performance of the pump pulse. This constraint strongly affected TR-XAS experiments during the commissioning.

From the technological point of view, we do believe that all the aspects discussed in this thesis work are fundamental to optimising the heterojunction-based device. The film electronic properties (exciton generation, charge transport) and the interface properties (charge separation and injection), as well as the structural influence in their dynamical processes, are fundamental in determining the efficiency of the device. As suggested by this thesis work, a detailed and complete overview of the dynamical properties of the system can be obtained by combining complementary information from different time-resolved techniques.

Concerning future perspectives, further characterization of the CoPc and CuPc systems by TR-XAS experiments is planned. We aim to get further information on the possible interconnection between the CoPc long-living excited states and the molecular ordering. Electrical measurements are also planned to determine the CoPc mobility in the three different structures. Open questions remain on the CuPc/SiO_2/p-Si(100) heterojunction as well as for the dynamics observed in the bare substrate. TR-XAS measurements of the SiO_2/Si will provide additional information on the substrate dynamics to clarify the origin of the additional relaxation process observed (with a decay time of 5.9 ns) using high pump fluence in TR-PES measurements, as well as the possible contribution of lattice deformation and heating effects in the substrate SPV dynamics (they occur in comparable time scale).

Finally, a detailed characterization of the formation of the band bending as a function of the increasing CuPc film thickness (and relative SPV dynamics), as well as TR-PES measurements of CuPc thin films grown on Si substrate with a thicker SiO_2 layer (enough to screen the SiO_2/Si interface influence) and without SiO_2 layer, will be performed in the next future. This is important to get a deeper insight into the SPV effect in organic semiconductors: a specific model which considers the organic material characteristics is still missing.

List of Acronyms

AEY	Auger Electron Yield
CB	Conduction Band
CCD	Charge Coupled Device
CFD	Constant Fraction Discriminator
CT	Charge Transfer
FY	Fluorescence Yield
FWHM	Full Width Half Maximum
HB	Hybrid-Bunch
HOMO	Highest Occupied Molecular Orbital
IC	Internal Conversion
IPES	Inverse Photoemission Spectroscopy
IR	Infrared
ISC	Intersystem Crossing
MB	Multi-Bunch
MCP	Multi-Channel Plate
MO	Molecular Orbital
NEXAFS	Near-Edge X-ray Absorption Fine Structure
LEINEC	Light/Electron Induced Non-Equilibrium phenomena Calculator
LUMO	Lowest Unoccupied Molecular Orbital
OPA	Optical Parametric Amplifier
PES	Photoemission Spectroscopy
PEY	Partial Electron Yield
PP	Pump-Probe
RF	Radio Frequency
S/N	Signal-to-Noise ratio
S	Singlet

SB	Single-Bunch
SCR	Space Charge Region
SOMO	Semi-Occupied Molecular Orbital
SPV	Surface Photovoltage
STM	Scanning Tunnel Microscopy
SUMO	Semi-Unoccupied Molecular Orbital
SV	Surface Voltage
T	Triplet
T-XRES	Time-Resolved X-ray Experiments Simulator
TAS	Transient Absorption Spectroscopy
TEY	Total Electron Yield
TR-PES	Time-Resolved Photoemission Spectroscopy
TR-UPS	Time-Resolved Ultraviolet Photoemission Spectroscopy
TR-XAS	Time-Resolved X-ray Absorption Spectroscopy
TR-XPS	Time-Resolved X-ray Photoemission Spectroscopy
TTL	Transistor-Transistor Logic signal
UHV	Ultra High Vacuum
UPS	Ultraviolet Photoemission Spectroscopy
VB	Valence Band
XAS	X-ray Absorption Spectroscopy
XPS	X-ray Photoemission Spectroscopy

Ringraziamenti

Come è giusto che sia, è arrivato il momento di ringraziare chi di dovere e che ha contribuito a questo mio lungo percorso di dottorato che orami giunge al termine.

Il primo nome in lista è senza dubbio Maddalena Pedio, innanzitutto per le numerose e indispensabili discussioni sull'interpretazione delle misure di questa tesi (e averla corretta, cosa non di poco momento). Ma soprattutto grazie per il costante supporto ed avermi insegnato tutto ciò che sono riuscito ad imparare (a volte bene a volte meno) in questi anni.

Vorrei poi ringraziare tutte le persone che hanno partecipato in questi anni allo sviluppo della nuova end-station TR-XAS, uno dei principali progetti (e probabilmente il più impegnativo e soddisfacente) del mio dottorato, di cui: lo staff di BACH, in particolare Elena Magnano, Federica Bondino e l'infaticabile Igor Pis che si è fatto insieme a me tutte le notti di beamtime durante il commssioning di TR-XAS. A seguire, ma non per importanza, tutto lo staff tecnico, Federico Salvador (senza di te come faremmo), Andrea Fondacaro e Massimiliano De Marco. Senza ovviamente dimenticarsi di Roberto Gotter con cui ho condiviso gioie e dolori dei beamtime, ma anche per i consigli pratici ed efficaci per l'ottimizzazione del setup sperimentale della camera. Ma soprattutto vorrei fare un ringraziamento speciale in memoria di Aleksander De Luisa che ha partecipato alla progettazione e disegnato i progetti iniziali di TR-XAS.

Un sentito ringraziamento va Martina dell'Angela e Roberto Costantini di ALOISA, in quanto molto probabilmente senza il beamtime con voi una buona parte dell'ultimo capitolo di questa tesi non esisterebbe. Ma un grazie anche per le preziose discussioni sull'interpretazione di quelle stesse misure.

Un più che dovuto grazie va a Barbara Ressel, memori del tempo passato insieme a fare misure dove andava sempre tutto "liscio". Anche se però alla fine in qualche modo il risultato lo portavamo a casa.

Un altro speciale ringraziamento va a Monica Valli. Se al liceo non mi avessi convinto a continuare a studiare oggi non sarei neanche qua a scrivere questa tesi. Ma anche a Marta, dopo che Monica non mi poteva più tenere d'occhio ci hai pensato te a farmi rigare dritto.

E per finire grazie a mamma e papà che mi hanno sempre sostenuto in tutti questi anni e che sempre lo faranno.